NON-EQUILIBRIUM X-RAY EMISSION FROM YOUNG SUPERNOVA REMNANTS

Thesis by

John Joseph Nugent Jr.

In Partial Fulfillment of the Requirements

for the Degree of

Doctor of Philosophy

California Institute of Technology

Pasadena, California

1983

(Submitted on October 4, 1982)

Acknowledgements

In my immediate academic world, there are many colleagues/friends to thank. First, my gratitude to the graduate students (past and present), who provide that all important day-to-day support structure: Dave Ennis, Kris Sellgren, Erich Grossman, Norm Bobroff, Ken Jensen, Ann Rosenthal, Beth Nordholt, Bill Priedhorsky, and France Cordova. To my "mini-advisors", the postdocs, for their advise and friendship, I thank John Nousek, Steve Pravdo, and Ian Tuohy. My advisor, Gordon Garmire, has provided not only scientific advice and financial support, but more importantly the freedom and responsibility which has made research at Caltech a rewarding experience. I thank him for that confidence as well as his patience in my failures, and his appreciation in my successes. In addition, thanks to Roger Blanford for being a gracious and effective pinch-hit advisor, to Pat Neill, for help in guiding me through the bureaucratic maze at Caltech and for brightening the day, and to many other people who have made the 3rd floor of Downs a pleasure to work on. From long ago, I'd also like to thank Garrett Jernigan who was an bountiful source of inspiration in the early phase of my scientific career.

There are many friends outside of work who should be acknowledged for making Caltech a bearable place to live over the years. Among them are Jim Rolph, Lloyd Townley, John and Shelly Daub, Armando Manduca, Cathy Allen, Ann Bobroff, Bill Dow, Wayne Berman, Bob Kanne, the Basketball Team, the Volleyball Team, and the Softball Team. For her care and understanding patience during the trying thesis period, my thanks to Maryanne Duffy. Last and most of all, for everything over the years, my deepest gratitude and love goes to my Aunts, Betty ("BB") and Kay, and to Mom and Dad.

****

On the technical side, I would like to acknowledge John Raymond and Barry Smith for their plasma code, Steve Pravdo, again, for the SPECFT code, and Andy Symkowiak for all his help with collecting the SSS data and providing the SSS response matrix.

Finally, I would like to thank the numerous Chinese astronomers not only for their observations but for inadvertently teaching an important lesson. These people labored producing tomes of information which addressed the issues of the day concerning the universe. Today, a millennium or two later, we view their observations as crude and their "issues" as myths, yet, within their tomes, they provided a record that will be timeless in its importance. I find a faint hope in that as I sit here putting the finishing touches on my tome which addresses the issues of the day concerning the universe.

Abstract

A computer model (NIE model) has been developed to predict the the x-ray spectra from the hot (10^{6-8} K), shock-heated plasmas that are found in the remnants of supernovae. The model accounts for the lack of collisional ionization equilibrium and for the possible lack of thermal equilibrium between the electrons and ions behind the shock fronts. Both of these effects are potentially important in determining the emergent x-ray spectrum of young ($\lesssim 10^4$ years old) supernova remnants (SNR). Both a spectral component arising from the supernova ejecta and a component arising from the shocked interstellar medium (ISM) surrounding the supernova are calculated.

The NIE model has been fit to the spectral data from two young SNR's, MSH 14-63 and RCW 103. The data from MSH 14-63 were collected with the *HEAO A-2* experiment and spans an energy range from 0.18 - 15 keV. Spectral resolution varies over this range. For example, $\Delta E/E$ = 32% FWHM at 1.5 keV, and $\Delta E/E$ = 15% FWHM at 7 keV. Important results from applying the model are: a significant non-Coulomb, ion-electron interaction is occurring in the remnant, presumably at the shock front; the data can be fit by a model with little or no emission from any source other than the shocked ISM with an age which is consistent with that of MSH 14-63; anomalous abundances of heavy elements and possible discrepancies in the centroid and shape of the Fe K_α feature could be explained by inhomogenities in the ISM density or by ejecta that have come to thermal equilibrium with the shocked ISM; and under the assumptions of the model, the distance to the MSH 14-63 is inconsistent with distance measured to an OB star group that is suggested to be associated with the remnant.

The data for RCW 103 were obtained using the Solid State Spectrometer (SSS) on board the *HEAO-2* spacecraft. This data set had a more limited spectral range than above (0.8 - 2.5 keV) but enhanced spectral resolution

($\Delta E/E \approx 10\%$). In addition, the data had limited spatial resolution. The principal results from this work are: no variation can be detected in the spectrum collected from different regions of the remnant; the data cannot be used to determine whether non-Coulomb electron-ion energy exchange processes may be present behind the shock front; and assuming that non-Coulomb processes are present - a likely hypothesis given results from other young SNR's, the data are consistent with the idea that the emission is all from the shocked interstellar medium with approximately solar composition of heavy elements.

Short Abstract

A computer model (NIE model) has been developed to predict the the x-ray spectra from the hot (10^{6-8} K), shock-heated plasmas that are found in the remnants of supernovae. The model accounts for the lack of collisional ionization equilibrium and for the possible lack of thermal equilibrium between the electrons and ions behind the shock fronts. Both of these effects are potentially important in determining the emergent x-ray spectrum of young ($\lesssim 10^4$ years old) supernova remnants (SNR). Both a spectral component arising from the supernova ejecta and a component arising from the shocked interstellar medium surrounding the supernova are calculated.

The NIE model has been fit to the spectral data from two young SNR's, MSH 14-63 and RCW 103. The data from MSH 14-63 was collected with the *HEAO A-2* experiment and spans an energy range from 0.18 - 15 keV. Specral resolution is varies over this range. For example, $\Delta E/E$ = 32% FWHM at 1.5 keV, and $\Delta E/E$ = 15% FWHM at 7 keV.

The data for RCW 103 was obtained using the Solid State Spectrometer (SSS) on board the *HEAO-2* spacecraft. This data set had a more limited spectral range than above (0.8 - 2.5 keV) but enhanced spectral resolution ($\Delta E/E \approx 10\%$). In addition, the data had limited spatial resolution.

Table of Contents

Chapter 1: Overview

Introduction

In times past, supernovae, some with brightness that would rival any star in the sky, were viewed as portents of good and evil. We now view supernova as a funeral announcement of a dead star. While some stars end their life cycle by fading into cool rocks, others, go out with a spectacular explosion. Some of the explosive energy, $\sim 10^{51}$ ergs, goes into the kinetic energy of ejected matter. The supersonic ejecta shock heats the interstellar medium (ISM) for many parsecs around the star to temperatures on order of 10^{6-8} K. The ejecta and the shocked ISM are collectively known as the supernova remnant (SNR).

If a supernova represents the death of a star, then the SNR is a star's tombstone. Lasting as a distinct feature for $\sim 10^5$ years and stretching out eventually to distances of 100 pc or so, a SNR bears witness to the life and death of the progenitor star. This information about supernovae and the dynamics of the ejecta and the shocked ISM have interested observers across the entire energy spectrum. Supernovae and supernova remnants are of interest for the following reasons:

1) They are postulated to be responsible for the production and dispersal of heavy elements ($Z > 6$).
2) They are good sites for study of astrophysical plasmas. The issues of the dynamical properties of the shocked gas, properties of collisionless shock waves, and the atomic physics of highly ionized heavy elements can be addressed.

3) Supernovae are thought to be a major source of heating for the ~ 10^6 K gas which is observed throughout the galaxy.

4) Supernova shocks entering dense clouds may be responsible for some star formation.

5) Cosmic ray production is postulated to occur in the tangled, rapidly varying magnetic fields at SNR shock fronts.

6) Neutron star/pulsars are left over from some and maybe all exploded progenitor stars. Black holes may also be a possible by-product if the remaining cores are of high enough mass.

Because the bulk of the emission from plasmas of temperature 10^{6-8} K are in the x-ray regime of the spectrum, x-ray astronomy has been recognized as an integral part of the study of the dynamics of SNR's. Since galactic SNR are many arcminutes in extent, they are easily resolvable by present x-ray imaging techniques. These observations provide information on the morphology of the remnants. A separate avenue of research has been measuring the x-ray spectra emerging from the hot shocked gas. These two areas of research have not intersected as yet, except by implication, because no observations providing simultaneously good spectral and spatial resolution have yet been achieved.

This thesis is concerned with the issue of the x-ray spectra - in particular, the x-ray spectra emitted by the hot plasmas in young ($\lesssim$2000 years) SNR. Because they are closer in time to the supernova event and, hence, contain more information about the explosion young SNR's are of special interest. The prediction of x-ray spectra from young supernova remnants is complicated by a number of non-equilibrium effects. This thesis describes a computer model developed to account for these effects and the results of applying the model to observations of two young remnants. The balance of this chapter well give a brief introduction to supernovae, supernova remnants, and the x-ray spectra

from hot astrophysical plasmas. The latter topic also includes a discussion of the special problems related to young SNR's. The second chapter describes the computer model and the following two chapters present results of applying that model to observational data.

Supernovae

This thesis will be mostly concerned with the interaction of the supernova ejecta with the interstellar medium (ISM) surrounding the progenitor star. For that purpose we need only to characterize the supernova explosion by two parameters: the mass of the ejected material, M_e, and the amount of kinetic energy in the ejected material, E_0. Even though the inner workings of the explosion that determine M_e and E_0 are of no direct concern for the spectral model, an effort will be made, once M_e and E_0 are determined, to comment on their implication for supernova theory. We briefly comment, then, on the facts and notions concerning supernovae explosions.

From empirical studies of the time history of the optical flux from supernovae in other galaxies, two classes of supernovae explosions have been identified. These classes are denoted Type I and Type II. Nominal properties for these two classes have been summarized in Table 1, which was reproduced from a review article by Chevalier (1977). All of the properties are implied from observational evidence with the exception of the value of the ionizing radiation which comes from theoretical modeling of early supernova evolution. The two entries for ionizing radiation for Type I result from two different models. Simply speaking, Type I supernovae are thought to be less energetic and to have older, less massive progenitors than Type II supernovae.

Theoretical understanding of the mechanism of the explosion of the two type of supernovae is still in a early stage. Current work on modeling Type II

supernovae assume that they occur in young, massive stars that have exhausted their nuclear fuel. The explosive trigger arises from the infall of the core which is no longer supported by nuclear burning. A rarefication shock then proceeds through the outer envelope either providing directly the kinetic energy for ejection or triggering thermonuclear reactions that then provide the needed energy. Type I supernovae may have a similar explosive mechanism. Alternatively, it has been suggested that Type I supernovae may be caused by thermonuclear explosions in the outer layers of white dwarfs undergoing accretion.

Evolution of a Supernova Remnants

After the initial explosion, the evolution of an SNR can be divided into four phases. Briefly, these can be described as follows:

1) *Free expansion phase*: this is the early phase when the mass of the matter swept-up from the ISM by the shock wave is small compared to the mass of the ejected matter. The remnant expands at roughly a constant rate during this phase.

2) *Adiabatic phase*: During this phase, the expansion of the remnant begins to slow as the swept-up mass becomes comparable to and exceeds the ejected mass. In this phase, the energy in the ballistic and random motions of the gas is conserved since radiation losses are negligible.

3) *Radiation phase*: The luminosity of the remnant steadily increases and at some point total radiation losses become a significant fraction of the initial blast energy.

4) *Merging phase*: At some point the shock slows to a point that falls below the sound speed of the interstellar medium ($\sim$ 10 km s^{-1}) and the remnant starts to become indistinguishable from the ISM.

During the free expansion phase, the ejecta moves radially outward at a constant rate. A collisionless shock wave expands out in front of the leading edge of the ejecta at ~ 10% greater rate. A collisional shock does not form because the mean free path for the rapidly moving (~ 1 MeV) protons is large compared to the scale height of the galaxy. For proton - HI collisions, Spitzer (1978) estimates that the mean free path is ~ 500 pc. It is known by looking at the remnants of SNR with known ages that shocks form long before this, so the magnetic field in the interstellar medium is suspected of being the mediator of the shock.

This phase continues as long as mass of the matter swept-up by the main forward shock is small compared to the mass of the ejected matter. When the two masses become equal - at an age of roughly 100 to 1000 years - the ejecta's role in the hydrodynamics of the shocked gas begin to diminish and the remnant enters the adiabatic phase. The hydrodynamics of the shocked ISM during this period can be approximated by the Sedov similarity solution for blast waves from a point source in a homogeneous medium(1959). Since the remnant is radiating, it is not, of course, truly adiabatic; however, the total energy emitted is small compared to the energy of the blast. The adiabatic phase ends when this approximation becomes invalid - usually at an age of roughly 5-10 $\times$ 10^4 years.

Most SNR that are observed at x-ray wavelengths are in one of the two early early phases. These include the two discussed in this thesis. The two phases are illustrated by a Figure 1, which shows the shock radius, R_s, as a function of time. During the free expansion phase the R_s is proportional to t, but after t_s, when the mass of the shocked ISM begins to exceed the mass of the ejecta, the expansion slows and, as predicted by a Sedov solution R_s becomes proportional to $t^{2/5}$. The post-shock temperature is proportional to the square of the shock velocity and is somewhere in the range of 10^{7-8} K for typical SNR parameters.

As can be seen by calculating $(dR_s/dt)^2$, the temperature is constant at first and begins to fall like $t^{-6/5}$ during the Sedov phase.

In addition to the leading shock, a second "reverse-shock" wave that heats the ejecta has been postulated to form at an early age (McKee, 1974; Gull, 1973,1975). The reverse-shock acts to alleviate the pressure differences between the hot interstellar medium that has been shocked by the leading shock and cool, dense ejecta. As the name implies, the shock begins at the ISM/ejecta interface and moves towards the center of the remnant. Typical density and temperature profiles for a young SNR, which were calculated from a one-dimensional hydrodynamical numerical model used in this work, are shown in Figure 2. Three main regions, the ejecta, shocked ISM, and unshocked ISM, are noted. These profiles are for a time when the remnant is well into the Sedov phase and the curves show the Sedov similarity solution for the temperature and density profiles. As can be seen from Figure 2, the temperature of the ejecta is much lower than the temperature of the shocked ISM. In general, because the pressure is continuous across the contact discontinuity, the ratio of the temperatures of the two regions roughly are inversely proportional to the ratio of the densities.

X-rays from Supernova Remnants

The x-ray emission that is seen from supernova remnants is assumed to arise from hot plasmas produced by the aforementioned shocks. Evidence for this postulate is found in x-ray maps of SNR that exhibit circular shell-like structures whose sizes are consistent with the expected shock radius. Moreover, line emission from highly-ionized heavy elements have been observed in the x-ray spectra which confirm the thermal nature of the emission. An important exception is the Crab Nebula where synchotron radiation is postulated to explain a

non-thermal, power-law spectrum and an irregularly shaped, relatively small emission region.

Work on calculating the x-ray spectrum from the hot plasma that occurs in SNR has been going on for more than a decade (Tucker and Koren, 1971; Raymond and Smith, 1977; Shull,1982). These works have all assumed that the plasma is optically thin, that electron-ion collisions are the only important photon producing mechanism, that the electron energy spectrum can be represented as a Maxwellian, non-relativistic distribution, and that the composition of the plasma is somewhere near solar. This last assumption is important in the sense that only the contributions from about a dozen of the most abundant elements are calculated, while the contributions to the emission from the balance of the elements are considered ignorable.

These calculations are complicated because of the large number of photon producing mechanisms that exist. Figure 3 shows a typical model spectrum. The continuum is primarily produced by bremsstrahlung and radiative recombination from hydrogen and helium. The line emission from heavy ($Z \geq 6$) elements is the dominant emission mechanism in a large part of the spectrum.

A given line arises from a specific ionic species of element, so to calculate the power of a line not only does the temperature and relative abundance of each element need to be known but also the fractional concentration of the ionic species which is producing the line. The fractional concentrations of the different ionic species, in general, will change with time as electron collisions ionizes an ion with ionic charge z to charge $z+1$ or recombines to charge $z-1$. The rate for these processes is equal to the electron density times the concentration of the ion times functions of electron temperature. For a given temperature there exists a steady state set of relative ionic concentrations in which the ionizations and recombinations are in balance. A plasma in which all the

elements have a steady state set of ionic concentrations with respect to electron collisions is said to be in collisional ionization equilibrium (CIE). Under the assumption that the plasma is in CIE, then, the spectrum from each element is a function of temperature only and the total spectrum is a function of temperature and the relative abundances of the elements.

Until recently, work on interpreting the x-ray spectra of SNR have relied on the use of models of CIE spectra (eg Becker *et al.*, 1980). Two aspects consistently arose in the use of this approach. One was that two different temperature components were required to explain the data. The high temperature component was attributed to the shock heated ISM, while the low temperature was touted as possible evidence for the reverse shock component. A second aspect concerns the abundance of heavy elements. In order to explain the data, abundances of a factor of $\gtrsim 3$ larger than the solar value are needed.

One potential problem with using CIE models to interpret x-ray spectral data is that there might not be equipartition of energy between electrons and ions behind the collisionless shock. A second and more likely problem is that the plasmas are not in CIE; or in other words, the ionization state of the ions differ from the expected in steady state with a constant electron temperature.

If the only process to heat the electron gas are Coulomb interactions, then initially (T_e / T_i) could be as low as (m_e / m_i) where T_e and T_i are the electron and ion temperature and m_e and m_i are the electron and ion masses. The equilibrium time scales involved (Spitzer, 1962), in that case, will be $\sim 2000\ n_0^{-1}$ years, where n_0 is the ISM particle density. Because the electron temperature is an important parameter for determining the emergent spectra, this lack of thermal equilibration between the electrons and ions would have profound effects on the interpretation of the observed data from of a large number of SNR's. Particularly in young remnants, this could cause the kinetic

temperature of the shock to be underestimated. This effect is controversial. McKee (1974) has suggested that a number of plasma instabilities at a collisionless shock front could provide a mechanism to quickly bring the electron gas and ion gas into thermal equilibrium.

Observational evidence supporting both models exists. In the low Mach number collisionless shocks that occur when the solar wind impinges on the magnetosphere of the earth, T_e has been observed to be lower than T_i. In the very young remnants, Cas A and Tycho, Pravdo and Smith (1979) have observed electron temperatures that are comparable to expected shock temperatures.

The second problem is more theoretically sound. If the heavy elements come across the shock front in low states of ionization relative to the states heavily populated in CIE, then the ionization time scales to reach CIE are typically $10^{4-5}\, n_0^{-1}$ years (see Appendix). Even if a significant amount photoionization of the preshocked gas occurs, the time scales for obtaining CIE are still of the same order since the crucial recombination rates are comparable to the crucial ionization rates. Since much of the flux, particularly below 3 keV, is from line emission from heavy elements in highly ionic states, predicting the relative populations of these states is necessary in order to model the x-ray spectra. Itoh (1977) has shown that this effect can manifest itself by producing a spectrum that emulates a low temperature component, especially when the data were obtained from a detector with low resolution. Evidence for non-ionization equilibrium (NIE) in SNR's was first demonstrated by observations of the ratio of the iron/nickel emission features at 6.7 keV and 8 keV in the spectrum from Cas A which was lower than would be expected if the plasma were in CIE (Pravdo and Smith, 1979).

Objectives

Our first objective is to develop a model, which will be dubbed the NIE model, to calculate the time-dependent nature of the ionic concentrations and to account for effects on the spectrum of Coulomb or, alternatively non-Coulomb electron heating.

That done the next objectives are of two natures. The first is to examine what we would a call "global" issues. These global issues concern whether the model gives a good description of the data; if it does, what can the model say about the remnants given the state of the art in x-ray astrophysical spectroscopy; and finally, of the issues that the model cannot properly address, given the state of the art, what are some of the important observations for future consideration in order to properly address these elusive issues. The "local" issues concern the two particular remnants to which the model will be applied and how the information obtained from the model relates to information about each remnant obtained from variety of other observations. The hierarchy implied by the choice of words "global" and "local" necessarily becomes rather tangled and may be indistinguishable at times, but the reader should be aware that these two lines of thought run through this thesis.

Specifically the following questions will be addressed:

1) Is there evidence for non-Coulomb electron-ion interactions behind the collisionless shocks of supernova remnants?

2) Is there evidence of reverse-shocked emission from the ejecta?

3) If it is assumed that the bulk of the emission is coming from shocked ISM, are the elemental abundances inferred from line intensities near solar as would be expected?

4) How do the inferred values of the age, the ISM particle density, and the distance compare with other measured values.

5) Can the progenitor be characterized as a Type I or Type II based on the inferred values of the blast energy and the mass of the ejecta.

Data

The two sets of data that will be discussed are displayed in Figure 4. They represent observations of two remnants each from a different experiment. Details of the experiments will be given in later chapters, but we will introduce some of the important features here. The data on SNR RCW 103 have moderate resolution ($\Delta E/E \sim 10\%$). Line features from Mg, Si, and S can readily be seen. These features represent blends of lines from different ionic species. This data set suffers from its limited coverage of the x-ray spectrum. In contrast, the data from MSH 14-63 (also known as RCW 86) cover a rather large spectral range, but have worse spectral resolution. K_α line emission from Fe and S can be seen, but other features below 2 keV cannot be resolved. Other observations of RCW 86 have at least seen Mg K_α which strengthens the supposition that the flux below 2 keV is due to unresolved lines.

The RCW 103 data then are a good place to examine the profiles and intensities of the low energy lines, while the RCW 86 data allow the study of the higher energy lines and the overall shape of the spectrum. RCW 86 also has the important constraint that the age is known, since the supernova explosion which formed that remnant was seen by Chinese astronomers in AD 185.

Table 1

Properties of Supernova

	Type I	Type II
Ejected Mass ($M_\odot$)	0.5	5
Mean velocity (km sec^{-1})	1×10^4	0.5×10^4
Kinetic Energy (erg)	0.5×10^{51}	1×10^{51}
Visual radiated energy (erg)	4×10^{49}	1×10^{49}
Ionizing radiated energy (erg)	10^{44} or 10^{48-49}	10^{48-49}
Frequency (yr sup -1)	1/60	1/40
Stellar population	old disc	young disc

Figure Captions

Figure 1

The shock radius, R_s, is shown as a function of time during the early phases of SNR evolution. The time, t_s, when the mass of the shocked ISM begins to exceed the mass of the ejecta is the demarcation between the free-expansion phase and the adiabatic phase. Calculation for this plot was done by the hydrodynamic code used in the model in this thesis. Dotted line is a Sedov solution.

Figure 2

The density and mean temperature profiles for a given time are shown as a function of radius. Histogram represents the calculations made by the hydrodynamic code in this thesis and the smooth curve shows an analytic Sedov solution for an adiabatic remnant. The latter ignores the ejecta which a accounts for the discrepancy between the calculations in the ejecta region.

Figure 3

An illustrative example of a model spectra from a 10^{6-8} K plasma. Characteristic lines from various elements are indicated.

Figure 4a

X-ray spectral data for RCW 103 collected by Solid State Spectrometer (SSS) on the *HEAO-2* spacecraft are shown. Line blends corresponding to Kα emission from Mg, Si, and S are indicated. The part of the spectrum that is dominated by L shell emission from Fe is also indicated.

Figure 4b

X-ray spectral data for MSH 14-63 collected by the A-2 experiment on the *HEAO-2* spacecraft are shown. There are two sets data points- one from the Low Energy Detectors (LED) and one from the Medium Energy Detectors (MED). The LED data has been multiplied by 2 to improve the clarity of the plot. Line blends corresponding to Kα emission from S and Fe are indicated.

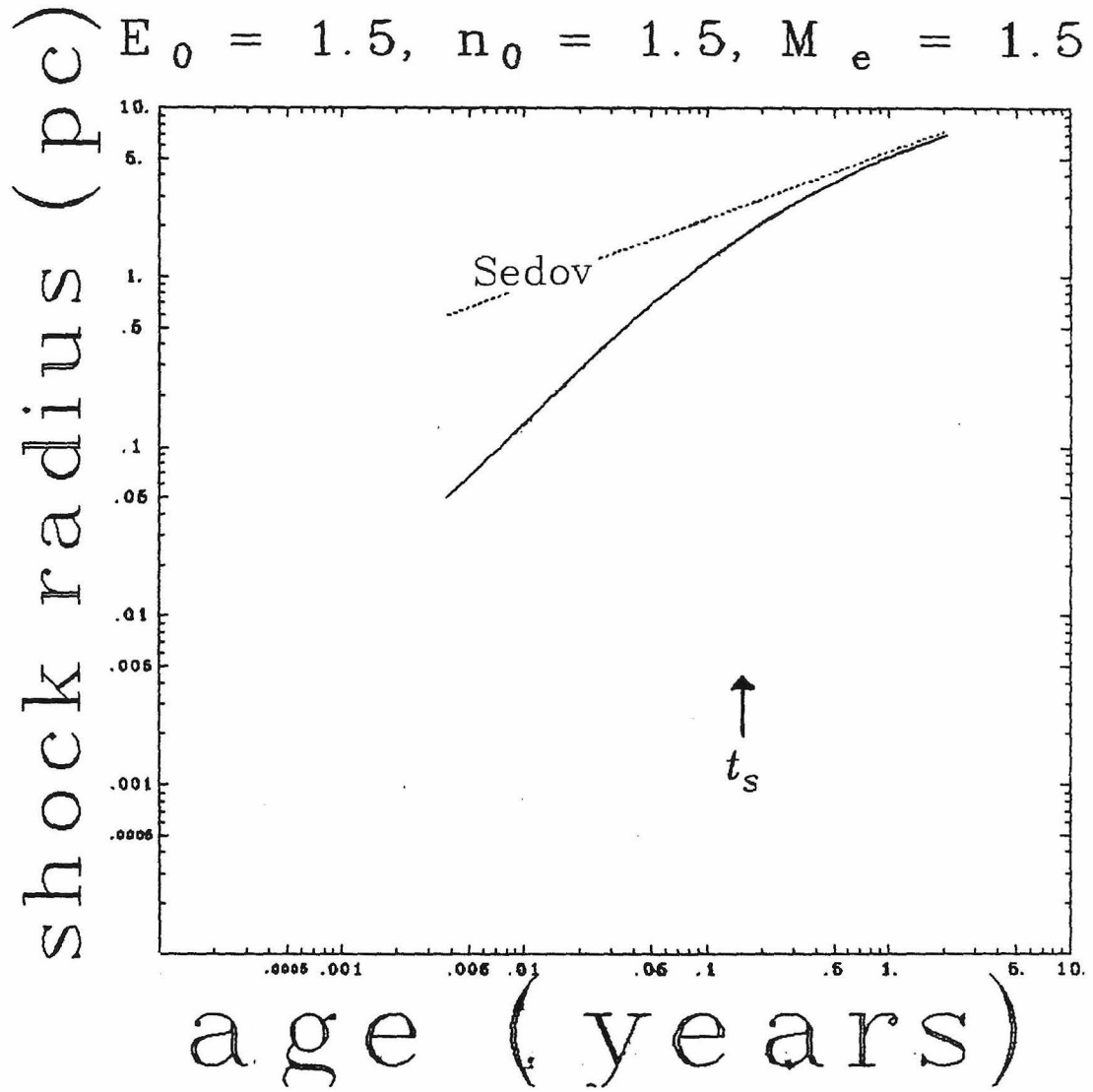
$E_0 = 1.5,\ n_0 = 1.5,\ M_e = 1.5$
shock radius (pc)
10.
5.
1.
.5
.1
.05
.01
.005
.001
.0005
.0005 .001
.005 .01
.05 .1
.5 1.
5. 10.
Sedov
t_s
age (years)

Figure 1

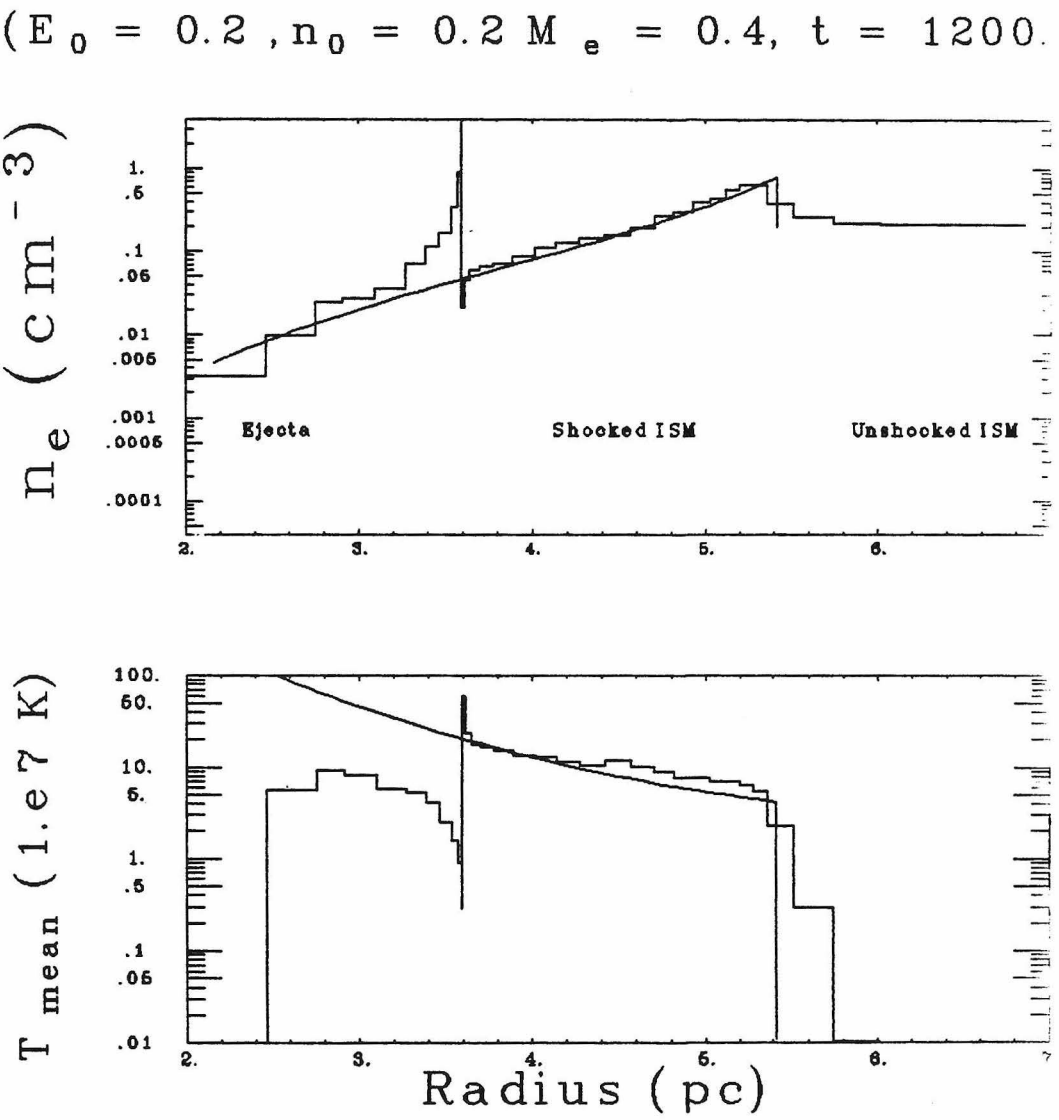
(E 0 = 0.2 , n 0 = 0.2 M e = 0.4, t = 1200.
n e (c m - 3)
1.
.5
.1
.05
.01
.005
.001
.0005
.0001
Ejecta
Shocked ISM
Unshocked ISM
2.
3.
4.
5.
6.
T mean (1.e7 K)
100.
50.
10.
5.
1.
.5
.1
.05
.01
2.
3.
4.
5.
6.
Radius (pc)

Figure 2

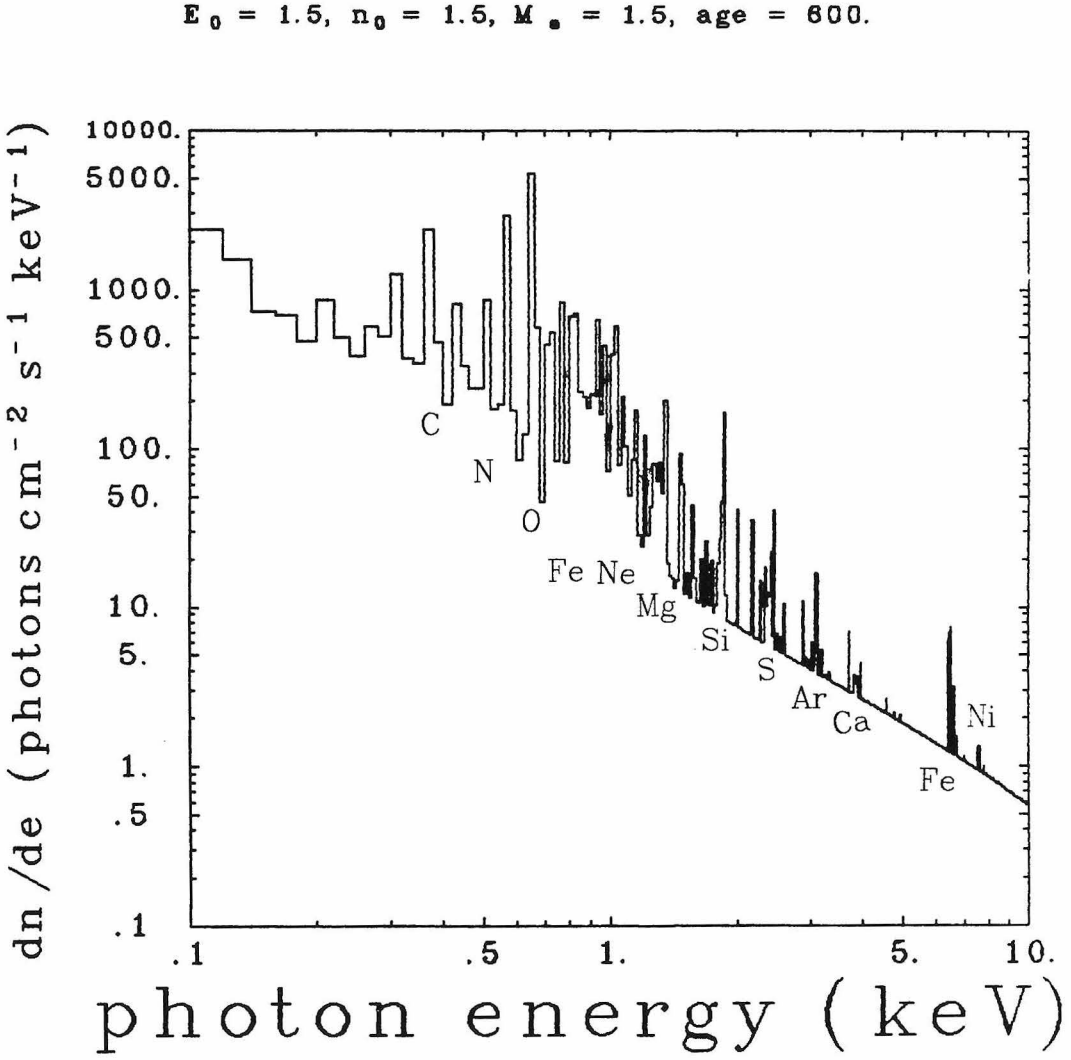
E 0 = 1.5, n0 = 1.5, M • = 1.5, age = 600.
dn /de (photons cm-2 s-1 keV-1)
10000.
5000.
1000.
500.
100.
50.
10.
5.
1.
.5
.1
.1
.5
1.
5.
10.
photon energy (keV)
C
N
O
Fe Ne
Mg
Si
S
Ar
Ca
Ni
Fe

Figure 3

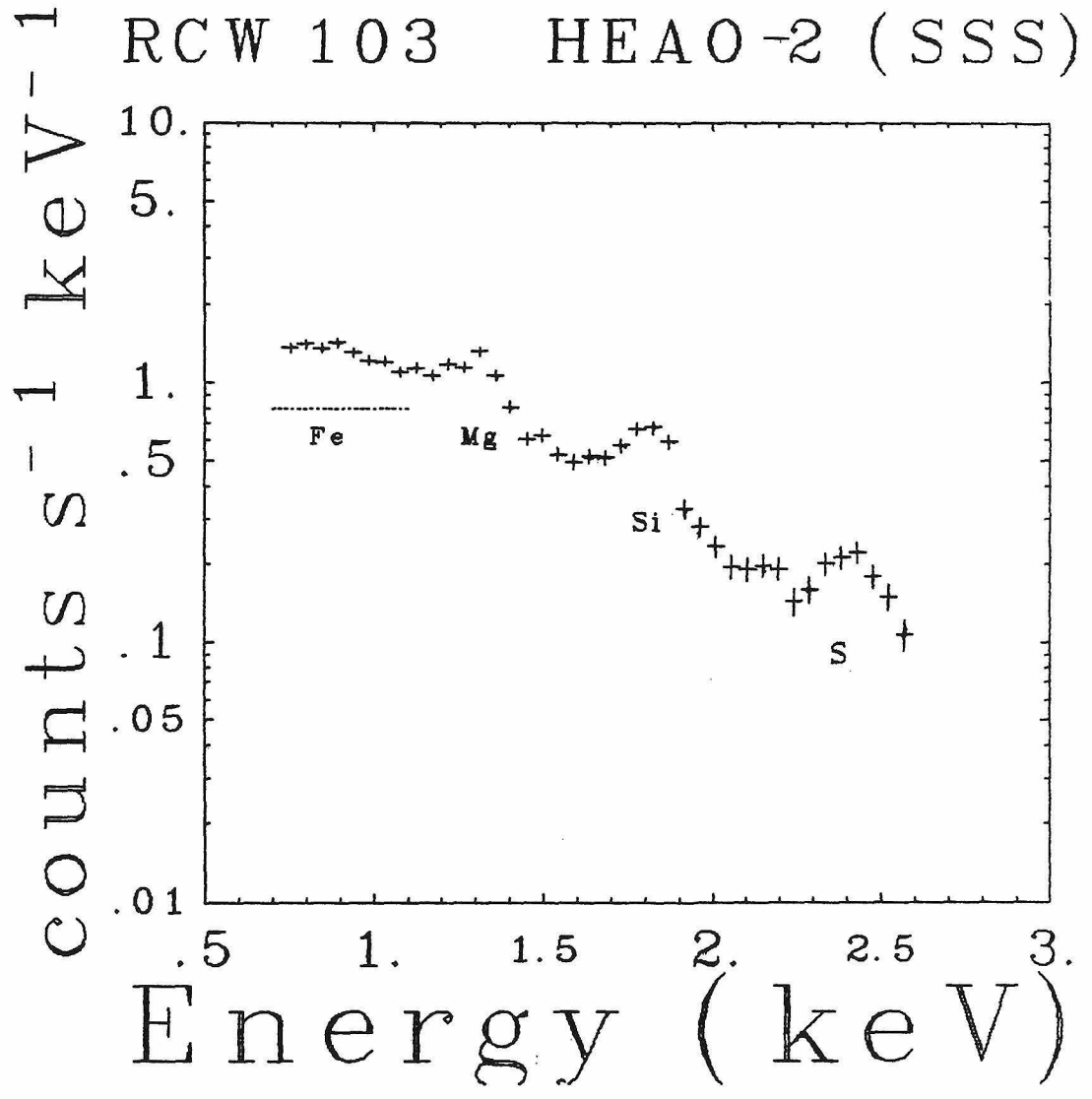
RCW 103 HEAO-2 (SSS)
counts s-1 keV-1
10.
5.
1.
.5
.1
.05
.01
Fe
Mg
Si
S
.5
1.
1.5
2.
2.5
3.
Energy (keV)

Figure 4a

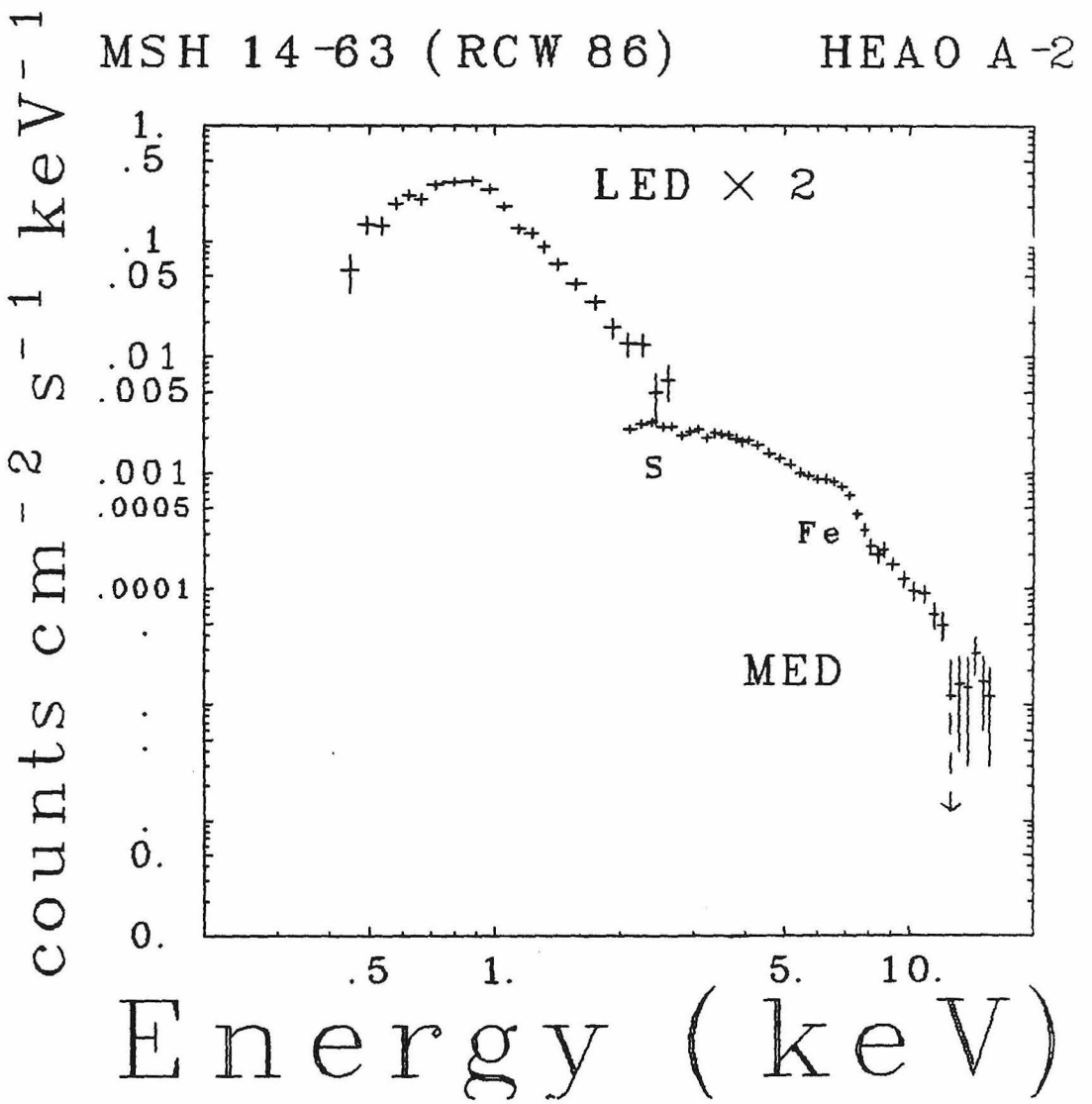
MSH 14-63 (RCW 86)
HEAO A-2
LED × 2
MED
S
Fe
counts cm⁻² s⁻¹ keV⁻¹
1.
.5
.1
.05
.01
.005
.001
.0005
.0001
0.
0.
.5
1.
5.
10.
Energy (keV)

Figure 4b

Chapter 2 : The NIE Model

Outline of the Model

This chapter gives only an overview of the NIE model. A more detailed account can be found in the Appendix of this thesis.

The hydrodynamics are calculated assuming a spherical supernova explosion of energy, E_0, which expands into a uniform ISM with particle density, n_0. The energy is assumed initially to be almost completely contained in the ballistic motions of the ejecta. The flow of the gas, except at shock fronts, is assumed to be adiabatic, so heat conduction and radiative cooling are neglected. An explicit set of finite-element equations representing the Lagrangian equations were used in the calculation. These equations, which were taken from Richtmyer and Morton (1967), included the artificial viscosity term, which acts as a dissipative mechanism at shock fronts. The number of spherical shells used for the ejecta was 13 and the number for the shocked ISM varied from 12 to 24. The number of shells was constrained by CPU memory and time considerations. Discontinuities in density at the ejecta/ISM interface and at the jump at the main forward shock were smoothed slightly because of the finite number of shells resulting in some minor underestimate of the emission from these regions relative to the rest of the remnant.

Thus, given E_0, n_0, and the mass of the ejected material, M_e, the mean temperature, T_m, and the electron density, n_e, can be calculated as a function of time and radius. The calculation of the electron temperature, T_e, depends on the question of non-Coulomb processes at the shock front. Two extreme cases will be examined. The first is to assume that the electrons come across the shock front "cold" and are subsequently heated by Coulomb-like collisions with the ions. The second is to assume that some mechanism at the shock front rapidly brings the electrons and ions into thermal equilibrium. Under those

conditions $T_e = T_i = T_m$.

Once the history of T_e and n_e in a given shell is known, the fractional population of ionic state with charge, z of an element with nuclear Z, can be found by integrating

$$\frac{1}{n_e}\frac{dX_{Z,z}}{dt} = i_{Z,z-1}X_{Z,z-1} - (i_{Z,z}+r_{Z,z})X_{Z,z} + r_{Z,z+1}X_{Z,z+1}$$

where $X_{Z,z}$ is the fractional population, $n_e i_{Z,z}$ is the rate for for an atom with nuclear Z in ionic state z to ionize to state $z+1$ via electron collisions, and $n_e r_{Z,z}$ is the rate for an atom with nuclear charge Z and ionic state z to recombine with an electron to form ionic state $z-1$. The fractional concentration is defined such that

$$\sum_{z=1}^{Z+1} X_{Z,z} = 1.$$

The set of values $\{X_{Z,1}, X_{Z,2}, \ldots, X_{Z,Z+1}\}$ shall hereafter referred as the ionization structure of the element with nuclear charge Z.

Some pre-ionization must occur in front of the shock for a collisionless shock front to form, but we will assume that the heavy elements all come across the shock front in relatively low states of ionization. Hydrogen and helium are assumed to be initially stripped. The rest of the elements considered and their given initial state are: C^{+4}, N^{+5}, O^{+5}, Ne^{+5}, Mg^{+5}, Si^{+5}, S^{+6}, Ar^{+6}, Ca^{+6}, Fe^{+6}, and Ni^{+6}. Because of the relatively large ionization rates that still occur at these early stages of ionization, the transient effects caused by this *ad hoc* choice of initial conditions should be eliminated in ~ 10 - 20 years.

The final step is to use the electron temperature, electron density, and ionization structure to calculate the spectrum from each element in each shell. A modified version of the Raymond and Smith plasma code (1977) is used. The

collisional excitation rates for He-like ions were changed to those calculated by Pradhan, Norcross, and Hummer (1981), which, unlike earlier calculations, included effects of autoionizing resonances. Also, a number of processes that produce Kα photons from iso-sequences with lower ionic charge than He-like ions have been added. The original Raymond and Smith code only considers innershell excitation for Li-like, Be-like, and occasionally B-like ions. This is sufficient in a CIE plasma because if the temperature is high enough to excite Kα emission from lower iso-sequences (*i.e.* if $T_e \gtrsim E_{K\alpha}$) then the iso-sequences below B-like are in very low concentrations. This is not necessarily the case when the plasma is in non-ionization equilibrium (NIE) especially for the higher Z elements. For the densities and time scales applicable in the SNR problem, we felt it was adequate to augment the Kα processes only for Ar, Ca, Fe, and Ni. Innershell excitation to the L-shell has been added, then, for all iso-sequences between Li-like and F-like ions of these elements. In addition, for these elements, innershell ionization for all iso-sequences below Li-like and the process of producing K shell vacancies via di-electronic recombination has been added for iso-sequences between Li-like and O-like. Both these processes result in Kα emission. Excitation rates, branching ratios, and resulting photon energies for these innershell processes are taken from Gronenschild (1979 and references within (eg Mewe, Schrijver, and Sylwester (1980)).

Parameterization of the model

The input parameters to the model and the units we will always use are the initial blast energy, E_0 (units of 10^{51} ergs), the density of the interstellar medium around the progenitor star, n_0 (units of 1 cm^{-3}), the amount of ejected mass from the progenitor star, M_e (units of $M_\odot$), the age of the remnant, t_3 (units of 1000 years), the abundance, relative to hydrogen, of elements in the

ejecta (normalized to the measured solar value), the abundance, relative to hydrogen, of elements in the ISM (normalized to the measured solar value), and the distance to the remnant, D (units of kpc). We also will define a "filling factor", f, that gives the fraction of the solid angle of the remnant that is filled with shocked plasma. Finally, we also fit for the amount of neutral hydrogen, N_H (units of 10^{22} cm^2) intervening between the remnant and the earth. This latter quantity parameterizes the energy dependent attenuation along the line of sight due to photoelectric absorption and scattering. The Fireman model (1974) was used for this calculation.

Since the calculation of the spectrum for a choice of E_0, n_0, M_e, and the age, t_3, takes a relatively large amount of computer time, it is necessary, in order to do spectral fitting, to interpolate from a grid. By exploiting a scaling law, we need only to store the results on a three dimensional grid. As discussed by a number of authors a given set of parameters E_0, n_0, M_e, t_3, and D does not produce a unique spectrum (eg Mansfield and Salpeter, 1977). An infinite set of those five parameters can be found that produce the same spectrum for the same abundance set. This degeneracy can be discussed in terms of a scaling parameter defined as

$$\alpha = \left[\frac{E_0}{n_0}\right]^{1/3}$$

as well as a number of "reduced" parameters:

$$\eta = (E_0 n_0^2)^{1/3} = \alpha^{-2} E_0 = \alpha n_0 ,$$

$$\beta = \frac{M_e}{E_0} = \eta^{-1} \alpha^{-2} M_e ,$$

and

$$\tau = \left(\frac{n_0}{E_0}\right)^{1/3} t_3 = \alpha^{-1} t_3 \ .$$

A fourth reduced parameter is the reduced emission volume, C_{ev}, which is defined as

$$C_{ev} \equiv \frac{\int n_e{}^2 dV}{4 \pi D^2}$$

and can be expressed as

$$C_{ev} = \frac{\alpha T_{ev}' f}{4\pi D^2}$$

where T_{ev}' is a function of η, β, and τ and is defined as

$$T_{ev}'(\eta,\beta,\tau) \equiv \alpha^{-1} \int n_e{}^2 dV \ .$$

We will quote C_{ev} in units of 10^{13} cm^{-5}.

These four reduced parameters, along with N_H and the abundance sets of the ejecta and ISM form the parameter space searched when fitting spectra. Once a point in this reduced space is determined to be the best fit, the next problem is to invert from the fitted parameters (η, β, τ, and C_{ev}) to the physical supernova parameters (E_0, n_0, M_e, t_3, f, and D). So far we have shown four equations for six unknowns. A fifth equation can be added that relates the angular radius of the shock front, Θ, a measured quantity, to R_s', which is defined by

$$R_s'(\beta,\tau) \equiv \alpha^{-1} R_s$$

where R_s is the true size of the shock radius and R_s' is a function of β and τ. Since $\Theta D = R_s$, we can write

$$R_s' = \alpha^{-1} \Theta D \ .$$

This still leaves the system of equations underdetermined by one variable. Our approach will be to assume f to be unity and show how the deduced parameters scale with f. Taking that approach, the equation for C_{ev} and the equation for R_s' can be combined to yield the following expression for α:

$$\alpha = \frac{T_{ev}'(\eta,\beta,\tau)\Theta^2}{4\pi R_s'^2(\beta,\tau)\ C_{ev}} f$$

With α, the input parameters are given by

$$E_0 = \alpha^2\eta \quad M_e = \alpha^2\eta\beta \quad t_3 = \alpha\tau \quad n_0 = \alpha^{-1}\eta$$

and the distance is given by

$$D = \frac{R_s'\alpha}{\Theta} \ .$$

Since α is directly proportional to f, each parameter scales with f as it scales with α.

We digress at this point to give some physical significance to this $\eta-\beta-\tau$ space. As can be seen from its definition above, β can be thought of as an "ejected mass-like" axis and τ can be thought of as an "age-like" axis. η can have a few different interpretations, but for our discussion it is best described as a "density-like" axis. The $\beta\tau$ plane is where the shape of the pertinent hydrodynamic variables, electron temperature and density as function of radius are determined. If we let λ be the ratio of the radius to the shock radius, then the temperature profile, $T(\lambda)$ and the density profile divided by η, $\eta^{-1}n(\lambda)$, are functions of β and τ only. Finally, α is measure of the mean x-ray surface brightness.

Various regions in this $\beta-\tau$ plane can be related to the different phases of the SNR evolution. An important quantity for discussing this demarcation is τ_s

which is given by

$$\tau_s = .16\beta^{5/6} \ .$$

When $\tau < \tau_s$ the remnant is in the so-called "free expansion phase". During this phase the ejecta dominates the hydrodynamics of the remnant which expands at a constant rate which depending upon the initial velocity of the ejecta. At $\tau = \tau_s$, the mass of the shocked ISM begins to exceed the mass of the ejecta, and the hydrodynamic profiles begin to approach those of the Sedov similarity solution for a point explosion (Sedov, 1959). The x-ray emission from the ejecta is significant for $\tau \lesssim 4\tau_s$. Beyond that time the contribution of the ejecta emission drops below a few percent of the total emission.

Increasing β increases the emission volume of the ejecta component relative to the emission volume of the shocked ISM and decreases the ratio of temperature in the shocked ejecta to the temperature in the shocked ISM. For $\tau<\tau_s$ the temperature of the shock region is inversely proportional to β as well. Increasing τ for a fixed β means a larger fraction of the x-ray emission comes from the shocked ISM as the shock wave sweeps up more interstellar matter. The temperature of the shocked ISM drops monotonically with increasing τ - slowly during the free expansion phase and like $\tau^{-6/5}$ during the Sedov phase. The temperature of the ejecta initially rises with τ during the formation of the reverse shock but later, at the times of interest for this work, it also decreases with increasing τ. For a fixed β and τ, η is a scaling factor for the density profile. $\eta\tau$ is proportional to $\int n_e \, dt$ which is the effective time for heating electrons in the "cold" electron model and the effective amount of time for evolving the ionization structure. Increasing η increases T_e / T_i (for Coulomb heating model only) and results in the ionization structure of the heavy elements to be closer to CIE.

Comparison with previous work

Early efforts for modeling non-equilibrium SNR, x-ray spectra were made by Itoh (1977, 1979). He constructed models with and without electron-ion thermal equilibration behind the shock front, but η and β were both fixed in his papers. The model in Itoh's 1979 paper was done with no ejecta at all. Concurrently with the model developed for this thesis, Shull (1982) and Hamilton, Sarazin, and Chevalier (HSC; 1982) have also devised similar models. Shull (1982) calculated models only with $\eta = 1$, with the no ejecta, and only with electron-ion thermal equilibration assumed. HSC calculate models varying in η and τ, for both electron-ion post shock equilibration and for only Coulomb electron heating, but again no ejecta contribution was considered. This work differs from these other efforts in that it includes the reverse-shocked ejecta as well as the shocked ISM. The models by Itoh (1979), HSC, and Shull rely exclusively on a Sedov similarity solution to provide the hydrodynamic substrate. This latter approach is equivalent to this work when $\tau >> \tau_s$ In this "far Sedov" limit the spectrum is completely independent of β, and, as is done in Shull (1982) and HSC, τ can be converted to a shock temperature as follows:

$$T_s = 5.2\,\tau^{-6/5}\ \text{keV} \quad .$$

We also note that the definition of η is slightly different in HSC. For comparison

$$\eta_{jjn} = \left[\frac{\eta_{HSC}}{10^{51}\ \text{ergs cm}^{-6}}\right]^{1/3} \quad .$$

This thesis also is among the first efforts at fitting spectral data with NIE models where η varys. (Shull and HSC currently have work in progress.)

These three other NIE models developed plus the one described here are nearly independent. At least two different methods for obtaining the hydrodynamic quantities, three or four different codes containing the atomic

processes, and different codes for integrating the electron temperature and ionization structure were employed in these computer models. Despite these differences and many other idiosyncratic differences, all models seem to agree with each other where it is possible to check. For software systems of this size ($\sim 10^4$ lines of code) and subtle complexities (numerous) this is not a trivial statement.

The Far Sedov limit

The Sedov limit will be an important limit in this thesis and a convenient limit for discussing some of the properties of the process of mapping fitted parameters to physical parameters. In this limit,

$$T_{ev}' \approx 3.3\times10^{58}\,\eta^2\tau^{6/5} \quad \mathrm{cm}^{-3} \quad ,$$

and

$$R_s' \approx 1.5 \times 10^{19}\,\tau^{2/5}\ \mathrm{cm}$$

From these relations, α for a Sedov limit model is given as

$$\alpha = .1\,f\,\frac{\eta^2\tau^{2/5}\Theta^2_{arcmin}}{C_{13}}$$

where Θ_{arcmin} is the angular radius in units minutes of arc and C_{13} is C_{ev} in units of $10^{13}\ \mathrm{cm}^{-5}$. f, again, is a filling factor. The distance is given by

$$D = 18\frac{\alpha\tau^{2/5}}{\Theta_{arcmin}}\mathrm{kpc} \quad .$$

As can be seen from above, in the Sedov limit the final set of parameters scale quite differently with η, τ, and f:

$$E_0 \sim \eta^5\tau^{4/5}f^2 \quad t_3 \sim \eta^2\tau^{7/5}f \quad D \sim \eta^2\tau^{4/5}f \quad n_0 \sim \eta^{-1}\tau^{-2/5}f^{-1}$$

The higher the powers to which η, τ, and f are raised the more severe the error propagation. So E_0 is the least well determined while n_0 is the best determined. This leads us to Nugent's Corollary of Murphy's Law of SNR modeling: "The more interesting a parameter, the more poorly it is constrained.". While the blast energy, an important parameter for such issues as stellar evolution and nucleosynthesis of heavy elements, is typically uncertain by an order of magnitude, we can, with dazzling precision, measure the amount of garbage around the progenitor star.

In the way of a digression, the reader may be bothered that D is an output of the model as opposed to an input. In previous x-ray papers discussing SNR's, the parameters known were T_e (from which T_s could be inferred under the assumption that $T_e = T_m$), the angular radius, and the x-ray flux. There were three equations relating these measured quantities to E_0, n_0, t, and D. Since there were four "unknowns", one had to be fixed so that the other three could be determined. Unless the age was known from historical records, the distance was usually the best determined "unknown". Heuristically speaking, with the advent of the NIE models another quantity, namely $\int n_e dt$, is measured from the amount of ionization heating and, possibly, from the amount of Coulomb heating. This gives a fourth equation so that all parameters can be determined.

Most distance estimates to SNR's rely on the empirical $\Sigma - D$ technique using radio measurements. In some cases, additional estimates have come from analyzing historical records of the peak apparent magnitude of the supernovae event, or the assumption that the progenitor star was a member of a certain star cluster. The use of NIE models in fitting x-ray spectral data represents an independent measure of the distance that arises from a non-empirical, physical model.

Caveats

Before proceeding to discuss the fits of the NIE model to x-ray spectral data, a few caveats are in order. First, despite the touting above, some care must be taken in accepting the inferred values of E_0, n_0, t, M_e, and D. Their rather fragile derivation could be destroyed by a number of systematic problems. Some of the problems that are suspected or are known to exist in SNR's include: inhomogenities may exist in the ISM; the ejecta/ISM interface is Rayleigh-Taylor unstable; and shocks might not form over the entire solid angle of the remnant. Heat conduction may be another important effect, especially if dense ejecta or ISM clouds are heated to shock temperatures. All of these may have a profound effect on the emergent spectrum. In addition to these hydrodynamic considerations, systematic uncertainties in the atomic physics as well as detector modeling could also swamp any of the statistical uncertainties.

In order to put the NIE model in perspective, a brief review of the history of x-ray spectral modeling of SNR emission is helpful. At first, multi-temperature thermal bremsstrahlung models were fit to the data with the caveat that line emission and non-equilibrium effects were being ignored. Then as data and theoretical work improved multi-temperature CIE models that included the line emission were employed. The lack of line emission was no longer a problem but non-equilibrium conditions along with the number of problems outlined above still were. These models were taken to be parametrizations of the problem, but it was always the expectation of the observer that the parameters derived were indicative of the real remnant. With the introduction of the NIE model, the lack of consideration of the non-equilibrium effects has been removed. In light of the caveats given above, it is safest to still view the NIE model as a parametrization. To a rough approximation the model is representing a plasma with a characteristic electron temperature and an effective ionization time (possibly a second

plasma if the ejecta is a significant component to the emission). As was discussed above, before NIE models the angular size, x-ray flux, and implied temperature were used to derive remnant parameters. The NIE model has added another measurement, the effective ionization time, and otherwise improved the derivation procedure; however, the basic idea is the same as before.

Chapter 3: Observations of MSH 14-63 (RCW 86)

Introduction

MSH 14-63 is the most likely candidate for the supernova recorded by the Chinese in A.D. 185 (Clark and Stephenson, 1977). While MSH 14-63 is the name of the radio source, an alias for the remnant is RCW 86, which is the designation of the optical filaments. Following the discovery of MSH 14-63 (Hill, 1967), other early radio maps clearly resolved a limb brightened shell with an angular radius of ~20 arcmin (Caswell *et al.*, 1975). Westerlund (1969a) suggested that the remnant was associated with an OB association. If this were the case, a Type II supernova would be indicated on the basis of stellar type. By using spectrophotometric studies, Westerlund determined the distance to the association to be 2.5 kpc. This measurement is in agreement with the measurement of the distance made by the $\Sigma - D$ technique.

The first x-ray observation of MSH 14-63 was made by Naranan *et al.* (1977) in the range 0.5 to 2.5 keV using an experiment on the *Apollo-Soyuz* mission. The observation was taken in the range 0.5 to 2.5 keV. The spectrum in the range of 1 to 30 keV obtained from the *OSO-7* spacecraft was reported by Winkler (1978). Winkler found that the combined spectrum of the two observations could not be explained by a simple thermal spectrum with a single temperature. Rather, two components each at different temperatures were needed to adequately explain the data. The temperature of the high-temperature component, which is presumed to be produced by the shocked ISM, was measured to be greater than 5 keV. The low temperature component, measured to be 0.22 keV, was attributed to the supernova ejecta which had been heated by inward propagating shock (McKee, 1974; Gull, 1973, 1975). Using this reverse-shock model, Winkler determined an ejected mass of greater than 5 $M_\odot$ is required. Winkler concluded that the x-ray spectral data supported the idea that MSH 14-

63 was formed from a Type II supernova located in the OB association studied by Westerlund.

Because of increased spectral resolution and sensitivity of observations, most recent attempts to explain the SNR spectral data have employed more sophisticated models to predict the x-ray spectrum from hot, optically thin plasmas than the simple exponential spectrum used by Winkler. These models explicitly calculate the contributions from each element in the plasma to the continuum emission as well as the the line emission (Tucker and Koren; 1971, Kato, 1976; Raymond and Smith, 1977; Shull, 1981). For a large range of conditions of the plasma line emission from heavy elements ($Z \geq 6$) dominates the spectrum, and as was discussed in the last chapter, a simplifying assumption that is often made is that the plasma is in collisional ionization equilibrium (CIE).

In this chapter we will present results of both CIE and NIE models with data collected from MSH 14-63 by the A-2 experiment on the HEAO-1 spacecraft.

Observations

The observations were made by two different detectors of the A-2 experiment (Rothschild *et al.*,1979) on board the HEAO-1 satellite. The low energy pulse height data (.5 - 3 keV) were obtained using the on-axis LED detector while the spacecraft was in a scanning mode. The high energy pulse height data (2 - 15 keV) were taken during a pointed observations using the MED detector.

Each detector had two separate co-aligned fields of view. Roughly, the dimensions of these two fields were 1°.5 × 3° full width at half maximum (FWHM) and 3° × 3° (FWHM). The data from both of these fields were combined to obtain the final data set used for the analysis. The dimensions of all the fields of view of the detector were larger than the dimensions of MSH 14-63 (diameter of 40 arcmin), so the data represent the integral over the entire surface brightness of

the remnant.

The LED detectors had a sensitivity to photons as low in energy as 0.18 keV; however, because of contamination from α Centauri (Nugent and Garmire, 1978) the lowest energy data were not used. Since interstellar absorption of the spectrum from MSH 14-63 is so great at energies below 0.5 keV, this was not a significant loss of information. α Centauri is measured to have a steeply falling spectrum ($kT_e \lesssim 0.15$ keV) and in broad band measurements in the energy range above 0.5 keV α Centauri has a count rate $\lesssim .04$ that of MSH 14-63 (Nugent *et al.*, 1982). These facts, combined with fact that the collimator transmission to α Centauri during the MSH 14-63 observations was $\lesssim 0.2$, gives us confidence that there has been no significant contamination of the pulse height data above 0.5 keV.

CIE Fits

We will first discuss fits of CIE models to the MSH 14-63 data - both a single temperature plasma and two-temperature plasma. There are three reasons for this digression:

1) Because bremsstrahlung and radiative recombination from hydrogen and helium dominate the spectrum at photons energies $\gtrsim 4.5$ keV, the electron temperature and reduced emission volume alone determine the shape and magnitude of the spectrum. The determination of the temperature, as we will discuss, will eliminate the Coulomb heating models.

2) Since only a two-temperature model was used by Winkler, we would like to apply the same model for purposes of comparison.

3) We would like to demonstrate how poorly a single temperature CIE model fits the data, before proceeding with NIE model fits.

Two-temperature CIE models assume two separate coronal plasmas of different temperatures. In addition to the temperatures and the reduced emission volumes of the two different components, other parameters are the elemental abundances of the two components, and the interstellar absorption column, N_H.

The results of the fit are shown in Figure 1a. A reduced χ^2 of 1.6 for 60 degrees of freedom is obtained. The only elemental abundance that was allowed to vary was iron. The results of the fit are shown in Table 1. The parameter of particular interest to this discussion is the higher temperature , 5.1 keV, which will be denoted, $T_{e,high}$. As mentioned above, at photon energies $\gtrsim$ 4.5 keV the spectrum is dominated by continuum emission from hydrogen and helium and, hence, $T_{e,high}$ is insensitive to NIE effects.

An important result from this value of $T_{e,high}$ is that we exclude the whole branch of NIE models which assume the electrons are heated by Coulomb collisions. Cox and Anderson (1982), using analytic approximations to the Sedov solutions for the temperature and densities in the interior of the remnant and analytic approximations for Coulomb heating, showed that the electron temperature is independent of radius for times shorter than $\sim 3000 E_{51}^{3/14} n_0^{-4/7}$. This "plateau" temperature as a function of time is given by

$$T_e \approx 1.5 \left[\frac{t}{1800 \text{ years}}\right]^{-2/25} \left[\frac{E_0}{10^{51} \text{ ergs}}\right]^{4/25} \left[\frac{n_0}{1 \text{ cm}^{-3}}\right]^{6/25} \text{ keV} .$$

In terms of our fitting parameters this equation becomes

$$T_e \approx 1.6 \, \tau^{-2/25} \, \eta^{2/5} \text{ keV}$$

As an example, Figure 2 shows the results of numerically modeling coulomb heating for $\eta = 0.2$ and $\tau = 1.2$. The two top graphs show the density and mean temperature shown with a analytic Sedov solution. The third graph shows the electron temperature assuming Coulomb heating only. The dotted line which displays Cox and Anderson's approximate solution demonstrates excellent agreement.

Because T_e is insensitive to the choice of parameters, an attempt to find a choice for D, E_0, and n_0 that allows $T_e = T_{e,high}$ and satisfies the constraints for angular radius and reduced emission volume produces an absurd result. To wit: $D \sim 41$ Mpc, $E_0 = 3 \times 10^{70}$ ergs, and $n_0 = 6 \times 10^{-4}$ cm^{-3}. We will safely ignore the possibility, then, that the electrons are "cold" after having crossed the shock fromt.

Saying that there exists at the shock front some mechanism other than Coulomb interactions to couple the electrons to the ions does not prove that the mechanism will be sufficient to bring the electrons and ions into thermal equilibrium If, after passing through the shock, the electrons have obtained a significant fraction but not the total amount of their equilibrium energy, then the time scale for them to reach equilibrium would still be as above. The only difference would be that the electron temperatures would be higher than those derived by Cox and Anderson (1982).

Before exploring the fits using the NIE models, we wish to emphasize that a single high temperature component does not fit the data at low photon energies. Figure 1b shows only the 5.1 keV component with a reduced emission volume as fitted in the two-temperature model. The flux at 1 keV differs from the predicted flux by a factor of ~ 10.

Review of Parameters

Before discussing results of the model, we briefly review for the reader the definitions of the parameters used. The input parameters to the model and the units we will always use are the initial blast energy, E_0 (units of 10^{51} ergs), the density of the interstellar medium around the progenitor star, n_0 (units of 1 cm^{-3}), the amount of ejected mass from the progenitor star, M_e (units of $M_\odot$), the age of the remnant, t_3 (units of 1000 years), the abundance, relative to hydrogen, of elements in the ejecta (normalized to the measured solar value), the abundance, relative to hydrogen, of elements in the ISM (normalized to the measured solar value), and the distance to the remnant, D (units of kpc). These parameters are mapped to more convenient set of parameters for purposes of the doing spectral fitting. There is a scaling parameter defined as

$$\alpha = \left(\frac{E_0}{n_0}\right)^{1/3}$$

and a number of "reduced" parameters:

$$\eta = (E_0 n_0^2)^{1/3} = \alpha^{-2} E_0 = \alpha n_0 ,$$

$$\beta = \frac{M_e}{E_0} = \eta^{-1} \alpha^{-2} M_e ,$$

and

$$\tau = \left(\frac{n_0}{E_0}\right)^{1/3} t_3 = \alpha^{-1} t_3 .$$

A fourth reduced parameter is the reduced emission volume, C_{ev}, which is defined as

$$C_{ev} \equiv \frac{\int n_e^2 dV}{4 \pi D^2} .$$

η, τ, β, and C_{ev} are derived from fits to the spectral data. α is then determined from the average x-ray surface brightness by

$$\alpha = \frac{\Sigma'(\eta,\beta,\tau)\Theta^2}{C_{ev}} f$$

where Σ' is determined from η, β, and τ and f is fraction of solid angle of the remnant filled with shocked plasma. The value of f will nominally be assumed to equal unity. With α, the input parameters are given by

$$E_0 = \alpha^2\eta \quad M_e = \alpha^2\eta\beta \quad t_3 = \alpha\tau \quad n_0 = \alpha^{-1}\eta$$

and the distance is given by

$$D = \frac{R_s'(\beta,\tau)\alpha}{\Theta} \quad .$$

where R_s' is a constant determined from the fitted value of β and τ.

When $\tau \gtrsim .16\beta^{5/6}$ the remnant is in a Sedov phase and the shock temperature, T_s, can be given as a function of τ by

$$T_s = 5.2\ \tau^{-6/5}\ \text{keV} \quad .$$

Non-Ionization Equilibrium Models / $T_e = T_i$

We are going to assume for the balance of this paper that whatever mechanism is responsible for coupling electrons to ions at the shock front will bring them to equilibrium on an ignorably short time scale. Under this assumption then we will always assume that $T_e = T_i = T_m$.

The parameter β, as it turned out, is not a well constrained parameter for this data set. Results of fitting the data with models that have relatively high values of β will be discussed below; however, we will assume, for simplicity and

definitiveness, during most of the discussion of the MSH 14-63 data that $\beta = 1$. Since the values of τ that fit the data under this assumption are ~1.1, a deliberate consequence of this choice of β is that we will be working in the Sedov limit. There are three advantages to this:

1) Working in a regime of parameter space where emission from the shocked ISM dominates the spectrum is deemed preferable to working in regime where the reversed shocked ejecta was dominant since the modeling of the latter is more controversial.

2) Since the spectrum is insensitive to β in this limit, the results of the fit are also insensitive to the precise choice of β, other than it is sufficiently low.

3) Models that are in the Sedov limit make possible direct comparisons with the work of Shull (1982) and Hamilton *et al.* (1982).

In addition to fitting for C_{ev}, N_H, η, and τ, we also allowed the abundances for Fe, S, and Si to vary. The abundances for the rest of the elements were fixed at solar values as given by Allen (1976). The results of the best fit are displayed in Table 2 along with the input parameters inferred from assuming the radius of the remnant to be 20 arcmin. Figure 3 shows a display of the best fit and an insert showing the dependence of χ^2 on η and τ. This χ^2 grid is calculated by fixing the values of η and τ and letting the balance of the parameters vary. The inner contour is for change of χ^2 from minimum of 4.6 which corresponds to the minimum volume 90% confidence region for 2 parameters (Lampton *et al.*, 1976). For comparison, a contour for $\Delta\chi^2 = 10$ is also shown. The results of fits that are done at two extremes of the 90% region are shown in Table 2.

We will now discuss various aspects of this fit:

Elemental Abundances

The over-abundance of the S and Fe was needed primarily to fit the K_α lines at 2.4 and 6.7 keV. Because L shell emission from iron is a major contributor to

the spectrum at ~1 keV, the reader may be concerned that the overabundance was required to match the flux in the LED data. To demonstrate that this is not the case and that a solar abundance composition can fit the data with the exception of the lines, we have also performed a fit where all the elemental abundances in the NIE model were fixed at solar, and lines were inserted, *ad hoc*, at the Kα energies of S, Fe, and Ar (2.4, 3.0, and 6.7 keV, respectively) to compensate for the missing flux at those photon energies and in effect neutralize the influence of the lines in the fit. The results of the fit are given in Table 3 and the fit shown in Figure 4.

The effect of changing the Fe abundance does have an effect on other parameters. In this case, increasing η has the effect of compensating for the lowered elemental abundances since the population of Fe XVII and Fe XVIII, both important 1 keV L-shell emitters, increase dramatically as η is raised from 0.15 to 0.3.

Density, age, and N_H

The fit to the combined LED/MED data gives good agreement to other known properties of MSH 14-63. The density of 0.1 - 0.3 is reasonable for the height of the remnant off the galactic plane ($\approx$ 80 (D / 2 kpc) pc). The measured value of N_H would imply an average hydrogen density along the line of sight to the remnant of ~ 0.7 (2 kpc / D). This is also a reasonable value considering the angle of the remnant off the galactic plane.

Most importantly, the fitted values of the age are in reasonable agreement with the age of 1800 years known from Chinese astronomical records. Alternatively, if one assumes an age of 1800 years, then the average x-ray surface brightness is consistent the measured value. This not a trivial statement since the average x-ray surface brightness scales as η^2. A large fraction of the volume of the remnant cannot be filled with a plasma which had a much higher η than

those fitted above.

Fe K_α line

The Fe K_α is an attractive feature for study because it is prominent and measurement of the surrounding continuum is easy. The line is composed of a blend of lines around ~ 6.6 keV from many different ionic species of iron. There are two anomalies concerning the line in the NIE model:

1) An over-abundance of iron must be assumed to explain the equivalent width of the feature.

2) The centroid of the line feature in the data is apparently shifted to higher energies with respect to the predicted line feature. These shifts in the centroid are ~ 150 ev to lower energies. Doppler shifts can probably be ruled out since the shock velocity implied from the x-ray temperature could at most produce a shift of ~40 ev if all the iron-line emitting material was on the far side of the remnant.

In a 5 keV plasma which is in CIE, the most prominent lines arise from H-like and, more so, He-like ions, but when the plasma is out of CIE the population of these ions can be severly diminished. Given the ionization time, $(\int n_e\, dt)$, in MSH 14-63, predicted by the above NIE fits the prominent iso-sequences are S-like to F-like ions. The emission, which results following innershell ionizations of these ions, has photon energies of ~200 ev lower then the characteristic Kα radiation from He-like and H-like ions. At greater ionization times the ionization structure becomes more advanced. The characteristic energy of the line photons increases with increasing ionic charge. The efficiency of ions below C-like for producing K_α is generally lower than the strong He-like ion by a factor of ~3. The C, B, and Be-like ions, on the other hand, produce comparable amounts of Kα from innershell excitations via dielectronic recombination.

To reconcile the observed iron feature in the MSH 14-63 data two requirements in some region are required. First, in order to produce Fe Kα emission at all, $T_e \gtrsim 5$ keV. Second, the effective ionization time would have to be $\gtrsim 5$ times that of the models used in the fits above. The latter requirement is necessary to start populating the ionic states at or above the C-like isosequence. The characteristic radiation from these ions is not only at higher photon energies, but, again, these ions also have higher efficiencies for producing Kα.

In order to quantify this discussion, we will perform NIE model fits on just the data $\gtrsim 4.5$ keV. Using these data will avoid many assumptions involved with fitting the data at lower energies which are dominated by line emission. We will consider only four parameters: η, τ, C_{ev}, and the abundance of iron, A_{Fe}. The amount of N_H, which only marginally affects the data at these energies was fixed at the fitted value from above and the abundances of all other elements were fixed at solar. In way of review before proceeding, τ is primarily responsible for the shape of the continuum, $\eta\tau$ is proportional to $\int n_e dt$, A_{Fe} is proportional to the equivalent width (strength) of the line, and C_{ev} acts as a overall scale factor. τ and C_{ev} are well determined by the continuum and will not change by more than 10% for this discussion.

Figure 5a shows a fit done with η fixed at 0.2 and the balance of the parameters left to vary. The non-iron contributions to the spectra have been subtracted. As noted above, the model shows a distinct shift of ~150 ev to lower energies and an abundance enhancement of factor of 3.2 over solar is needed to explain the intensity of the feature. If we now unpin the value of η, a best fit is obtained with a value of η = 3.1. This fit is displayed in Figure 5b. Not only does the line fit better at this value of η (The improvement in χ^2 was ~ 11.), but it does so with an abundance much closer to solar. The 95% confidence region (2σ) for η ranged from 1 to 6. (Even at η = 6 there are still significant deviations

from CIE.)

Finally the same region was a fit with a CIE model. Now a single electron temperature, T, has replaced τ. The fit, displayed in Figure 5c, also shows a well centered line with near solar abundance; however, the CIE model predicts too much emission at ~ 8 keV. This line feature, which has been referred to as Kβ (eg. Pravdo and Smith, 1979), contains n=3 to n=1 transitions from H-like and He-like Fe and Kα emission from Ni. The Fe component tends to dominate because Ni is less abundant than Fe by a factor of ~18. The ratio of Kβ to Kα has been used by Pravdo and Smith as a diagnostic for CIE since it is very sensitive to the population of the He and H-like ions in Fe. The χ^2 of the fit to data points between ~ 5.5 keV and ~ 9 keV increased by 12.1 from best fit NIE to best fit CIE. This increase, which is evidence against the plasma being in CIE, came primarily from contributions around the Kβ feature.

Taking the best fit value of η from the Fe-line fits what can one say about the remnant? First, because the surface brightness (or α) scales as η^2, we can rule out a model where plasma of this nature fills the entire volume of the remnant. For filling factors near unity, the distance would need to be 200 kpc and the age, 3×10^6 years. Filling factors of ~1% would be adequate, although we know from x-ray images probably 50-75% of the remnant is filled with plasma. These x-ray images (Pisarski, private communication) show a limb brightened shell that has large variations in surface brightness as a function of angle around the ring - the brightest region behind in the SW. In addition there are noticeable deviations from a circular ring. There is some correlation for brighter regions to have a smaller radius of curvature. All of this suggests that there probably are density inhomogenities on various different size scales present in the remnant.

Since the models calculated above assume a homogeneous ISM, they are what we would call "single-η" model. What the spectral data and the x-ray image seem to require is, in a sense, a "multi-η" model. Somewhat analogous to "two-temperature" models, we would argue for low η's to explain the shape and flux of the low energy emission and high η's to explain the shape and flux of the high energy lines.

The high-η components could for example be explained as dense cloudlets that are heated by conduction to temperatures of the post-shock region. Another possible source of material in the remnant with high ionization time is the ejecta. The reverse shock cannot be the source of the Kα emission since the temperatures are not high enough (McKee, 1974; Gull, 1974,1975). There have been two mechanisms suggested for mixing the ejecta into the hotter, shocked ISM regions - neither was appropriate for inclusion in one-dimensional hydrodynamic model. If the ejecta was initially in a smooth shell, the contact surface between the shell and the shocked ISM would become Rayleigh-Taylor unstable (eg Gull 1975). Fingers of this dense ejecta material could then break away from the rest of the ejected material and be heated to temperatures comparable to the shocked ISM by heat conduction (Chevalier, 1975). Alternatively, some of the ejecta could initially be in clumps to begin with (Chevalier 1977). In addition to being heated by shock waves due to pressure differences between the clump interior and the shocked ISM, the higher temperatures could, again, be obtained by heat conduction.

Distance

We turn our attention next to the question of the distance to MSH 14-63. As mentioned in the introduction, Westerlund (1969a) has measured the distance to a OB star association in the direction of MSH 14-63 by spectrophotometric technique. He finds a distance modulus of 12.0 ± 0.2 which corresponds to a distance

2.5 kpc with an uncertainty of roughly 0.2 kpc. This is inconsistent with the distances related to the x-ray measurements discussed here which argue for the distance being much closer (~1.6 kpc).

Given that the age is known, the best method for discussing the limits on the distance by x-ray measurements is, again, to work only with data above 4.5 keV. Here the only assumptions are that the remnant can be approximated by a Sedov blast wave, that the electron temperature is equal to the mean temperature, that the age is 1800 years, and that the angular radius of the shock front is 20 arcmin. The distance is then given as

$$D = 1.6 \left[\frac{\Theta}{20\text{arcmin}}\right]^{-1} \left[\frac{t_3}{1800\text{ years}}\right] \tau^{-3/5} \text{ kpc} \quad .$$

The minimum volume 95% confidence region (2σ) in τ extends from 0.9 to 1.2. The lower limit of 0.9 (an upper limit on the shock temperature of ~6 keV) gives an upper limit on the distance of 1.7 kpc. For the x-ray determined distance to agree with Westerlund result would require $\tau \approx 0.55$ (plasma temperatures of 12-15 keV), which can be ruled out. It is, of course, possible that the progenitor for MSH 14-63 was not a member of Westerlund's OB association; however, we do point out that any deviations from the assumptions stated above would tend to make us underestimate the distance.

First, even though the longest angular dimension of the x-ray emission is 40 arcmin, the brightest regions - those dominating the x-ray spectra - appear to have a smaller radius of curvature, maybe as small as 15 arcmin. Second, if, despite some non-Coulomb electron heating at the shock front, T_e is still less than T_i, than the shock temperature would be underestimated by our measurement of T_x. Finally, the introduction of density inhomogenities into the remnant can alter the interpretation. If, for example, after expanding for a significant

part of its lifetime, the shock in the SW part of MSH 14-63 moved into a denser region, the shock temperature would be lower than the radius would imply. Finally, while a temperature of 12-15 keV can be ruled out if the x-rays were all arising from a post-Sedov shock, a thin, hot component related to the post-shock regions could exist that was being overwhelmed by cooler emission from denser regions. The observations lack the sensitivity to detect such a hot component under these conditions.

A lower limit can be set for the distance by assuming that the remnant is still in the early free expansion phase. A lower limit of the kinetic temperature of the shock of 5 keV would imply a constant expansion velocity of 2100 km s^{-1}. Assuming, again, an age of 1800 years and an angular radius of 20 arcmin yields a lower limit on the distance of 700 pc.

Emission from the ejecta

The value of β has consequences for demonstrating the existence of the reverse-shock ejecta component and measuring the mass of the ejected material. As was mentioned above, β was not a well constrained parameter. We fit the data with values of β ranging from 1 to 10 with no more than a change of roughly unity in the value of χ^2. At low values of β the ejecta was only a few percent of the total emission at $\sim$ 1 keV and, thus, did not significantly effect the spectrum. At higher values of β the fraction of emission from the ejecta became dominant but the temperature of the ejecta decreases. The ejecta's dominance of the spectrum occurred at less than 0.5 keV where interstellar absorption makes observations difficult. The amount of emission from the ejecta was comparable to the shocked ISM at $\sim$ 1 keV, but as with discussion on the iron abundance, varying the value of η, which varied the contribution to the $\sim$ 1 keV emission from the shocked ISM, could compensate for any changes in the ejecta emission. In low resolution we were not able to decouple the components.

Using much the same argument for providing a lower limit to the distance we can put an upper limit on the size of β of $\sim$ 40. Any value higher than that would produce shock velocities that were too low to produce a 5 keV plasma during the lifetime of the remnant.

Blast Energy

Knowledge of the blast energy has a direct application to accessing whether the progenitor of MSH 14-63 is a Type I or Type II supernova. The issue of the association of MSH 14-63 with the OB star group also relates the question of the type of SN explosion that formed the remnant. The association would strongly suggest that the MSH 14-63 was a Type II supernovae (Shklovsky, 1962), since Type II supernova are thought to occur in massive stars.

The results of the standard NIE model with β fixed at unity which are given in Table 2 would indicate that the blast energy, E_0, was $\lesssim 6 \times 10^{50}$ ergs. However, as the discussion in Chapter 2 pointed out, E_0 is a very sensitive function of η. Fixing the abundances to solar, for example, moved the inferred value of the blast energy up to $\sim 1.2 \times 10^{51}$ ergs. This large range of uncertainty in E_0 along with the large range of uncertainty in the mass of the ejecta, M_e does not allow an unambiguous assertion as to the type of supernova explosion.

[Fe XIV] Emission

Lucke *et al.* (1979) have made measurements of the [Fe XIV] λ5303 emission line in RCW86. They observed a flux of $2.28 \pm .98 \times 10^{-14}$ ergs cm^{-2} s^{-1} from summing four 5 arcmin circular fields in the SW part of the remnant at the shock front. The dereddened flux was given as 1.4×10^{-12} ergs cm^{-2} s^{-1}. In CIE, [Fe XIV] emission peaks rather sharply at 2.1×10^6 K. For CIE plasmas with $T_e \lesssim 1.5 \times 10^6$ K or $T_e \gtrsim 3.0 \times 10^6$ K the emissivity of the λ5303 line drops precipitously as a function of temperature. The authors interpreted their observation

in terms of the two-temperature model fit to the x-ray data. They ignored the high-temperature blast-wave component, because under the assumption of CIE the amount of [Fe XIV] emission would be negligible at the measured temperature of 6×10^7 K. Rather, they suggested associating their flux with the alleged low-temperature x-ray component ($2.5 < T_6 < 6$) or an even lower temperature component which they argue would be difficult for x-ray detectors to detect because the bulk of this emission would be attenuated by photoelectric absorption in the intervening ISM.

Though it is possible that these low temperature components exist, we would like to put forth an argument that ignoring the high-temperature blast wave is not justified. Because of the time-dependent nature of the ionization behind the shock, a shell of [Fe XIV] is produced which has sufficient emission volume as to produce a flux comparable to that observed.

The unattenuated [Fe XIV] λ5303 flux observed at the earth, S, from the blast wave of a remnant at a given time is

$$S = \frac{4\pi \int_0^{R_s} n_e{}^2 P_{14}(T_e) A_{Fe} X_{14} r^2 dr}{4\pi D^2} f_{ob}$$

where R_s is the shock radius, n_e is the electron density, P_{14} is the emissivity of the line assuming a solar abundance for the iron (from Allen, 1976) and 100% concentration of the iron in the [Fe XIV] ionic state, A_{Fe} is the abundance of iron in units of solar, X_{14} is the fractional concentration of the [Fe XIV] ionic state, r is a integration variable, D is the distance to the remnant, and f_{ob} is a correction for a beam size less than the size of the remnant. X_{14} and $n_e{}^2$ are the most rapidly changing quantities behind the shock so we approximate the equation for S as

$$S = C_{ev} f_{ob} A_{Fe} P_{14}(T_e) \langle X_{14} \rangle$$

where $\langle X_{14} \rangle$ is the emission weighted average of the X_{14} and is given as

$$\langle X_{14} \rangle = \frac{\int_0^{R_s} n_e^2 X_{14} r^2 dr}{\int_0^{R_s} n_e^2 r^2 dr}$$

The [Fe XIV] λ5303 line results from the forbidden transition $3s^2 3p\ ^2P_{1/2}-^2P_{3/2}$. Population of the $^2P_{3/2}$ level results from direct electron excitation of the ground state or from cascades following electron excitation to higher energy levels. In general, the emissivity, for an atomic line from an element with nuclear charge Z and ionic charge z, in an optically thin plasma of temperature T_e, and resulting from electron collisional excitation is given by

$$\frac{P}{n_e^2} = X_{Z,z} \left(\frac{n_Z}{n_H}\right) 1.71 \times 10^{-19}\ T_6^{-1/2} \Sigma_{eff} \left(\frac{E}{I_H}\right) e^{-\frac{E_{ex}}{kT_e}}\ \text{ergs cm}^{-2}\ \text{s}^{-1}$$

where $X_{Z,z}$ is fractional ionic concentration, (n_Z/n_H) is the number fraction of the element relative to hydrogen, (E/I_H) is the energy of the emitted photon in rydbergs, Σ_{eff} is the effective collision strength, E_{ex} is the excitation energy, and T_6 is the electron temperature in units of 10^6 K. To arrive at P_{14}, the fractional ionic concentration is set to unity, the exponential factor is set to unity because $kT_e \gg E_{ex}$, and the elemental abundance is taken from Allen (1976). A value for Σ_{eff} of ~3 is obtained by extrapolating from a graph given in Nussbaumer and Osterbrock (1970). Σ_{eff} includes cascades following excitation to higher levels. The resulting expression for P_{14} is

$$P_{14} = 3.51 \times 10^{-24} \left(\frac{T_e}{10^6\ \text{K}}\right)^{-1/2} \left(\frac{\Sigma_{eff}}{3}\right)\ \text{ergs s}^{-1}\ \text{cm}^3\ .$$

We will also include λ5303 photons produced following ionizations of Fe XIII to FE XIV. Using branching ratios given by Nussbaumer and Osterbrook (1970), we calculate that 46% of the ionizations will result in λ5303. Taking ionization rates from Raymond and Smith (1977), we can calculate an analogous expression to P_{14} for P_{13}:

$$P_{13}(T_e \gtrsim 10^7 K) = 3.4 \times 10^{-26} \text{ ergs s}^{-1} \text{ cm}^3 \ .$$

We use a nominal value of 5×10^7 for T_e and $1.4 \times 10^{13} \text{cm}^{-5}$ for C_{ev}. For the calculation of $< X_{14} >$ we will assume that at the shock, at least, a low η model as valid. For η = 0.16 and τ = 1.2, $< X_{14} > \tilde{=} 0.18$ and $< X_{13} > \tilde{=} 0.16$. We estimate f_{ob}, which is fraction of emission volume observed, to be 0.07. This calculation of f_{ob} incorporated effects of limb brightening. These values give S equal to $9 \times 10^{-14} A_{Fe}$ ergs cm^{-3} s^{-1}.

This number is less than the measured value by a factor of ~ 13, but three good possibilities that could bring the calculation more into agreement are:

1) The iron abundance of the shocked material could be high by a factor of 2-3 times solar.

2) Lucke *et al.* observed in the region of the most intense x-ray emission. This implies that the post-shock densities might be higher in this region. Higher densities shrink the X_{14} by a factor of n_e^{-1}, but they increase the surface brightness, which is proportional to $C_{ev} f_{ob}$, by n_e^2. The resulting value of S scales like n_e.

3) The Lucke *et al.* measured value for S is dependent on dereddening. They took 2 mag of extinction from the measurements by Westerlund (1967) which assume that the remnant is in the OB Association. If it is closer as the x-ray data suggest, the reddening correction would be lower than the one used.

Given the uncertainties in the input parameters, statistical uncertainties, and uncertainties in the dereddening, this predicted flux might be consistent with the one measured. At the very least, the [Fe XIV] flux from the high temperature blast wave component cannot be dismissed as lightly as Lucke *et al.* suggest if the plasma is not in CIE. For comparison, we note that the value of S assuming CIE in a ~ 5 keV plasma is decreased ~ 20 orders of magnitude from the NIE result.

Conclusion

In summary, the results of this chapter are the following:

1. A significant non-Coulomb, ion-electron interaction is occurring in the remnant, presumably at the shock front.
2. The data can be fit by a model with little or no emission from any source other than the shocked ISM with an age which is consistent with that of MSH 14-63.
3. Anomalous abundances of heavy elements and possible discrepancies in the centroid and shape of the Fe K_α feature could be explained by inhomogenities in the ISM density or by ejecta that have come to thermal equilibrium with the shocked ISM.
4. Under the assumptions of the model, the distance to the MSH 14-63 is inconsistent with distance measured to an OB association in the direction of the remnant; however, plausible deviations in the model assumptions might explain the discrepancy.

Future observations with good combined spectral and spatial resolution, especially at Fe K_α would be helpful in addressing the issues raised here.

Table 1	
Two Temperature Model	
$C_{ev,low}$	$8.1 \pm 1.6 \times 10^{12}$ cm^{-5}
$T_{e,low}$	0.52 ± 0.04 keV
$C_{ev,high}$	$7.1 \pm 0.2 \times 10^{12}$ cm^{-5}
$T_{e,high}$	5.1 ± 0.14 keV
N_H	$1.1 \pm 0.3 \times 10^{21}$ cm^{-2}

Table 2			
NIE Model ($\mathbf{T_e = T_i}$)			
	best fit	~ limits	
C_{sv} (10^{13} cm^{-5})	1.4	1.6	1.2
η (foe$^{1/3}$ cm^{-2})	0.16	0.12	0.22
β ($M_\odot$ foe^{-1})	1 (fixed)	-	-
τ (kiloyears cm^{-1} foe$^{-1/3}$)	1.2	1.3	1.1
N_H (10^{21} cm^{-2})	4.4	4.7	4.1
A_{Si} (solar)	0.7	0.6	0.8
A_S (solar)	3.4	4.1	2.8
A_{Fe} (solar)	3.9	4.8	2.6
χ^2_ν (ν = 53)	1.3	1.4	1.4
α (foe$^{1/3}$ cm)	0.76	0.33	1.7
E_0 (foe)	0.09	0.01	0.6
n_0 (cm^{-3})	0.2	0.4	0.1
t_3 (10^3 years)	0.9	0.4	1.9
D (kpc)	0.7	0.4	1.6

cb. foe ≡ 10^{51} ergs (fifty-one ergs; © Hans Bethe)

Table 3	
NIE Model with K^{α} lines	
	best fit
C_{ev} (10^{13} cm^{-5})	1.2
η (foe$^{1/3}$ cm^{-2})	0.30
β ($M_{\odot}$ foe^{-1})	1 (fixed)
τ (kiloyears cm^{-1} foe$^{-1/3}$)	1.1
N_H (10^{21} cm^{-2})	3.5
χ^2_{ν} (ν = 53)	1.3
α (foe$^{1/3}$ cm)	2.8
E_0 (foe)	2.4
n_0 (cm^{-3})	0.11
t_3 (10^3 years)	3.1
D (kpc)	2.9

Figure Captions

Figure 1

(a) shows a fit to the data using a two-temperature CIE model. Histogram represents best fit model and the crosses are the data points. (b) shows only the high temperature CIE model.

Figure 2

An illustrative example of electron temperature profile when only Coulomb heating is considered is given in (c) from calculations by NIE model. Cox and Anderson (1980) approximate analytic solution is denoted by the broken line. The density and mean temperature profiles are shown for comparison in (a) and (b), respectively. Histograms are calculations from the NIE model and the smooth curves is calculated from the analytic solution for a adiabatic remnant.

Figure 3

The best fit model (histogram) using NIE model is shown with the data points. Insert is the projection of χ^2 space on the $\eta - \tau$ plane. Contours show the change of χ^2 from the best fit. Both 4.6 and 10 are shown.

Figure 4

Same as Figure 3 but now lines have been inserted at the Kα energies of S, Ar, and Fe (2.4, 3.0, and, 6.7 keV, respectively). The abundances of the elements in the NIE model were set to solar.

Figure 5

These graphs represent fits to the data at photon energies $\gtrsim$4.5 keV where the non-iron contributions to the model have been subtracted to emphasize the fit of the model at the Fe Kα feature. (a) shows the best fit when η is fixed at 0.2, (b) is the best fit letting all parameters vary, and (c) is a fit with a CIE model. Fitted abundances, A_{Fe} are given in the figure.

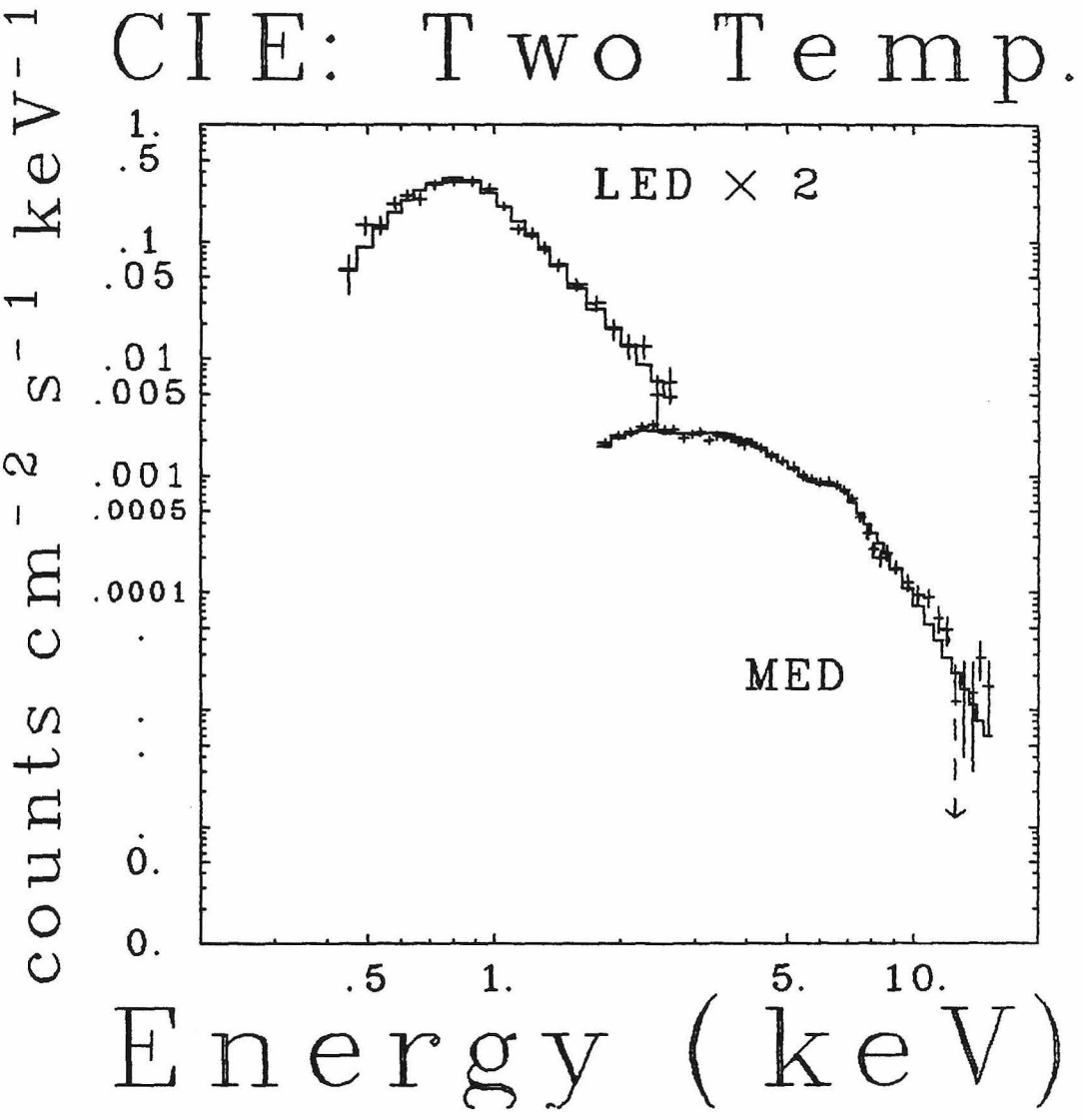
CIE: Two Temp.
LED × 2
MED
counts cm⁻² s⁻¹ keV⁻¹
1.
.5
.1
.05
.01
.005
.001
.0005
.0001
0.
0.
.5
1.
5.
10.
Energy (keV)

Figure 1a

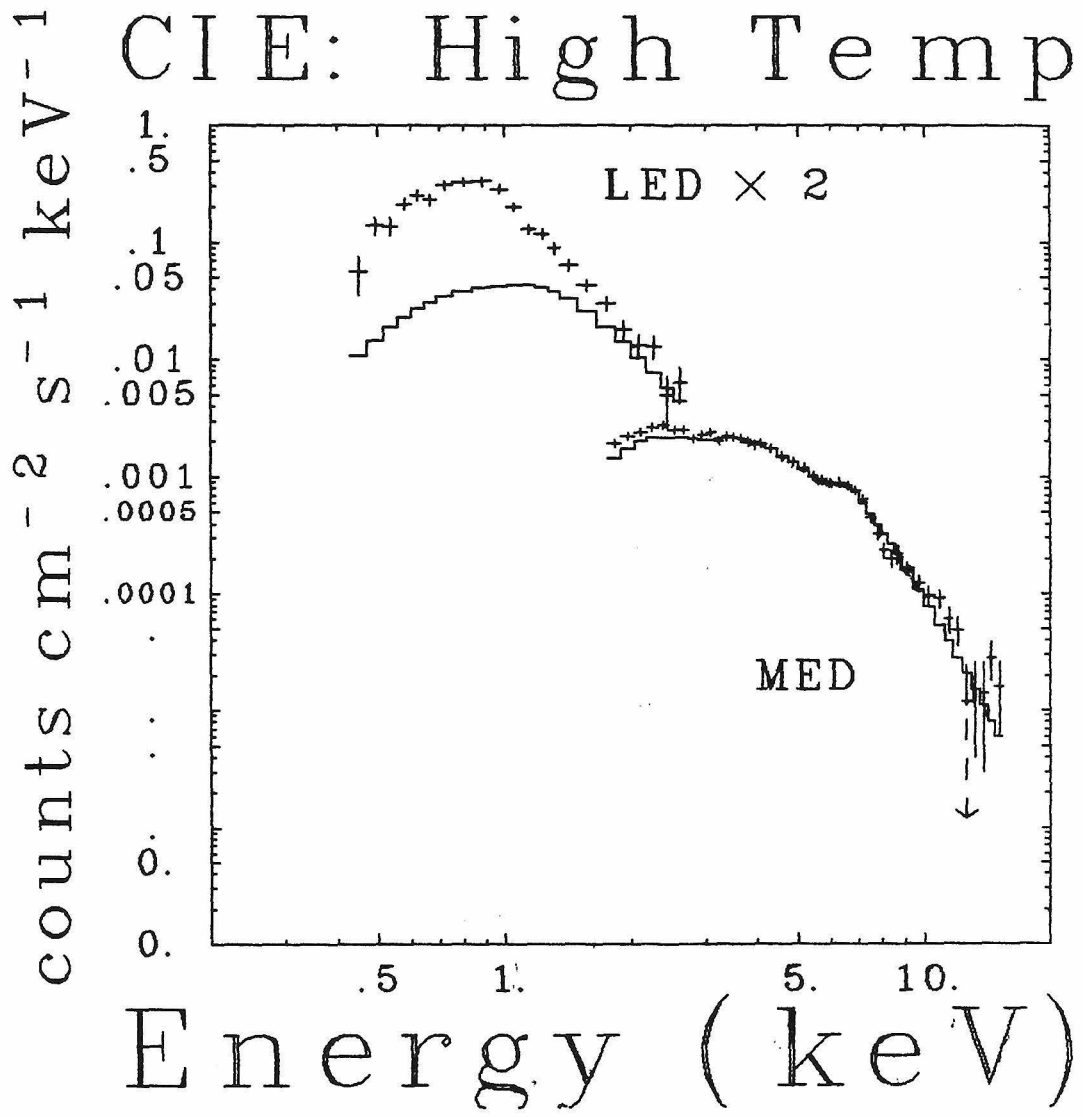
CIE: High Temp
LED × 2
MED
counts cm⁻² s⁻¹ keV⁻¹
1.
.5
.1
.05
.01
.005
.001
.0005
.0001
0.
0.
.5
1.
5.
10.
Energy (keV)

Figure 1b

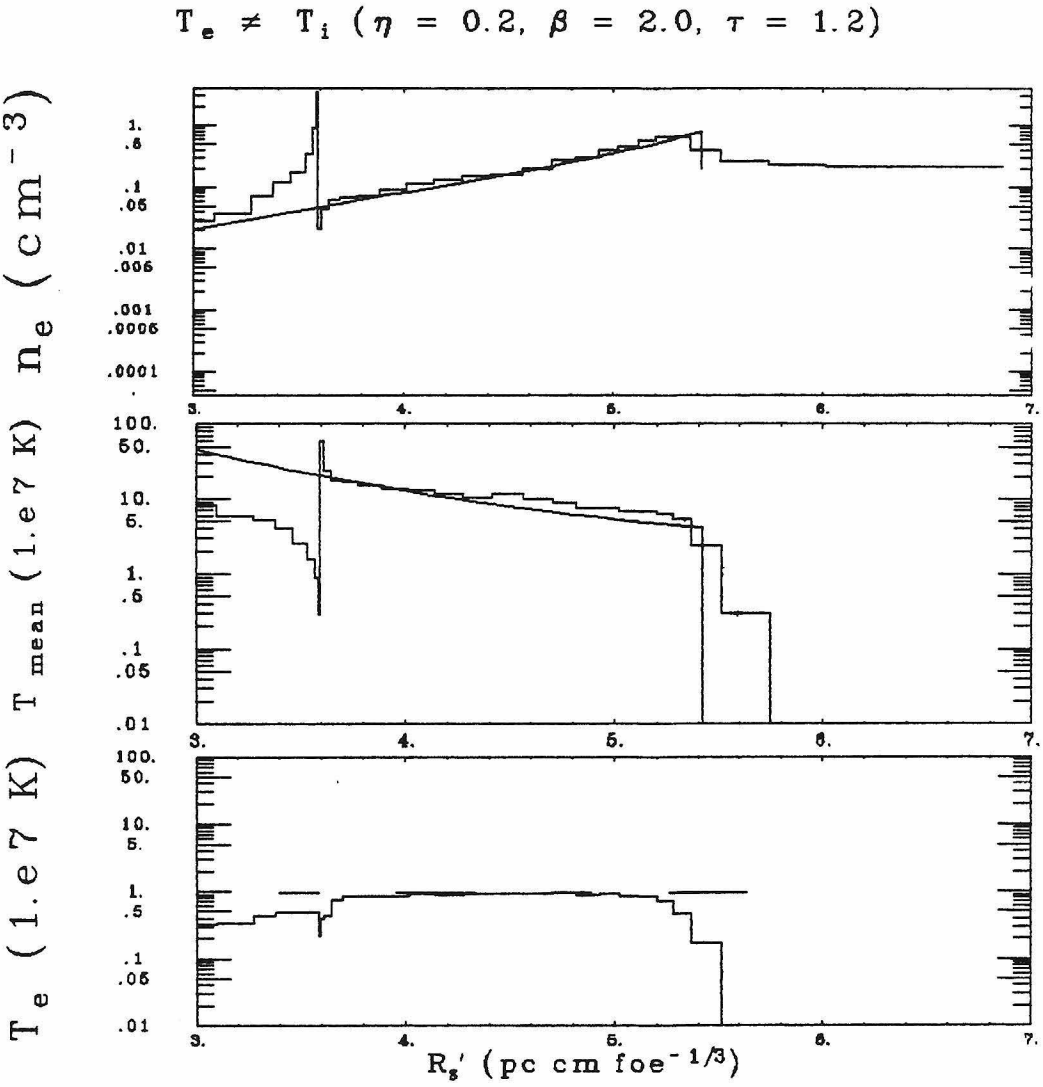
$T_e \neq T_i$ (η = 0.2, β = 2.0, τ = 1.2)
T_e (1.e7 K) T_{mean} (1.e7 K) n_e (cm^{-3})
1.
.5
.1
.05
.01
.006
.001
.0006
.0001
100.
50.
10.
5.
1.
.5
.1
.05
.01
100.
50.
10.
5.
1.
.5
.1
.05
.01
3.
4.
5.
6.
7.
R_s' (pc cm foe$^{-1/3}$)

Figure 2

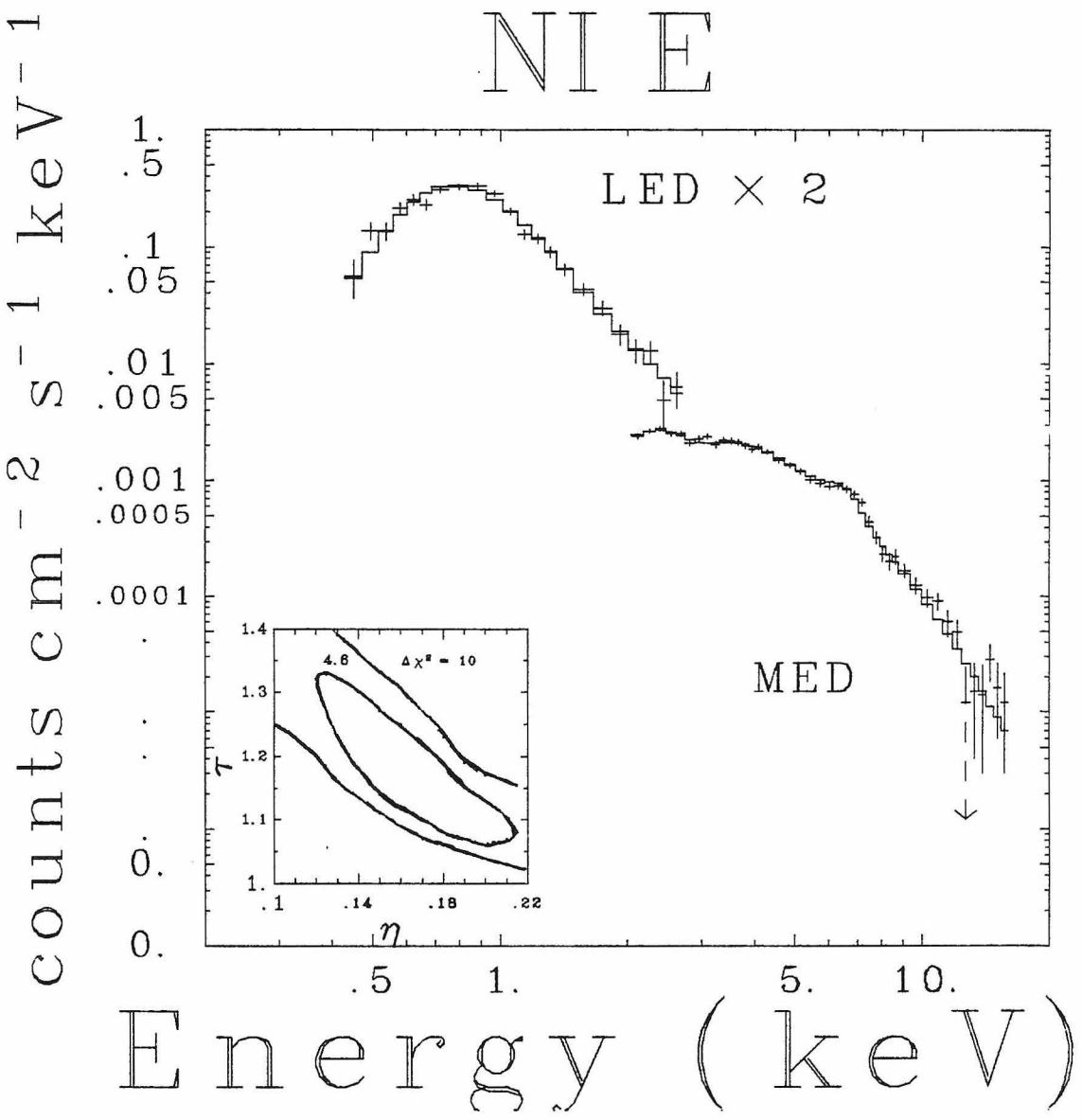
NI E
LED × 2
MED
counts cm⁻² s⁻¹ keV⁻¹
1.
.5
.1
.05
.01
.005
.001
.0005
.0001
0.
0.
.5
1.
5.
10.
Energy (keV)
4.6
Δχ² = 10
τ
η
1.4
1.3
1.2
1.1
1.
.1
.14
.18
.22

Figure 3

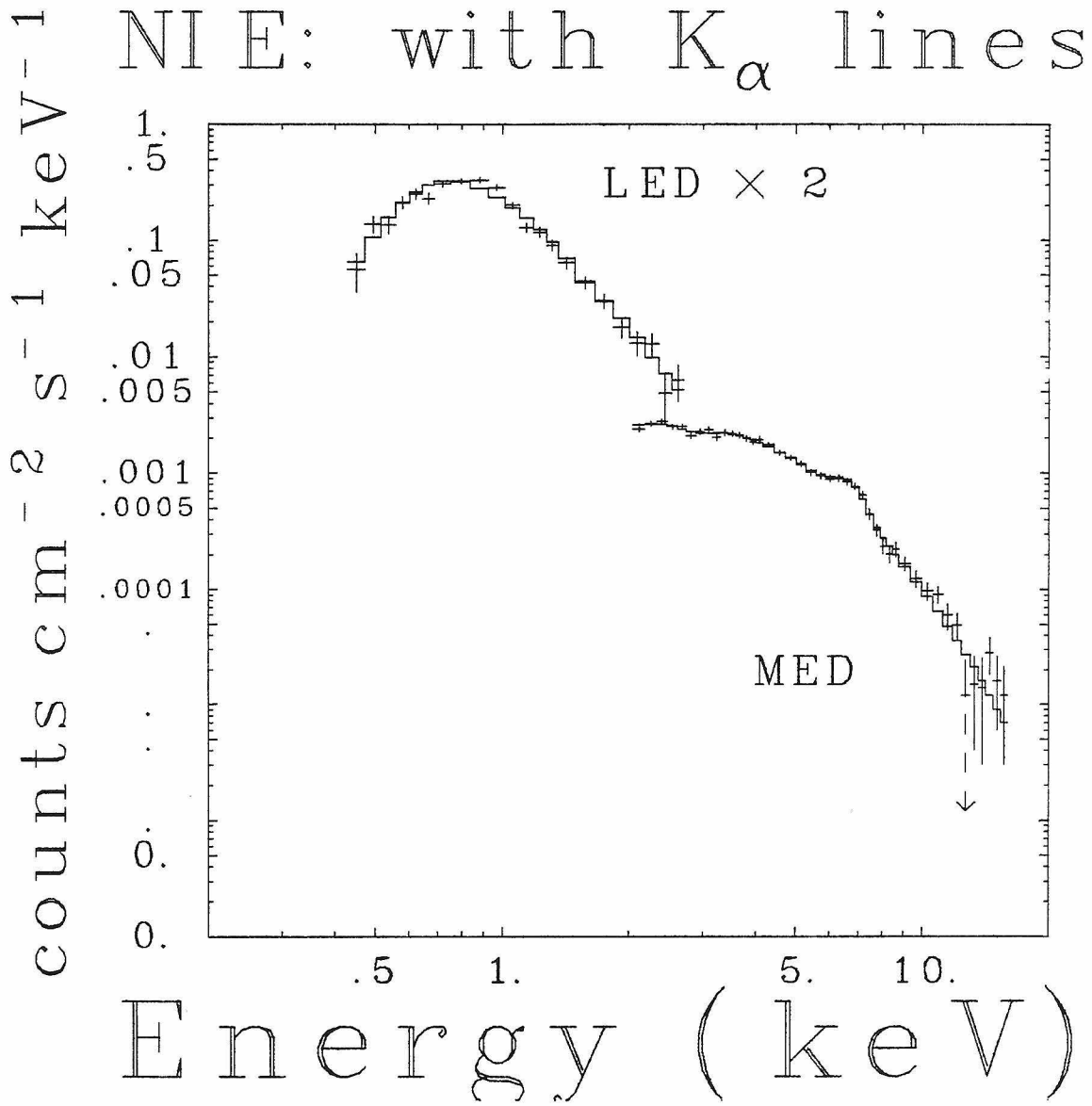
NIE: with K_α lines
LED × 2
MED
counts cm^{-2} s^{-1} keV^{-1}
1.
.5
.1
.05
.01
.005
.001
.0005
.0001
0.
0.
.5
1.
5.
10.
Energy (keV)

Figure 4

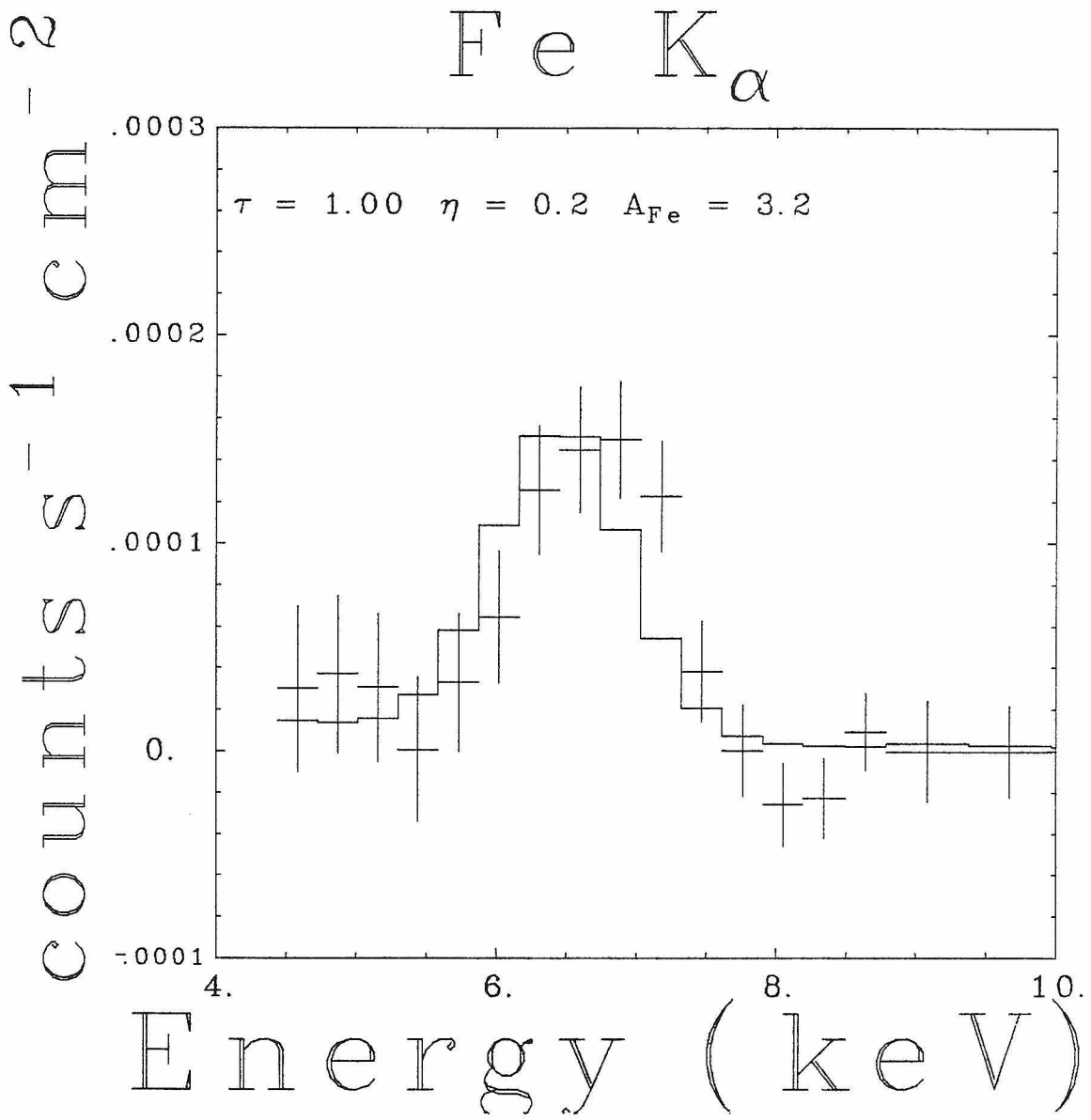
Fe K_α
τ = 1.00 η = 0.2 A_{Fe} = 3.2
.0003
.0002
.0001
0.
-.0001
4.
6.
8.
10.
Energy (keV)
counts - 1 cm - 2

Figure 5a

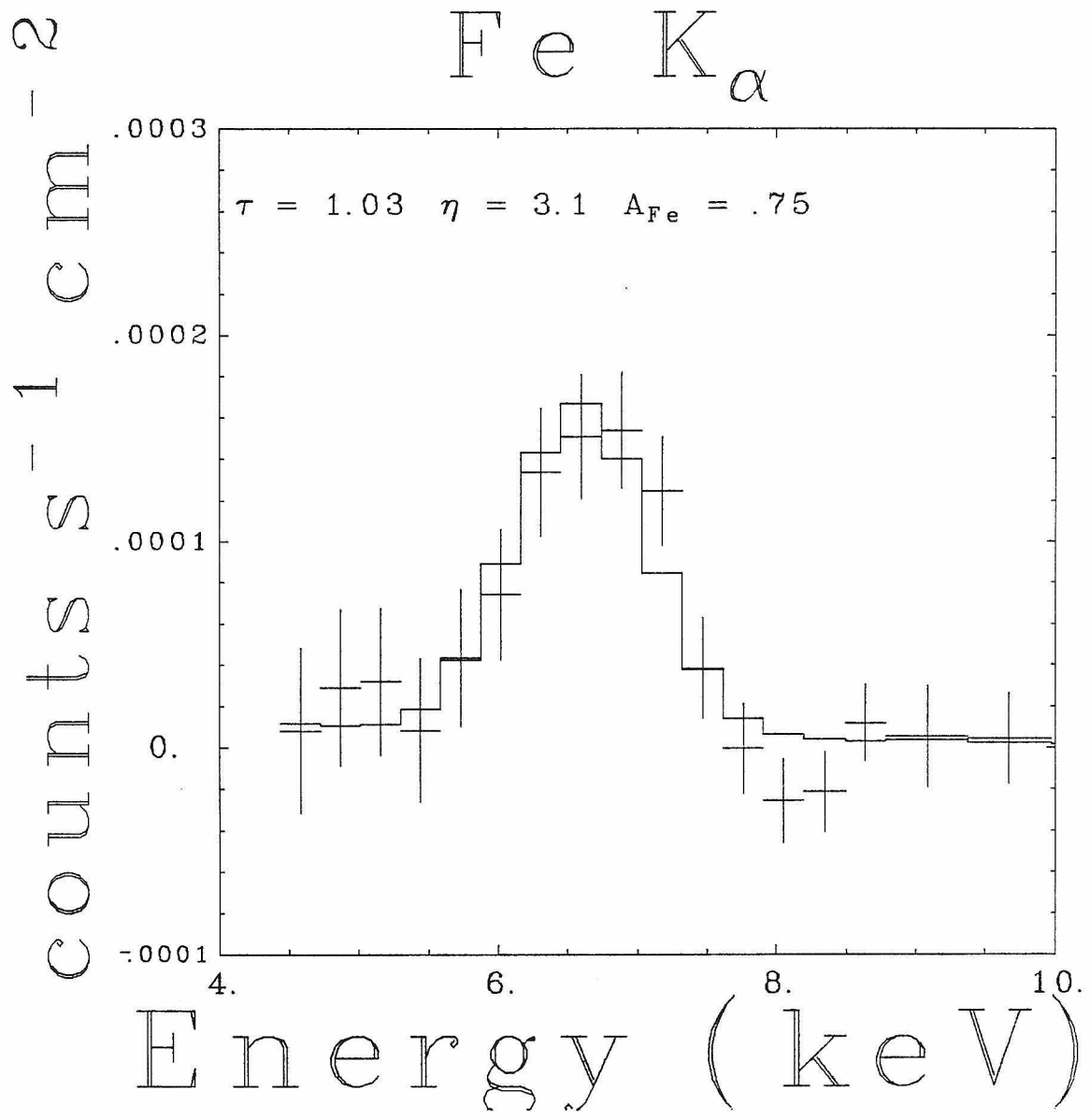
Fe K_α
τ = 1.03 η = 3.1 A_{Fe} = .75
.0003
.0002
.0001
0.
-.0001
4.
6.
8.
10.
counts - 1 cm - 2
Energy (keV)

Figure 5b

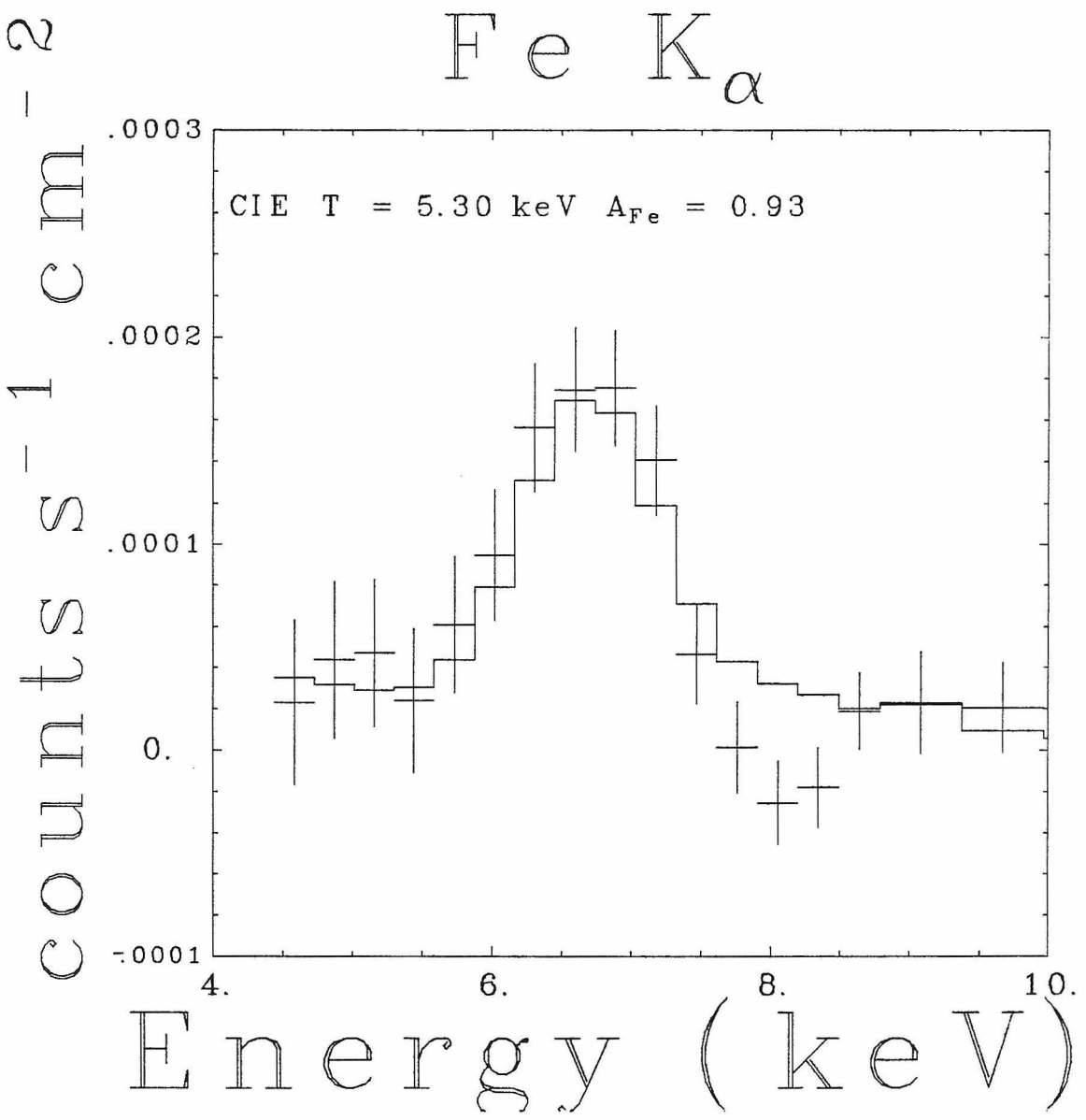
Fe K_α
CIE T = 5.30 keV A_{Fe} = 0.93
counts - 1 cm - 2
.0003
.0002
.0001
0.
-.0001
4.
6.
8.
10.
Energy (keV)

Figure 5c

Chapter 4: Observations of RCW 103

Introduction

The first report of x-ray emission from RCW 103 was made by Tuohy *et al.* (1979) using data from the *HEAO A-2* low energy detectors (LED). The detection was made at photon energies $\lesssim$3 keV. Fits to the pulse height data using a collisional ionization equilibrium (CIE) plasma model allowed temperatures in the range of 1.3 - 20 $\times$ 10^6 K. Results from the *HEAO A-2* medium energy detectors (MED) were ambiguous because of source confusion. An upper limit to the 2 - 10 keV flux was 1 $\times$ 10^{-10} ergs cm^{-2} sec^{-1}. As Tuohy *et al.* point out, this upper limit does not exclude any temperature that is consistent with the low energy spectral data.

X-ray images have been obtained from the *Einstein* Observatory. Data from the High Resolution Imaging (HRI) experiment (Tuohy and Garmire, 1980) and the Imaging Proportional Counter (IPC) experiment (Tuohy, private communication) exhibit a limb brightened shell. The surface brightness around the ring is not uniform - the most intense region is in the southeastern part of the remnant. The angular radius of the x-ray emission is ~9 arcminutes. Radio maps of the region also show a ring-like structure of comparable radius (Goss and Shaver, 1970). Optically, filaments exist in the southeast and northwest parts of the remnant. They are contained within a projected radius which is smaller than the radius of the x-ray/radio emission.

An interesting feature of RCW103 is the presence of a x-ray point source in the geometric center of the remnant (Tuohy and Garmire, 1980). No detectable radio emission has been observed from this point source (Tuohy *et al.*, 1983) suggesting that it may be of a different character from the pulsars that exist at the center of some other supernova remnants (SNR). Tuohy and Garmire suggest that it may be the first detection of thermal radiation from a cooling

neutron star.

A distance to RCW 103 of 3.3 kpc is estimated based on the kinematic models of the neutral hydrogen in the spiral arms and absorption profile of RCW 103's radio continuum at 21 cm (Caswell *et al.*, 1976). This distance estimate along with the measured angular diameter of the x-ray emission would determine the shock radius to be 4.5 pc. This size would indicate that RCW 103 is a young or possibly middle aged SNR. Assuming the kinematics of the shock are described by a Sedov blast wave, the remnant size would imply an age of $\sim 600(n_0/E_{51})^{1/2}$ years, where the particle density of the interstellar medium (ISM), n_0, is in units of 1 cm^{-3}, and the supernova blast energy, E_{51}, is in units of 10^{51} ergs.

Westerlund (1969b) has suggested that the progenitor of RCW 103 might have been a member of an OB association 3.9 kpc away that lies along the line of sight to the remnant. The association with an OB star group would also suggest that the supernova was a Type II event since Type II supernovae are thought to be due to massive, early type stars (eg Shklovsky, 1962).

In the previous chapter we presented an analysis of the *HEAO A-2* data of SNR, MSH 14-63 (RCW 86), using a model developed to account for non-equilibrium effects in SNR (NIE model). In this chapter we use the model to fit the RCW 103 data collected by the Solid State Spectrometer (SSS) experiment on the *Einstein* satellite. Because the SSS has good spectral resolution below ~4 keV ($\Delta E/E \sim 10\%$), line features can be more readily distinguished with the SSS than with proportional counter detectors flown previously. These line features, each associated with a blend of lines from a single element, are seen prominently in the spectra of most young SNR's. In the SSS, $K\alpha$ lines from Mg, Si, and S are the three most striking features. Lines from n=3 to n=2 transitions in Fe also produces a large amount of the flux at around 1 keV. To properly infer

elemental abundances from the intensities of the these features, a proper accounting of the ionic concentrations must be made. Previous work modeling the RCW 103 SSS data have used a CIE plasma model (Becker, private communication). Two plasmas at different temperatures were required to explain the data. In addition, the CIE model required that the abundances, relative to solar, for the elements of Mg, Si, S, and Fe be $\gtrsim 2$. Because the plasma may not be in CIE the calculated ionic concentrations and hence the inferred elemental abundances may be in error. Models which assume non-ionization equilibrium (NIE) in a solar abundance, shock heated, plasma produce a spectrum, that when convolved with a detector response function, can emulate a second, lower temperature component and produce anomalous line strengths relative to a CIE model (Itoh, 1977, 1978, and 1979; Nugent, 1982; Shull, 1982).

The reflection efficiency of the telescope on the *HEAO A-2* observatory drops sharply for photons above ~4 keV. Consequently no high energy data were obtained with the aforementioned imaging observations (IPC/HRI) or during the SSS observations discussed above. This ignorance of the high energy spectrum has serious consequences for the analysis performed here. Because line emission from heavy elements is the dominant emission mechanism in the part of the spectrum where the SSS is sensitive, interpreting the spectral data requires a complex model; however, above ~4 keV the continuum dominates, so measurement of the spectrum at these energies is a less model-dependent measure of the electron temperature and reduced emission volume of the shock heated ISM. Addressing the issue of electron-ion equilibration behind the shock becomes more difficult as result of this lack of data. Measurement of the continuum in this energy range has been definitive in demonstrating that some non-Coulomb electron-ion interactions are present in Cas A (Pravdo and Smith, 1979), Tycho (Pravdo and Smith, 1979), and MSH 14-63 (Nugent *et al.*, 1982).

Despite a growing body of evidence that these non-Coulomb processes exist at the collisionless shock fronts of young supernova remnants, there still does not exist a detailed model of the process, so that we are ignorant of how the magnitude of the effect might vary over a plausible range of SNR shock parameters. It is known, for example, in the collisionless shocks which occur when the solar wind impinges on the magnetosphere of the earth, that the electron temperature is lower than the ion temperature. Even though we have a bias towards models that have electron-ion equilibration, we will search for evidence of this in the SSS data on RCW 103.

Observations

The spectral data were obtained from observations with the Solid State Spectrometer (SSS) experiment on the *HEAO-2* spacecraft. The SSS experiment is described in detail in Joyce *et al.* (1978). Briefly, the experiment has an effective collecting area of 200 cm^2 and a circular field of view with a diameter of 6 arcmin. Spectral data are collected in the photon energy range from $\sim$ 0.5 to $\sim$ 4 keV.

Because the field of view of the spectrometer is smaller than the the angular size the remnant (9 arcmin), a number of different observations are required to obtain the spectrum from the entire remnant. Specifically four observations were performed. Figure 1 is an an x-ray surface brightness map showing the positions and approximate extent of the field of view of the different observations. For each of the observations, Table 1 gives the co-ordinates of the center of the field of view, the epoch, and the integration time. The uncertainties in the positions are $\lesssim$ 1 arcmin (Symkowiak, private communication).

Comparison of Observations

The fields of view of the four observations of the RCW103 remnant do overlap to some extent, but they all sample a different part of the remnant. This gives some limited spatial resolution to the spectra. Before fitting the data we shall statistically test whether the four data sets are consistent with a single, generalized spectral model. By a generalized model, we mean a set of numbers, M_j, where the subscript refers to the j^{th} pulse height channel. Because the surface brightness varies over the remnant and because the amount of the remnant subtended by the field of view during a certain observation varies we will allow the observations to have overall scaling factor, s_i. The subscript in s_i refers to the i^{th} observation.

The χ^2 statistic used can be written as

$$\chi^2 = \sum_{i=1}^{I} \sum_{j=1}^{J} \frac{(s_i M_j - D_{ij})^2}{{\sigma_{ij}}^2}$$

where D_{ij} is the count rate in the j^{th} pulse height channel of the i^{th} observation, σ_{ij} is the 1σ uncertainty in D_{ij}, J is the number of pulse height channels and I is the number of observations.

The analysis is complicated by a number of effects. First, because certain emitting regions were common to two or more observations, the data sets were not completely independent. For simplicity, though, it was assumed that they were. A second problem concerned the thickness of an absorbing layer of ice that accumulates on the window of the SSS detector. The thickness, hence the amount of absorption of the impinging x-rays varied from one observation to another. The correction of the data for this absorption, in principle, is dependent on the choice of model for the input spectrum. Since no spectrum was assumed for this statistical test, an approximate correction was made by

dividing the data for each pulse channel by the absorption factor for photons with energy corresponding to the nominal energy for that channel. A final problem with the data concerns a background component that is known to vary. This problem is most severe in channels which correspond to photon energies $\gtrsim$2.5 keV. We felt that the shape of the background contamination in these channels is different from the nominal one that has been calculated (private communication, Symkowiak). More attention will be given to this issue later in this paper, but for this comparison here, we will ignore the data above 2.5 keV.

The result of the analysis is displayed in Figure 2. The reduced χ^2 for the fit was 1.28 for 117 degrees of freedom. The chance of χ^2_ν being $\gtrsim$1.28 for 117 degrees of freedom if the model were correct is 2.3%. Under the usually criteria of "90% confidence" the model fails the χ^2 test and does suggest the possibility of intrinsic differences of the spectrum arising from different regions in the RCW 103 remnant. The slightly high χ^2 could be also due to the systematic errors outlined above. Therefore, for simplicity, we will adopt the latter assumption for the remainder of this paper. Given that the spectra are very similar, it is questionable whether the exercise of modeling each data set separately would produce any meaningful differences.

As was mentioned in the introduction, x-ray images of RCW 103 reveal that there exist surface brightness differences over the surface of the remnant. Because of uncertainties in the precise position of the SSS fields of view and the lack of any detailed data on the x-ray morphology aside from a plot, we cannot confirm that the flux received in the SSS bandpass is consistent with the measured surface brightness with the IPC or HRI detectors. All three instruments have different bandpasses - the SSS being the smallest, so if the SSS and IPC or HRI measurements of the relative surface brightness were inconsistent that would imply that spectral differences outside of the SSS bandpass were

responsible for the differences in remnant's x-ray morphology. Alternatively, if that SSS flux is consistent with IPC/HRI result, then variations in the emission integral, [$\int n_e{}^2 dl$], would be indicated. Lack of variation in the SSS spectrum implies that the ionization time, $\int n_e\, dt$, is constant at different positions around the remnant which would further imply that there are no density variations and that variations in filling factors may be responsible for surface brightness variations.

In order to aid future workers on the x-ray morphology of RCW 103, we give the relative de-iced flux of the four observations in Table 2. The fluxes are normalized to the flux of observation #1.

Review of Parameters

Before discussing results of the model, we briefly review for the reader the definitions of the parameters used. The input parameters to the model and the units we will always use are the initial blast energy, E_0 (units of 10^{51} ergs), the density of the interstellar medium around the progenitor star, n_0 (units of 1 cm^{-3}), the amount of ejected mass from the progenitor star, M_e (units of $M_\odot$), the age of the remnant, t_3 (units of 1000 years), the abundance, relative to hydrogen, of elements in the ejecta (normalized to the measured solar value), the abundance, relative to hydrogen, of elements in the ISM (normalized to the measured solar value), and the distance to the remnant, D (units of kpc). These parameters are mapped to a more convenient set of parameters for purposes of the doing spectral fitting. There is a scaling parameter defined as

$$\alpha = \left[\frac{E_0}{n_0}\right]^{1/3}$$

and a number of "reduced" parameters:

$$\eta = (E_0 n_0^2)^{1/3} = \alpha^{-2} E_0 = \alpha n_0 ,$$

$$\beta = \frac{M_e}{E_0} = \eta^{-1} \alpha^{-2} M_e ,$$

and

$$\tau = \left(\frac{n_0}{E_0} \right)^{1/3} t_s = \alpha^{-1} t_s .$$

A fourth reduced parameter is the reduced emission volume, C_{ev}, which is defined as

$$C_{ev} \equiv \frac{\int n_e^2 dV}{4 \pi D^2} .$$

η, τ, β, and C_{ev} are derived from fits to the spectral data. α is then determined from the average x-ray surface brightness by

$$\alpha = \frac{\Sigma'(\eta,\beta,\tau)\Theta^2}{C_{ev}} f$$

where Σ' is determined from η, β, and τ and f is the fraction of solid angle of the remnant filled by shocked plasma. The value of f will nominally be assumed to have a value of unity. With α, the input parameters are given by

$$E_0 = \alpha^2 \eta \quad M_e = \alpha^2 \eta \beta \quad t_s = \alpha \tau \quad n_0 = \alpha^{-1} \eta$$

and the distance is given by

$$D = \frac{R_s'(\beta,\tau)\alpha}{\Theta} .$$

where R_s' is a constant determined from the fitted value of β and τ.

When $\tau \gtrsim .16\beta^{5/6}$ the remnant is in a Sedov phase and the shock temperature, T_s, can be given as a function of τ by

$$T_s = 5.2\,\tau^{-6/5} \text{ keV} \quad .$$

Fits to Spectral Models

As was discussed in the section concerning comparison of observations, there are systematic problems with the background data above 3.0 keV. In the case of the RCW 103 data there were problems reconciling the data with the fitting models at photon energies $\gtrsim$2.5 keV. We will first present results, considering fits to the data below 2.5 keV and then discuss the residuals above 2.5 keV.

We will first discuss models similar to those used by Hamilton *et al.* (1982). As discussed above these models use Sedov hydrodynamics and are equivalent to this model only in the "far Sedov" limit ($\tau >> \tau_s$). The models were fit with β fixed at 2 (β must be finite for numerical reasons.) and no ejecta emission was considered. Models where the ejecta were included are discussed below. The results of the fit with the "hot" electron ($T_e = T_m$) model are given in Table 3 and the data with the model are shown in Figure 3b. Likewise, the "cold" electron ($T_e \neq T_i$) model results are given in Table 3 and the data with the model are displayed in Figure 3a. For both of these fits $\tau/\tau_s \gtrsim 12$, thus assuring our desire to be in a "far Sedov" limit. The parameters that were varied were C_{ev}, η, τ, N_H, and the abundances for magnesium ($A_{\rm Mg}$), silicon ($A_{\rm Si}$), sulphur ($A_{\rm S}$), and iron ($A_{\rm Fe}$). The rest of the elemental abundances were fixed at their solar value.

On the assumption that the emission is from a uniform ISM shocked by a Sedov blast wave, we have inferred the input parameters by the method described in the last section. In addition to the filling factor, f, there is a related effect that the SSS field of view is smaller (6 arcminute) than the extent

of RCW 103 (9 arcminute), and, thus the measured C_{ev} given in the tables is an underestimate. Most of the exposure of the data comes from observations 3 and 4 where the remnant filled the entire field of view, so, as an approximation, we corrected C_{ev} before calculating α by the ratio of the solid angle of the remnant to the solid angle of the SSS beam. We took that ratio to be ~2. The value for α and the inferred input parameters are given in Table 3.

The fits to the data are not of high quality. The reduced χ^2 obtained would result $< 0.1\%$ by chance. It is possible that the high χ^2 are in part due to improper modeling of detector output to a given input spectrum including background effects, but, even if all the problems were due to detector modeling as opposed to source modeling, there is no reason to believe that our best fit parameters are close (compared to the statistical uncertainties) to the best fit values given ideal detector modeling. Despite this caveat, we performed on the "hot" electron model a contraction of χ^2 space onto the $\eta-\tau$ plane. Every point on this plane represents the best fit χ^2 if η and τ are fixed at the values given at that point and all others are allowed to vary. The results are shown in the insert of Figure 3b. Two contours are given. The first is for values of χ^2 which exceed the minimum χ^2 by 4.6. This corresponds to 90% confidence region for 2 interesting parameters (Lampton *et al.*, 1976). Another contour at $\Delta\chi^2 = 10$ is given. Two representative points near the extremes of his region are also shown in Table 3. These illustrate rough statistical limits for the various parameters.

We note that the "valley" of χ^2 on the $\eta-\tau$ plane roughly runs along a line of constant effective ionization time, $\eta\tau$. The fits are sensitive to the shape of the Kα lines of the principal elements. Each Kα blend is composed of emission from the hydrogen-like ion, helium-like ion, lithium-like ion, .etc. Each ion emits at slightly different energies that are roughly ordered by the ionic charge. The SSS does not, of course have the capability to resolve these blends of lines, but they

can be inferred from the shape and centroid of the line which, assuming kT_e is much greater than the energy spacing, will be dependent on the relative concentration of the ionic species. These ionic concentrations depend somewhat on the temperature history, but for the temperatures and elements of interest here, the ionic structure is a more sensitive function of $\int n_e\, dt$. This is the reason that χ^2 contours remain close to iso-$\eta\tau$ contours.

We will first discuss the significance of the different parameters individually. Following that, we will make some general comments and summarize the main points.

Contribution from the ejecta

The possibility of an ejecta emission component resulting from a "reverse" shock wave has been discussed by McKee (1974) and Gull (1973,1975). As has been discussed this reverse shock component manifests itself in one-dimensional hydrodynamic codes like the one used in this model, so, in principle, we can use our NIE to search for the evidence of this component in the x-ray spectral data.

When reverse shock emission from the ejecta was included in the model, best χ^2 were obtained when the ejecta did not contribute significantly to the measured flux. Either the ejecta had a small fraction of the emission volume or the ejecta component had a temperature $\lesssim$100 ev - a temperature to which the SSS is insensitive. It is possible, however, to find models that do have a significant ejecta component that are not in gross disagreement with the data. To demonstrate this a search was made in a restricted part of parameter space for which $\tau < 4\tau_s$. β was allowed to vary, along with the parameters mentioned above. Our spatial and spectral resolution were not sufficient to deconvolve the ejecta contribution to line strengths from the ISM contribution. Hence the

abundance parameter for a given element in the ejecta and the abundance parameter for the same element in the ISM are highly correlated in the fitting process. One can be arbitrarily decreased and, to compensate, the other can be increased without significantly changing χ^2. This problem can be avoided by fixing one of the abundance sets. In most modeling runs the contribution of the ejecta turned out to be a smaller fraction of the emission, so the ejecta was chosen to be the fixed set. Solar abundances for the ejecta were used; however, this might be a poor choice, especially if the progenitor was a Type II supernova.

The results of this search for "hot" and "cold" electron models are shown in Table 5 and Figure 4. In the case of the "cold" electron model a local minimum χ^2 in parameter space was found, but for a "hot" electron model τ needed to be constrained in order to satisfy the condition of being $< 4\tau_s$. Both fits give somewhat worse but comparable χ^2 to models where the ejecta was ignored.

Electron heating at shock fronts

The issue of whether electrons are heated by non-Coulomb processes in the shock of RCW 103 is not clearly resolved by the fits to the SSS data. One reason, mentioned before, for this ambiguity is the inability to directly measure the high energy continuum which gives a relatively model-independent measure of the electron temperature. That inability is related to the insensitivity of the SSS to photons with energies $\gtrsim 4$ keV and is a general problem when relying solely on data from the SSS experiment. Assuming the results of the NIE model are roughly correct there is a more fundamental problem, intrinsic to the RCW 103 SNR. RCW 103 is apparently in a part of $\eta-\beta-\tau$ space where the "cold" and "hot" models are beginning to become indistinguishable. The age, t_{eq}, at which the electron temperatures predicted by a "cold" electron model and a "hot" electron model begin to become indistinguishable is given by Cox and Anderson

(1982) as

$$t_{eq} = 3000 E_{51}^{3/14} n_0^{-4/7} \text{ years}$$

where E_{51} is the blast energy in units of 10^{51} ergs and n_0 is the ISM particle density in units of cm^{-3}. The ratio of the age, t, to t_{eq} is independent of α and, in terms of our parameters, is given by

$$\frac{t}{t_{eq}} = \frac{\tau}{3} \eta^{5/14} \quad .$$

For $\eta = 0.5$ and $\tau = 3.6$, $t / t_{eq} = 0.94$. The fact that the best fit points for both models lie roughly in the same region of parameter space is consistent with the fact that the models are beginning to converge in that region. For $t >> t_{eq}$ the differences in the two model spectra become negligible, but at $t \sim t_{eq}$ only the differences in the predicted electron temperature and hence the continuum spectra becomes negligible. The fact that the fits are not completely similar can be explained by the different electron temperature histories of the shock gas. In the "hot" electron model, the electron temperature of a particular gas element has been decreasing monotonically ever since that gas element has been shocked, while during some or all of that time the "cold" electron model predicts that the temperature has been increasing. Since the evolution of the ionization structure is dependent on the evolution of the electron temperature, it is reasonable to expect differences between the two best fit points in parameter space, particularly the elemental abundances.

Elemental abundances

The fitted ISM elemental abundances in the "hot" electron model are consistent with a solar set. This differs from the results using CIE models by Becker (private communication). The abundances required by the CIE models are a

factor of 2-3 (Table 5) higher relative to solar. The abundances determined by the "cold" electron model deviate from solar by up to factor of ~4.

Since a solar abundance set is nominally expected from a interstellar gas, the results of the NIE "hot" electron model are pleasing. The abundance results may be closer to solar than are shown in Table 3. For historical reasons an Allen (1976) abundance set was used. More recent work by Meyer (1979) shows some significant deviations from Allen for some elements. The conversion between to the two abundance sets is complicated by the fact that the continuum flux is dependent on the elemental abundances, particularly C, N, and O; however, as an approximation we will correct each element by its ratio in the two abundance sets. With that correction, the best fit abundances for Mg, Si, and Fe are all within 5% of solar. This makes the Meyer solar value consistent for each of these elements. The only statistically significant deviation is for S which has Meyer abundance of 1.2.

Not all results from applying NIE models to SSS data of young SNR's have demonstrated solar abundances. Work on Tycho's SNR (Shull, 1982), for example, has shown overabundances still are predicted by NIE models. The distinction may result from the dominance of the role played by the ejecta in the x-ray emission, since the ejecta is thought to be metal rich. In addition to the emission from the ejecta following heating from a reverse shock, ejecta may also mix with hot ISM and heat by conduction.

Distance, density, and interstellar absorption

The distance measurement is consistent with the 3.3 kpc estimate made by Caswell (1976). It also is consistent with the distance measured to Westerlund's OB star group, strengthening the argument for association of the progenitor of RCW 103 with that group.

The height of RCW 103 off of the galactic plane is 23 pc assuming a distance of 3.3 kpc. The inferred particle density of ~ 1 cm^{-3} is reasonable for that position.

Finally, assuming a distance of 3.3 kpc, the measure of N_H, would imply a mean density of $\sim$0.4 cm^{-3} in the intervening ISM. Again, this is a reasonable value.

Age

The age of RCW103 has consequences for the issue of the lack of historical record of the supernova which formed RCW 103 and of the cooling of central point source seen by Tuohy and Garmire (1979). We will adopt for this discussion the age, with uncertainties, determined from the "hot" electron model. First, to put this work in perspective, we note that limits can be put on the age of RCW 103 without resorting to the use of the elaborate NIE model. Taking the radius of the remnant to be 4-5 pc and assuming that the average velocity of the ejected material is $\lesssim$ 0.1 c would put a lower limit to the age of $\sim$140 years. From crude spectral modeling of x-ray data a lower limit for the shock temperature can be determined to be $\sim$0.2 keV. That limit on the temperature along with the measurement of the size of the remnant can be used to assert an upper limit to the age of $\sim$ 6000 years.

Due to its apparently young age and close proximity to the sun, RCW 103 could be expected to be a historical supernova. As pointed out by Clark and Stephenson (1976) if RCW 103 is younger than 600 years the initial supernova event could have escaped attention by Chinese astronomers, since the capital of China was at Peking for most of the time after AD1280. Peking is too far north (latitude $\sim$ +40) to able to see RCW 103. Chinese records become more scarce before $\sim$ 200 BC, so, if the age of RCW 103 is $\gtrsim$ 2200 years, the non-detection of

its supernova, could again be explained. At intermediate times, records existed, the capital was farther south, and the effect of the earth's precession made objects in the direction of RCW 103 more visible in northern latitudes. From the NIE model, RCW 103 is most likely of this intermediate age. To emphasize the point that the Chinese were able to monitor objects in the direction of RCW 103, they did record supernovae in AD 185 at $\alpha \approx 15^h$, $\delta \approx -62°$ (1950) and in AD 393 at $\alpha \approx 17^h$, $\delta \approx -40°$ (1950). They should have had an unobstructed view of the RCW 103 supernova, which is at $\alpha \approx 16^h$, $\delta \approx -51°$ (1950), if the event took place at the time determined by the NIE model.

As also pointed out by Clark and Stephenson (1976) even if the RCW 103 supernova took place during a time when Chinese could observe it, the likelihood of detection could still have been reduced if RCW 103 was near conjunction with the sun at the time of the event. We also point out that Cas A, which is thought to be at the same distance as RCW 103, most likely escaped detection as a historical supernova. If anything, Cas A was a more likely candidate for detection since it was probably more recent and definitely at a much more favorable declination for viewing in the northern hemisphere.

A second issue related to the age of RCW 103 is the cooling rate of the point source in the center of the remnant. Under the assumption that the object is a neutron star and that no mechanism exists for renewing the internal energy of the core, then knowing the age of the neutron star could be a test for different suggested cooling mechanisms (Bahcall and Wolf, 1965; Glen and Sutherland, 1980; Normoto and Tsuruta, 1981; Richardson *et al.*, 1982) The NIE model can only be an effective discriminate of cooling mechanisms if the cooling time scale is within this allowed range for the age of RCW 103. This probably is not the case. Neutrino cooling following pion beta-decay is the fastest cooling mechanism with cooling time scales << 1 year. This can be easily ruled out for RCW

103's neutron star. Recent calculations by Richardson *et al.* which do not assume a pion concentrate in the core give cooling curves that are consistent with the age measured here and the effective temperature of 2.2×10^6 K measured by Tuohy and Garmire. In principle, the age and effective temperature could be used within the framework of models - such as Richardson *et al.* - to determine the mass of the neutron star; however, the uncertainties in the measured quantities were too large to allow this.

Blast Energy

The value determined for the blast energy, $\lesssim 6 \times 10^{50}$ ergs, is somewhat low compared to the numbers that are usually associated with supernova blasts ($\sim .4 - 4 \times 10^{51}$ ergs). Some care must be taken before accepting this upper limit, however. Because the inferred value of the blast energy scales like η^5, it would only take an increase of $\sim$ 10% in the in the fitted upper limit of η to account for the discrepancy.

Since Type I supernovae are thought to have lower blast energies ($E_{51} \approx 0.5$) then to Type II ($E_{51} \approx 1$), the low fitted value of E_0 would be weak evidence for the progenitor of RCW 103 being a Type I supernova.

Summary

Our inability to settle the question of electron-ion equilibration at the shock front may be due, as suggested, to intrinsic properties of the RCW 103 remnant; however, this ambiguity and the ambiguity on the question of reverse shocked ejecta are exacerbated by poor knowledge of the spectrum above 2.5 keV. This part of the spectrum is dominated by continuum emission and as a result gives a measure of the electron temperature independent of many of the systematic problems of the NIE model. It also gives a direct measure of the reduced

emission measure of this high temperature component which provides a base-line for interpreting the "excess" of flux at 1-2 keV. As can be seen from the analysis of the RCW 86 data, this information constrains the permitted volume of parameter space severely even without detailed knowledge of the line emission.

Knowledge of this component could, for instance, help to distinguish between "cold" and "hot" electron models. The "hot" model would predict a shock temperature of ~1-2 kev and reduced emission volume of $\sim 1 \times 10^{13} cm^{-5}$ while the "cold" model would have the high temperature be ~0.7 keV and the reduced emission volume be $\sim 3 \times 10^{13}$ cm^{-5}.

An important future observation will be the determination of the behavior of the spectrum at photon energies above 2.5 keV. Source confusion has thwarted efforts to do so with *HEAO-1* and the high energy cutoff of the x-ray mirrors on *HEAO-2* prevented the SSS from operating in that region. AXAF, BBXRT, as well as more modest shuttle and Explorer missions should have the capability to make this measurement.

Despite the poor coverage of the spectrum, the SSS data on RCW 103 does, of course, provide a good opportunity to study the intensity of the line emission and, hence, deduce elemental abundances. On this note we consider the NIE model to have been a success. Assuming the "hot" electron model is correct, the data do support the idea that the x-ray emission is arising from shocked ISM with elemental abundances roughly the same as solar. The "hot" electron model is preferred because the "cold" electron model has been ruled out in other young SNR's.

Finally, we note that there are indications that RCW 103 may have up to four unique or almost unique characteristics relative to other young SNR's. With parenthetical comment, these are:

1) The radio surface brightness is low by factor of 5-10 from other remnants of comparable diameter (This is fairly certain; Clark and Caswell, 1976).

2) A low value of the blast energy E_0 is derived here. (Many assumptions used.)

3) The supernova was not detected. This possibly suggests a low peak optical luminosity for the supernova. (Other plausible reasons exist.) This argues for a Type II supernova which is inconsistent with feature number 2.

4) A central point source exists that is not a radio pulsar. (This is fairly certain.)

How many of these are true anomalies and what possible connection exists between them is an open question.

Data > 2.5 keV

Figure 5 shows all the data displayed with the $T_e = T_m$ model given in Table 3. The model underestimates the data at photon energies $\gtrsim$2.5 keV. We will restrict our discussion to the electron-ion equilibrium model since the "cold electron" model gives similar results in this energy range. The possibility exists that this anomaly is caused by an incorrect measurement of the background. The background of the SSS is known to have two components (Symkowiak, private communication): a "constant" background component that is simply proportional to the integration time of the observation and a "bump" background component that is also nominally proportional to the integration time but also has a scale factor relative to the constant background that can vary from one integration to another. It is customary to allow this scale factor to be a fitting parameter.

Figure 6 shows the residuals at the end of the spectrum for observations 1, 2, 3, and 4, respectively. The model used was the same one used to the fit the composite spectrum. The only variable in the input model between the different

fits was the overall normalization factor which was determined only by the data with photon energies < 2.5 keV. The "bump background" scale factor was also a free parameter. Figure 5b displays the bump background component. The bump background alone cannot account for all the anomalous residuals. As can be seen, the shape of the anomalous residuals is different from the bump background component. In some cases the residuals have a maximum value at ~ 2.7 keV where the bump background is very small compared to its peak value.

The inability of the standard background subtraction procedure to account for the anomalous residuals does not preclude the possibility that the problem is related to background subtraction. Other variations in the intensity and spectrum from the nominal background model are suspected in other SSS observations (Symkowiak, private communication). Most of the background is produced by false counts made by charged particles in the magnetosphere of the earth. Variations in the density and spectrum of these charged particles can explain variations in the SSS background. Indeed, the "bump" background scheme was an empirical attempt to account for these variations but perhaps not comprehensive enough.

Table 6 gives a measure of the residuals in each of the observations. The residuals were averaged between the energy of 2.5 and 3.2 keV. This range was chosen to minimize the dependence of measurement on the amount of "bump" background. Also given, for comparison, is the average flux over the range of 0.8 to 2.5 keV received during the various observations. The residuals from observations 1 and 2 are twice as large as observations 3 and 4. This may be significant since the first two observations form a distinct set, grouped in time, from the last two observations. As can be seen in Table 1, observations 1 and 2 and observations 3 and 4 were close together in time but, the epochs for each pair were relatively far apart (~ 9 days). The observations in the first pair looked at edges

of the remnant and subtended a smaller fraction of the surface brightness than the second pair which was more centrally located on the remnant. The count rates from the first pair were smaller for this reason. The first pair also has shorter integration times. The correlation of the intensity of the residuals with the epoch of the observation and the anti-correlation with the intensity of the known source intensity at other photon energies would support the notion that the residuals were caused by an inaccurate model of the background. Anti-correlation of the residual intensity with integration time might also be indicative of background problems. Examination of other observations taken during this time have not been helpful. The source intensity at the pertinent energies overwhelmed the effect we were looking for in other observations. In any case, the effect might vary with position over the earth as well as the orientation of the telescope relative to the the direction of the magnetic field and both of these parameters may be correlated with the pointing of the telescope in the direction of RCW 103. However, the evidence for background contamination is far from conclusive, and we now examine possible contributions to these residuals that originate at the remnant.

Attempting to explain the residuals in terms of emission from an optically thin plasma is difficult. The data require a rising photon spectrum at photon energies greater than 2.5 keV. Any additional continuum component, then, falls off faster than the data regardless of the temperature. Line emission is a possible explanation, but it has difficulties. Any significant contribution due to the line emission from elements with ($Z \leq 16$) can be ruled out. The strength of the Kα emission features gives upper limits to the amount of power from these elements in the lines above 2.5 keV. For example, one of the most powerful lines of this type is a result of an n = 3 to n = 1 transition in S XV (line energy at 2.88 keV). Even under the most optimistic condition the power in the S Kα feature

would constrain the power in the 2.88 keV line to be factor of ~ 7 below that required to explain the data at that energy. An overabundance of chlorine of a few hundred relative to solar could explain the data but is unlikely.

Before considering other spectral forms, a relevant factor is the central point source of the remnant. Enough systematic uncertainty exists that it cannot be said for sure whether or not the point source was within the field of view of the detector during each observation. It was certainly within the field of view during observation number 4 and most likely within the field during observation number 3. Given the nominal positions, the point source was not involved in observations number 1 and 2. Including possible offsets of the collimator (Symkowiak, private communication), it might be in one of those fields of view, but not both of them. It is not possible, then, for the point source to explain all the residuals. It is possible that the residuals in observations 1 and 2 are not caused by the same phenomenon as in latter observations, so we cannot rule out the role of the point source in this matter.

A black body spectrum required a temperature of ~5 keV and an emitting region with a characteristic size of ~100 m at a distance of 4 kpc. Taking a neutron star density as an upper limit to the density of the emitting region, we calculate that the cooling time for this proposed black body would $\lesssim$ 100 days. Thus the emitting region would would need to be ~0.01 the size of a neutron star and would need to be re-energized.

Conclusions

The main conclusions of this chapter are:

1) No variation can be detected in the spectrum collected from different regions of the remnant.

2) The data cannot be used to discriminate between whether non-Coulomb electron-ion energy exchange processes may be present at the shock front.

3) Assuming that non-Coulomb processes are present - a likely hypothesis given results from other young SNR's, the data are consistent with the idea that the emission is all from the shocked interstellar medium with approximately solar composition of heavy elements.

Table 1

RCW 103 Observation Record

Obs #	<Obs. time> (Day of 1977)	Int. time (s)	Position R.A. (1950)	Dec. (1950)
1	425.611	1679.4	243.500	-50.967
2	425.378	1638.4	243.343	-50.899
3	434.122	3604.5	243.425	-50.933
4	434.663	4341.8	243.458	-50.883

Table 2

Relative de-iced fluxes

Obs #	Relative Flux
1	1
2	0.858 ± 0.035
3	1.424 ± 0.045
4	1.351 ± 0.044

Table 3

NIE Model without ejecta

	$T_e \neq T_i$	$T_e = T_i$		
	best fit	best fit	~ limits	
C_{sv} (10^{13} cm^{-5})	1.8	0.56	0.66	0.35
η (foe$^{1/3}$ cm^{-2})	0.5	0.34	0.30	0.49
β ($M_\odot$ foe^{-1})	-	-	-	-
τ (kiloyears cm^{-1} foe$^{-1/3}$)	3.6	4.2	4.8	3.0
N_H (10^{21} cm^{-2})	5.0	3.7	4.1	3.2
A_{Mg} (solar)	0.83	1.5	1.4	2.1
A_{Si} (solar)	0.79	1.0	1.0	1.2
A_S (solar)	1.9	1.3	1.6	1.3
A_{Fe} (solar)	0.20	0.75	0.71	1.3
χ^2_ν (ν = 31)	2.3	1.9	2.1	2.1
α (foe$^{1/3}$ cm)	0.23	0.37	0.26	01.1
E_0 (foe)	0.03	0.05	0.02	0.6
n_0 (cm^{-3})	2.1	0.92	1.2	0.45
t_3 (10^3 years)	0.85	1.6	1.2	3.2
D (kpc)	1.6	2.6	1.9	6.7

cb. foe $\equiv 10^{51}$ ergs (fifty-one ergs; © Hans Bethe)

Table 4

Two Temperature CIE Model

$C_{ev,low}$	1.1×10^{13} cm^{-5}
$T_{e,low}$	0.51 keV
$C_{ev,high}$	8.4×10^{11} cm^{-5}
$T_{e,high}$	$\gtrsim$6 keV
N_H	5.9×10^{21} cm^{-2}
A_{Mg}	2.3 solar
A_{Si}	1.9 solar
A_S	3.2 solar
A_{Fe}	2.9 solar

Table 5

NIE Model with ejecta

	$T_e \neq T_i$	$T_e = T_i$
C_{ev} (10^{13} cm^{-5})	2.0	0.31
η (foe$^{1/3}$ cm^{-2})	0.64	0.55
β ($M_\odot$ foe^{-1})	4.9	3.0
τ (kiloyear cm^{-1} foe$^{-1/3}$)	1.6	> 1.6
N_H (cm^{-2})	4.7	0.29
A_{Mg} (solar)	1.1	3.1
A_{Si} (solar)	0.83	1.4
A_S (solar)	1.2	1.2
A_{Fe} (solar)	0.2	2.4
χ^2_ν (ν = 30)	2.7	2.6
α (foe$^{1/3}$ cm)	0.45	> 1.7
E_0 (foe)	0.13	> 1.6
M_e ($M_\odot$)	0.6	> 4.8
n_0 (cm^{-3})	1.4	< 0.32
t_3 (10^3 years)	0.72	> 2.7
D (kpc)	2.4	> 9.2

Table 6

Obs #	Residual flux (2.5 - 3.2 keV)	Total flux (0.8 - 2.5 keV)
1	4.5 ± 0.9	26.5 ± 0.9
2	4.7 ± 0.9	28.6 ± 1.0
3	2.1 ± 0.6	49.3 ± 0.8
4	2.3 ± 0.5	38.1 ± 0.7
	10^{-2} cnts (SSS area)$^{-1}$ s^{-1} keV^{-1}	

Figure Captions

Figure 1

The x-ray surface brightness map (Touhy, private communication) from the Imaging Proportional Counter (IPC) experiment on the *HEAO A-2* spacecraft. Circles represent the four fields view of the SSS observations.

Figure 2

The results of attempting to find a generalized model that was consistent with the four different observations are displayed. Histogram represents model.

Figure 3

Results are shown of best fits to the data when no ejecta was included (far Sedov limit). (a) is for Coulomb heating model and (b) assumes electron-ion thermal equilibrium. Insert in (b) is the projection of χ^2 space on the $\eta - \tau$ plane. Contours show the change of χ^2 from the best fit. Both 4.6 and 10 are shown.

Figure 4

Results are shown of best fits to the data when ejecta was included. (a) is for Coulomb heating model and (b) assumes electron-ion thermal equilibrium.

Figure 5

Figure 5 shows the same fit as was in Figure 3b but, now, all the data is shown. (b) displays the residuals of the fit and (c) gives the bump fraction function for comparison.

Figure 6

The residuals from each observations to the model in Figure 3b are shown.

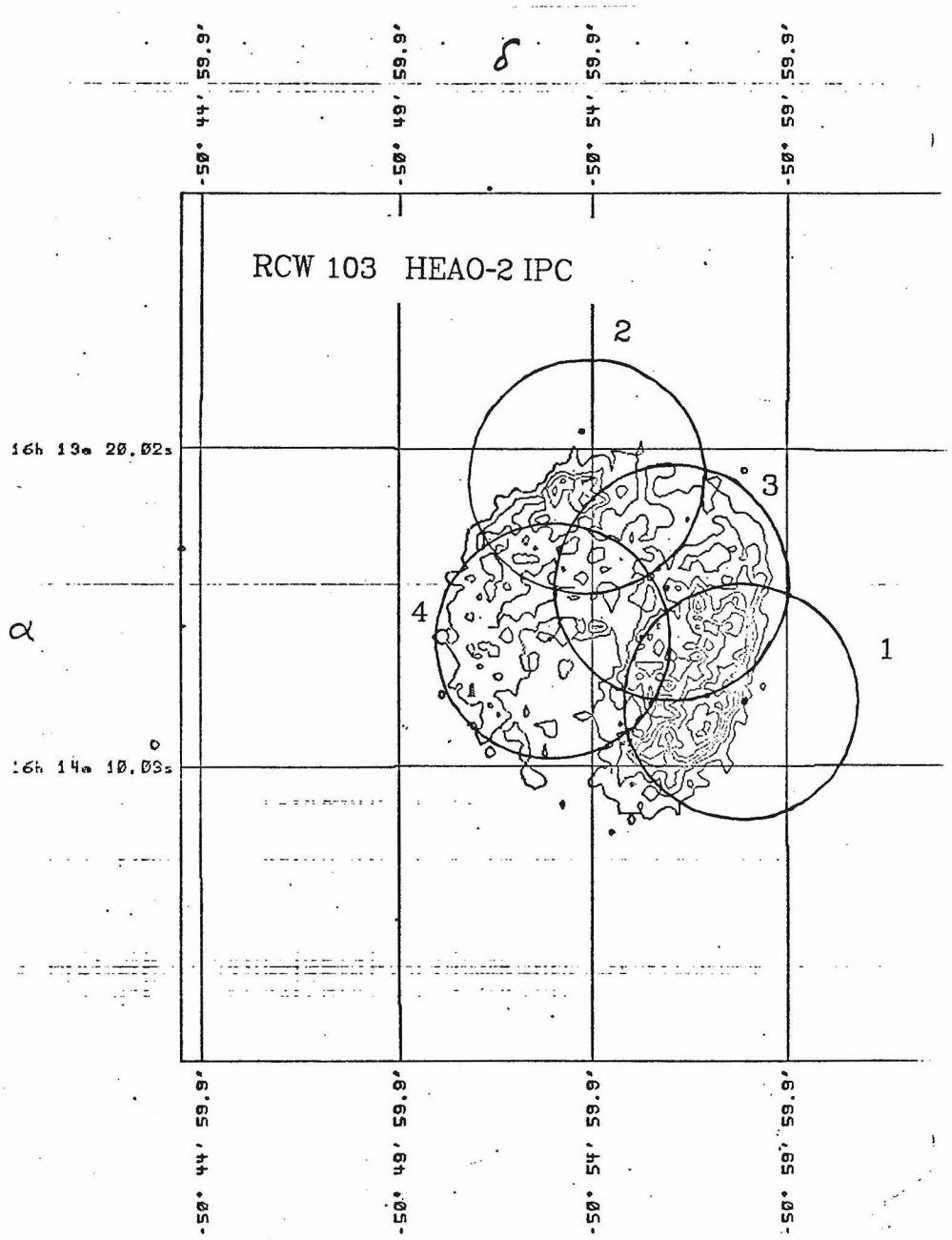
RCW 103 HEAO-2 IPC
δ
α
-50° 44' 59.9"
-50° 49' 59.9"
-50° 54' 59.9"
-50° 59' 59.9"
16h 13m 20.02s
16h 14m 10.03s
1
2
3
4

Figure 1

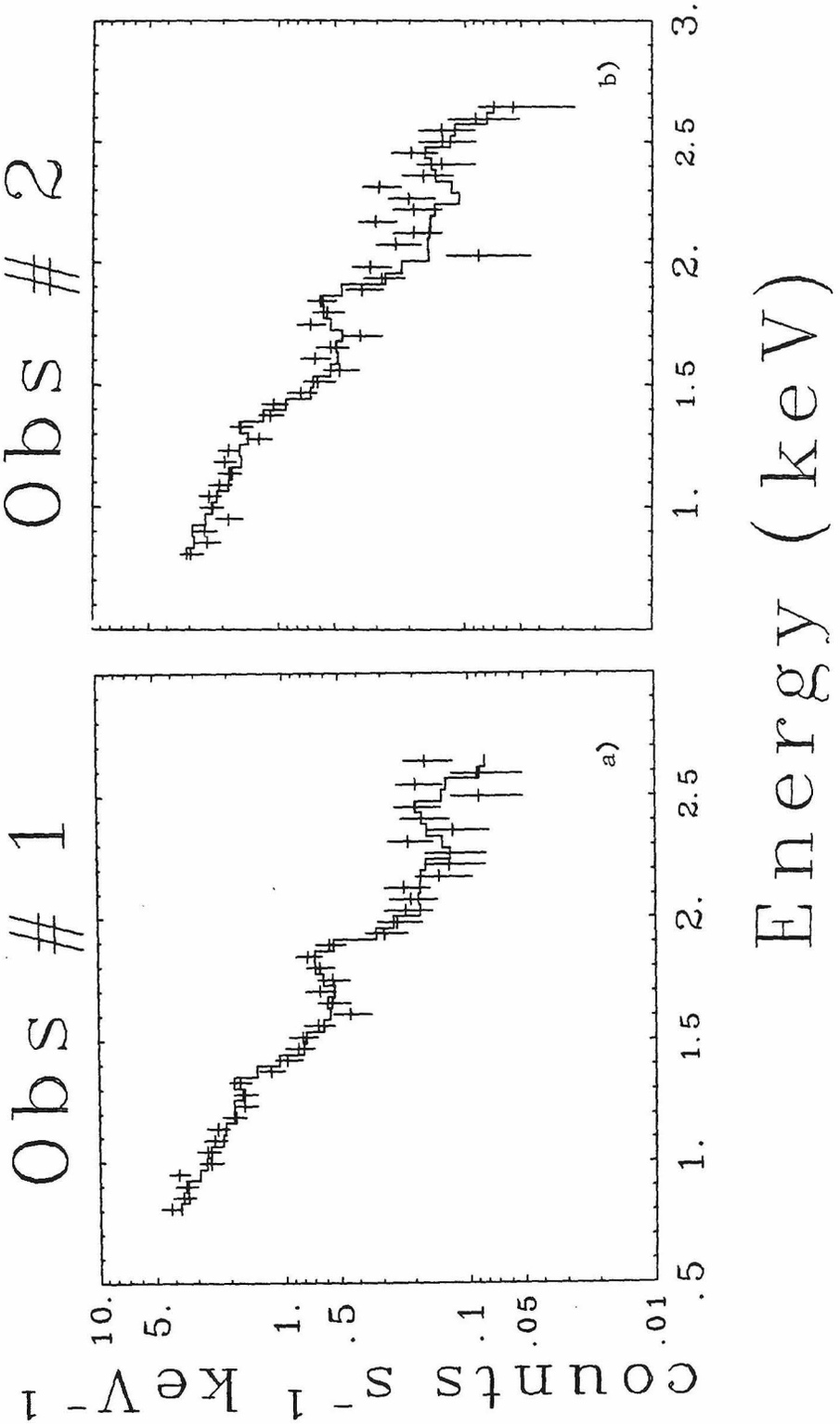

Figure 2

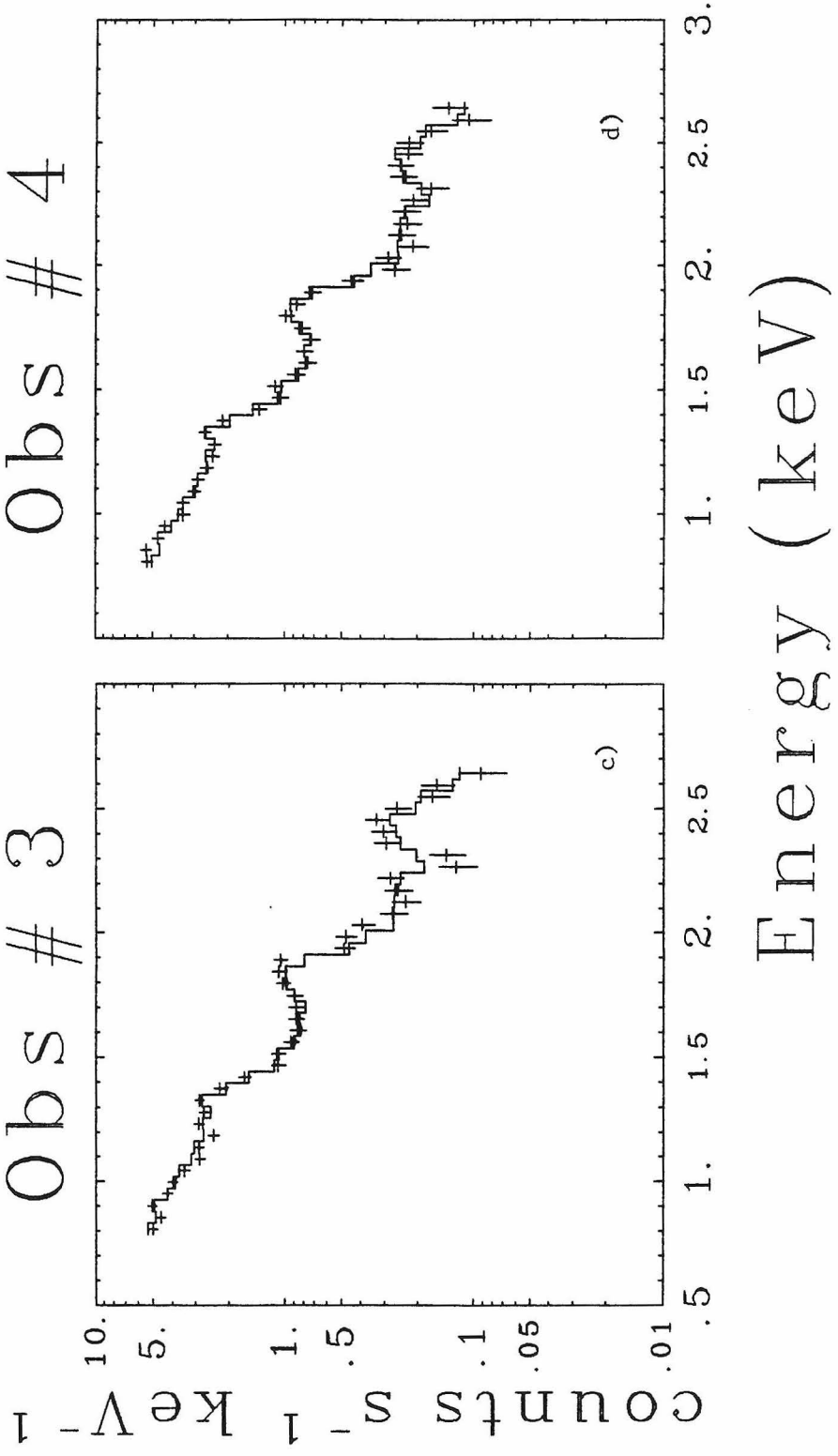

Figure 2

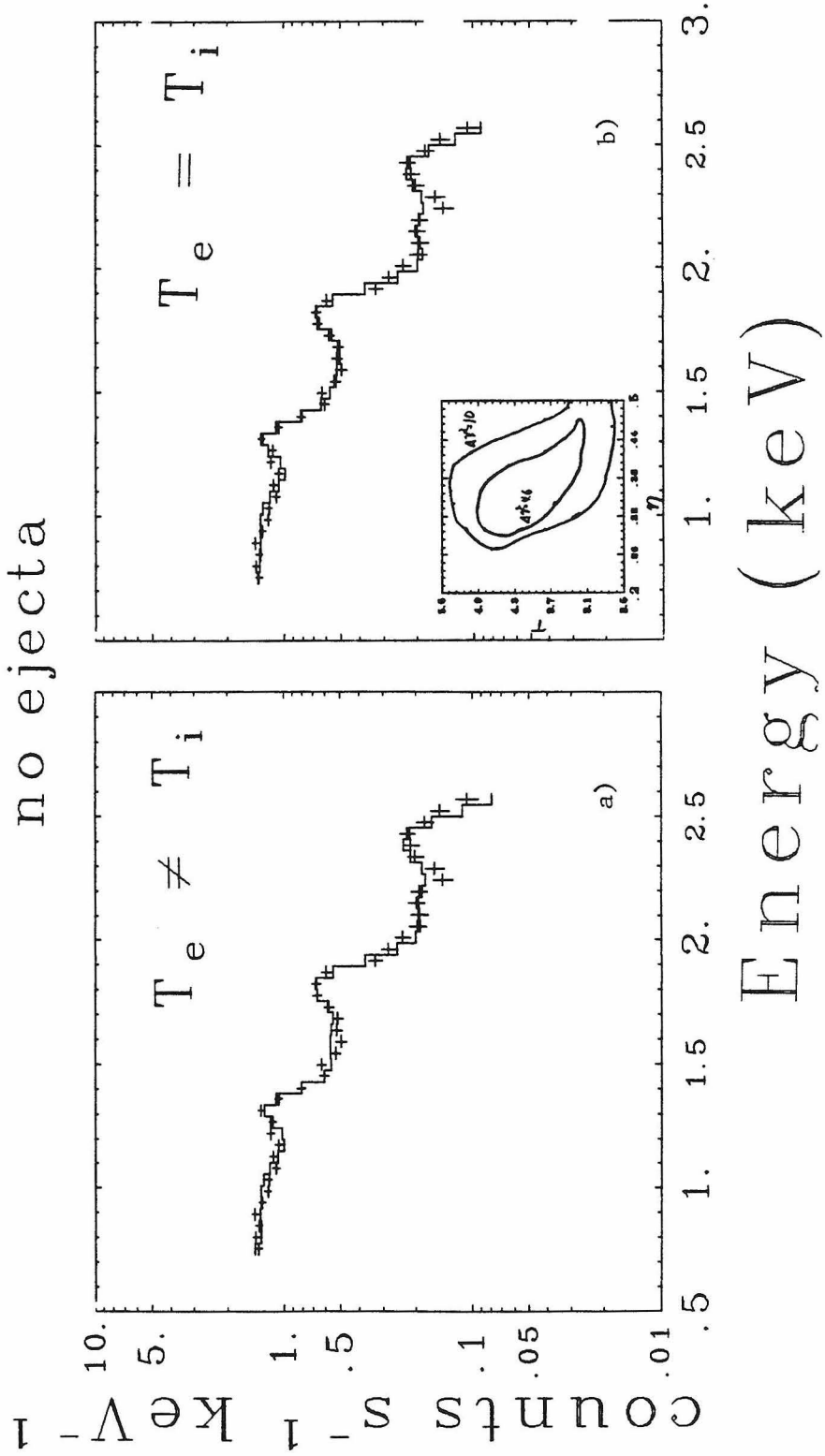
no ejecta
counts s⁻¹ keV⁻¹
10.
5.
1.
.5
.1
.05
.01
.5
1.
1.5
2.
2.5
3.
Energy (keV)
$T_e \neq T_i$
a)
$T_e = T_i$
b)

Figure 3

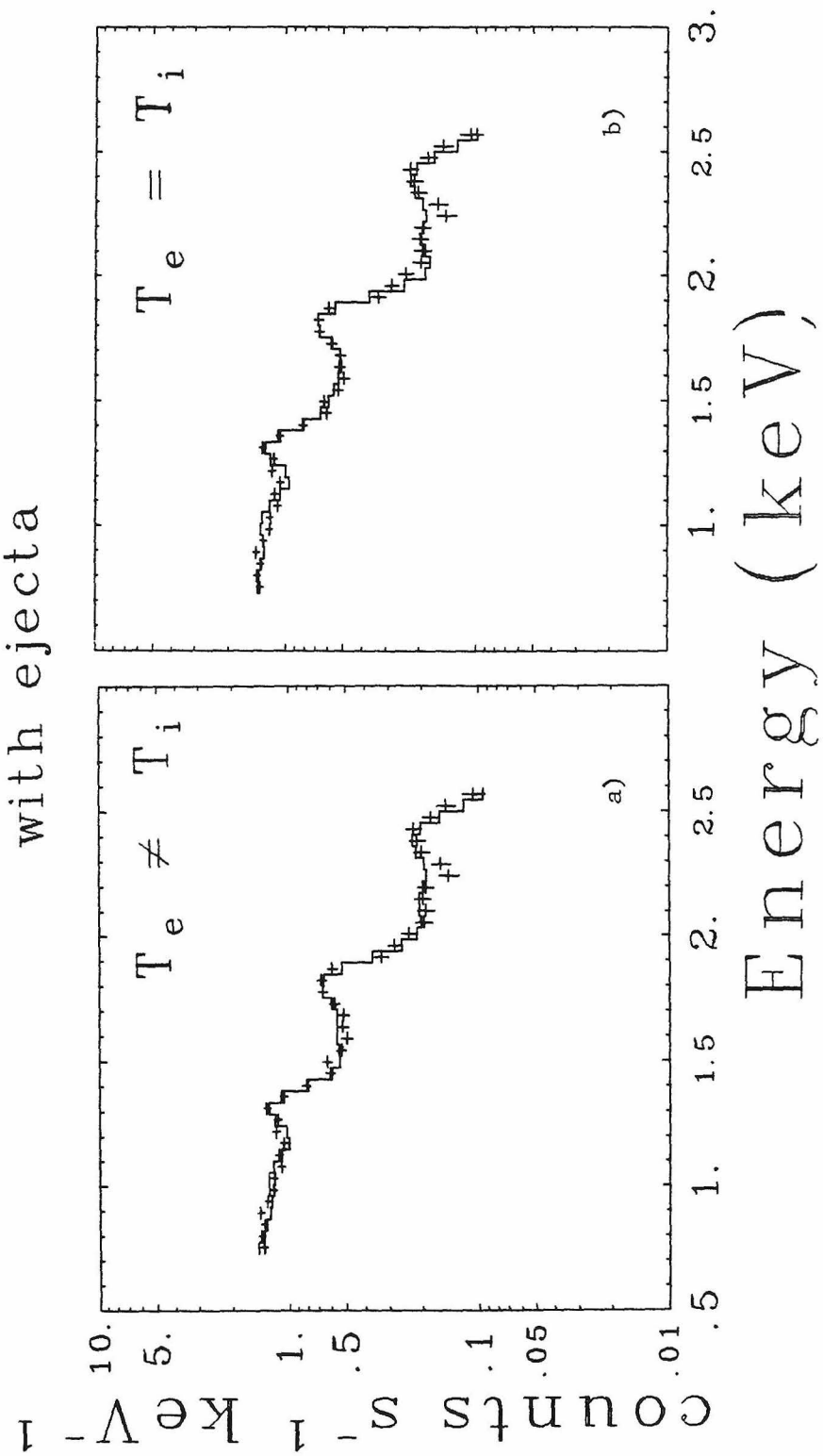
with ejecta
counts s⁻¹ keV⁻¹
10.
5.
1.
.5
.1
.05
.01
.5
1.
1.5
2.
2.5
3.
Energy (keV)
$T_e \neq T_i$
a)
$T_e = T_i$
b)

Figure 4

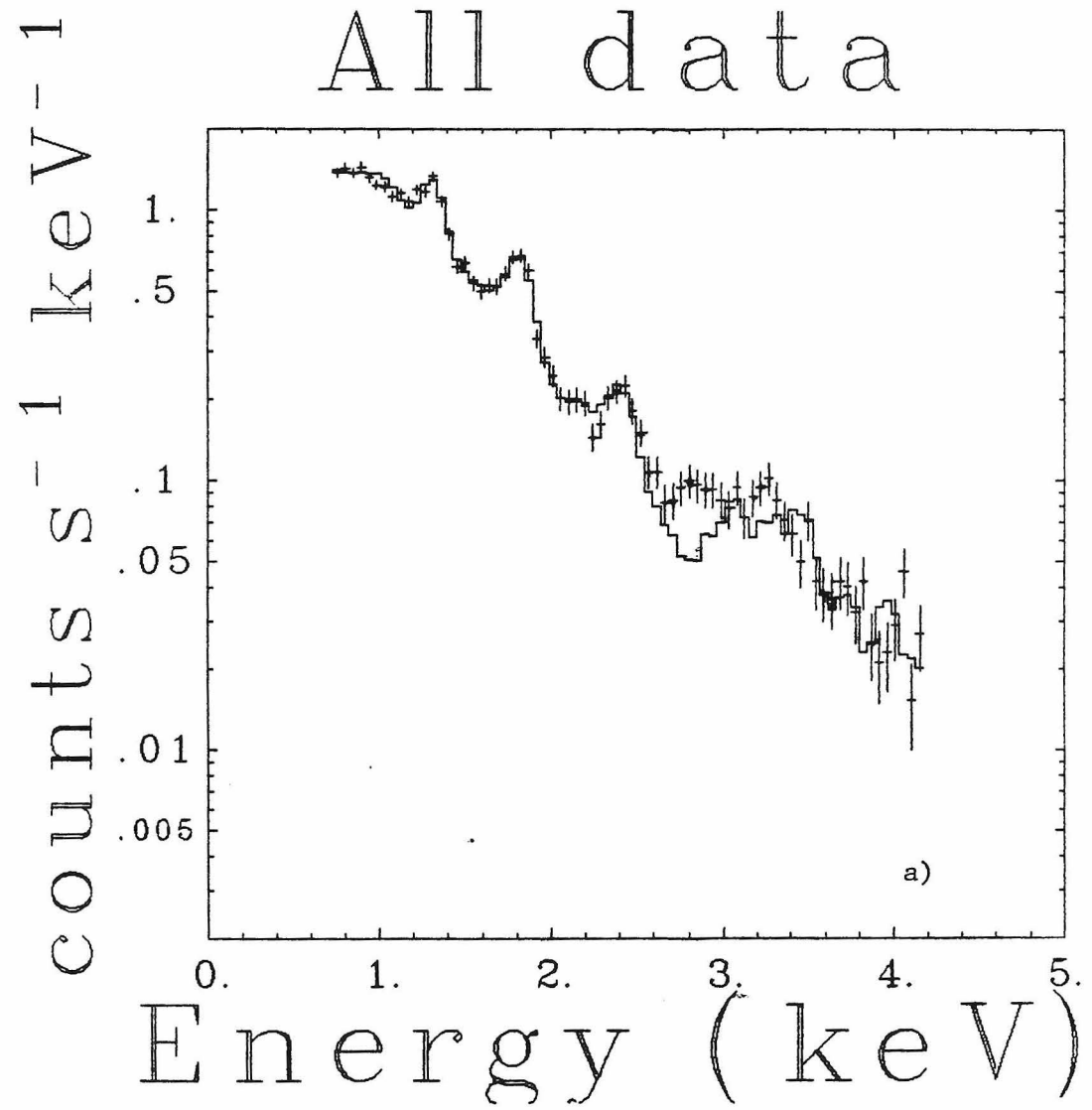

Figure 5

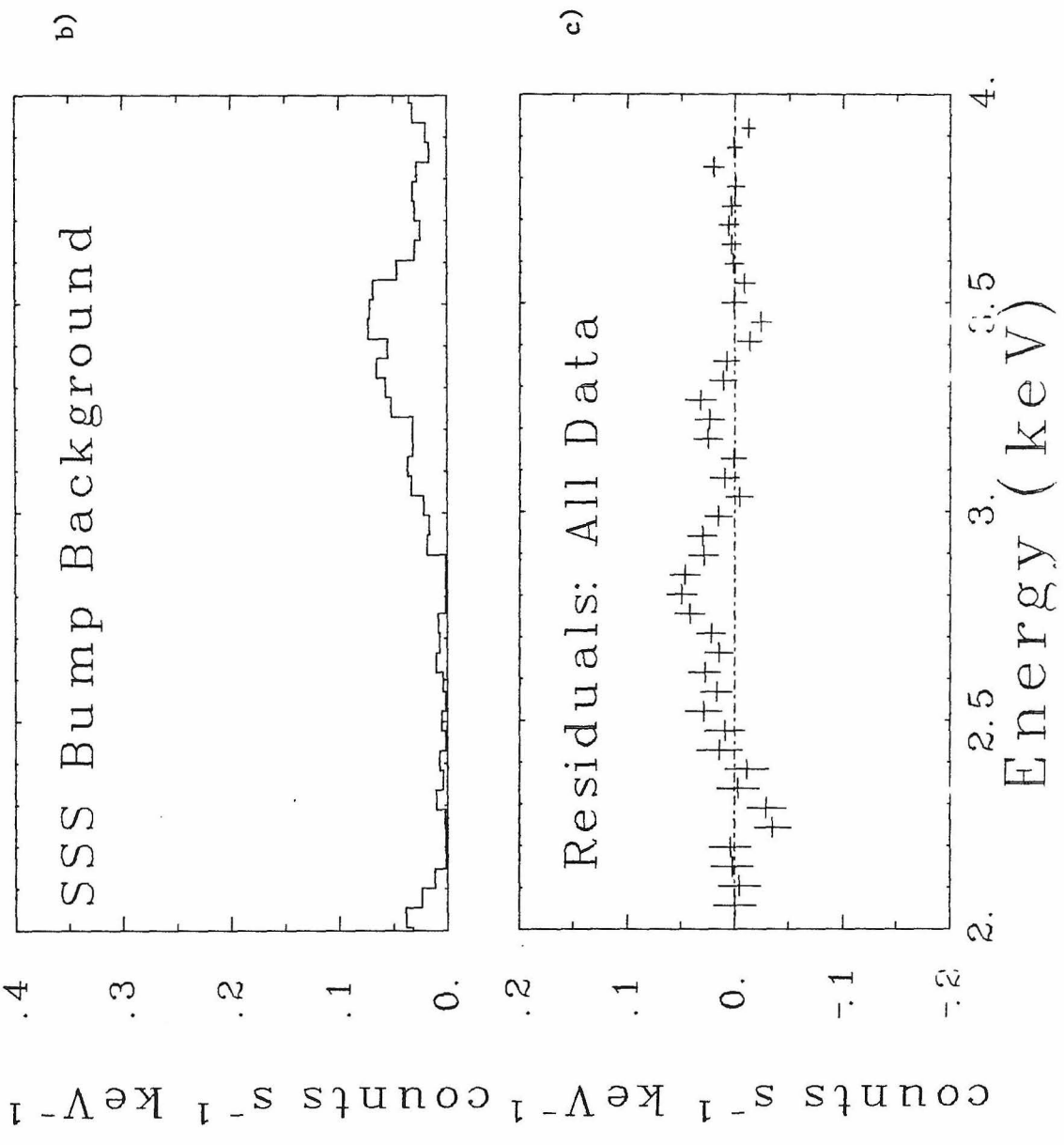
b)
SSS Bump Background
c)
Residuals: All Data
counts s⁻¹ keV⁻¹
Energy (keV)
.4
.3
.2
.1
0.
.2
.1
0.
-.1
-.2
2.
2.5
3.
3.5
4.

Figure 5

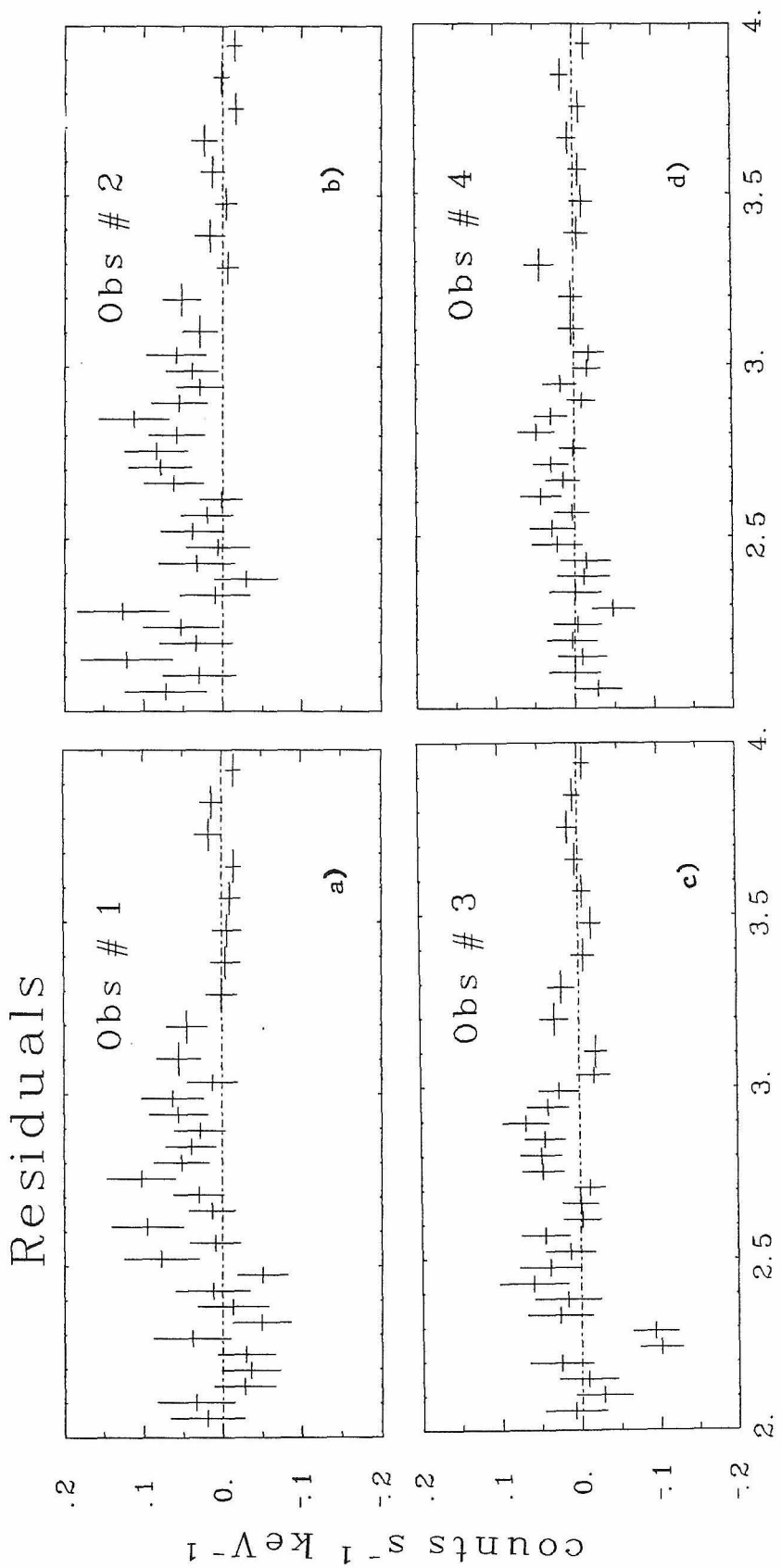
Residuals
counts s⁻¹ keV⁻¹
Energy (keV)
Obs # 1
a)
Obs # 2
b)
Obs # 3
c)
Obs # 4
d)
.2
.1
0.
-.1
-.2
2.
2.5
3.
3.5
4.

Figure 6

Chapter 5 : Concluding Remarks

The NIE models seemed successful from the point of view of the "global" issues since the models did give adequate fits to the data with physically reasonable parameters. The χ^2 were somewhat high, but this is reasonable given systematic uncertainties in the modeling of the detectors, known uncertainties in the atomic physics, and deviations at the source from the ideal conditions assumed in the model. Although the existence of these systematic uncertainties gives reason for some caution in accepting inferred remnant parameters, the physically reasonable results do indicate that these models do hold some promise for use in future observations.

CIE model fits to MSH 14-63 data had required two plasmas at different temperatures. The NIE model showed that with the exception of the S and Fe K_α lines, the data could be accounted for by shocked ISM of solar composition. The offending lines only required abundance changes by a factor of ~ 3, but as was discussed they could be explained by the density inhomogenities that do seem to be present in MSH 14-63 or by ejecta.

In the case of the SSS data for RCW 103, CIE modeling again required two temperature components in order to give adequate fits. Abundance anomalies of $\gtrsim 2$ were required for Mg, Si, S, and Fe to explain the intensity of the line emission. The NIE once more proved successful in providing good fits to the data assuming emission from shocked ISM of near solar composition.

The question of emission from reverse-shocked ejecta was not clearly answered by the work here. For these data sets, β was not a well determined parameter. When β was low, the ejecta was too small an emission component. With increasing β the emission started to become significant but the temperature was so low that the bulk of the flux from the ejecta component was either below the bandpass of the detector or was attenuated by interstellar absorption.

On the issue of electron-ion thermal equilibrium the data from MSH 14-63 resoundingly asserted that some non-Coulomb energy exchange mechanism must exist behind the blast wave. MSH 14-63 joins Cas A and Tycho as young remnants where evidence for a non-Coulomb mechanism have been found. The case of RCW 103 is uncertain. Lack of information in the spectrum above 4 keV makes the interpretation difficult.

Future observations providing simultaneously good spectral and spatial resolution which are planned for the next generation x-ray telescope, can be invaluable for separating the ejecta component of the spectra from the shocked ISM and for establishing whether surface brightness variations within a remnant are due to a filling factors or density inhomogenities. Observations with spectral resolution of $\Delta E/E \lesssim 1\%$ with or without spatial resolution would allow measurement of lines from individual ionic species of the same element. These would allow more direct plasma diagnostics than those in this thesis which had to infer the fine structure from lower resolution spectra.

Appendix

This appendix gives details on various parts of the NIE model. Its primary purpose is for people trying to understand the computer code, but some useful information is also covered. Warning to the casual reader: Gory detail within.

Hydrodynamics

The first step in calculating the model is to determine the profiles for the density and mean temperature as a function of time within the remnant. To accomplish this, an explicit finite element analysis given by Richmeyer (1967) is employed to solve the hydrodynamic equations for a spherically symmetric expanding shock front. This method included an artificial viscosity term that smoothed the discontinuity at the shock boundary. As opposed to using a Sedov solution (Sedov, 1959), with this method it is possible to calculate the temperature and density conditions in the matter that was ejected as well as the ISM. Sedov solutions also are only appropriate when one is interested in times that are long compared to the time required for the shock wave to sweep past an amount of material equal in mass to the material ejected from the supernova. This time, t_s, is given by

$$t_s = 160 \left(\frac{M_e}{M_\odot}\right)^{\frac{5}{6}} \left(\frac{n_0}{1\ \mathrm{cm}^{-3}}\right)^{-\frac{1}{3}} \left(\frac{E_0}{10^{51}\ \mathrm{ergs}}\right)^{-\frac{1}{2}} \text{ years}$$

where M_e is the mass of the ejecta. For some supernovae, this time can be a few thousand years - times that can be longer than or comparable to the ages of young supernova remnants.

To calculate the hydrodynamics, the equations are written in Lagrangian co-ordinates. In Lagrangian co-ordinates, the co-ordinate system is fixed to the gas so that the equations are used in a co-moving frame of reference. The equations simplify because the convective derivative, $d/dt + v \cdot \nabla$, reduces to d/dt.

As given by Richmeyer, the equations to be integrated when written in Lagrangian form are given by

$$\frac{dR}{dt} = u$$

$$\frac{du}{dt} = -\frac{1}{\rho_0}\left[\frac{R}{r}\right]^2 \frac{dp}{dr}$$

$$\frac{d\varepsilon}{dt} = -p\frac{dV}{dt}$$

$$\varepsilon = \frac{pV}{\gamma - 1} \quad .$$

The first two equations describe the mapping from a Lagrangian co-ordinate (r) to a Eulerian co-ordinate (R) as a function of time (t). u is the velocity of a gas element in Eulerian co-ordinates as a function of r. The rate of change of u is related only to the gradient in the gas pressure (p). Here we have neglected photon pressure as well as magnetic pressure. The factor $(1/\rho_0)\,(R/r)^2$ arises from the transformation factor dr/dR times the inverse of the density. This will be shown below. The third equation gives the rate of change of the internal energy per unit mass (the specific energy; ε) for a gas element undergoing adiabatic flow. V is the volume per unit mass (specific volume) which, as is evident by its definition is equal to the inverse of the density (ρ). Since the flow is assumed to adiabatic heat conduction and radiative cooling have been neglected. As will be seen below in the finite element equations only expansions of gas elements ($DV/dt > 0$) are truly adiabatic. Compression will have an extra heating term. The last equation is the equation of state which relates the specific energy to the pressure and the specific volume. γ is the ratio of specific heats. The arbitrary density constant, ρ_0, is a conversion factor between the Eulerian co-ordinates and the Lagrangian co-ordinates. This is given by

$$r^3 = \frac{3}{\rho_0}\int_0^R \rho(r')r'^2 dr' \quad .$$

By taking the implicit derivative of both sides the equation relating the specific volume to the relation between the Lagrangian and Eulerian co-ordinates is shown to be

$$V = \frac{1}{\rho} = \frac{1}{\rho_0}\left[\frac{R}{r}\right]^2 \frac{dR}{dr} \quad .$$

These equations in their finite element form as given by Richmeyer are

$$u_j^{n+1} = u_j^n - \frac{\Delta t}{\rho_0 \Delta r_j}[(p_{j+\frac{1}{2}}^n - p_{j-\frac{1}{2}}^n) + (q_{j+\frac{1}{2}}^n - q_{j-\frac{1}{2}}^n)]\left[\frac{R_j}{r_j}\right]^2$$

$$R_j^{n+1} = R_j^n + u_j^{n+1}\Delta t$$

$$\varepsilon_{j+\frac{1}{2}}^{n+1} = \varepsilon_{j+\frac{1}{2}}^n - \left[\frac{p_{j+\frac{1}{2}}^{n+1} + p_{j+\frac{1}{2}}^n}{2} + q_{j+\frac{1}{2}}^{n+1}\right](V_{j+\frac{1}{2}}^{n+1} - V_{j+\frac{1}{2}}^n)$$

$$V_{j+\frac{1}{2}}^{n+1} = \frac{1}{\rho_0}\frac{(R_{j+1}^{n+1})^3 - (R_j^{n+1})^3}{(r_{j+1})^3 - (r_j)^3}$$

$$p_{j+\frac{1}{2}}^{n+1} = (\gamma - 1)\frac{\varepsilon_{j+\frac{1}{2}}^{n+1}}{V_{j+\frac{1}{2}}^{n+1}}$$

$$q_{j+\frac{1}{2}}^n = \begin{cases} \left[\frac{2a^2\rho_0^2(\Delta r)^2}{V_{j+\frac{1}{2}}^n + V_{j+\frac{1}{2}}^{n-1}}\right]\left[\frac{V_{j+\frac{1}{2}}^n - V_{j+\frac{1}{2}}^{n-1}}{\Delta t}\right]^2\left[\frac{r_{j+1}}{R_{j+1}^n}\right]^4 & (\text{if } V_{j+\frac{1}{2}}^n < V_{j+\frac{1}{2}}^{n-1}) \\ 0 & (\text{if } V_{j+\frac{1}{2}}^n \geq V_{j+\frac{1}{2}}^{n-1}) \end{cases}$$

The superscript n denotes the time mesh co-ordinate and the subscript j denotes the space mesh boundary co-ordinate. Variables with integral subscripts are ones which pertain to the boundaries of the space mesh. The velocity (u), the Lagrangian co-ordinate (r), and the Eulerian co-ordinate (R) are such quantities. The pressure (p), the energy per unit mass (ε), the specific

volume (V), and the pseudo-viscosity term (q) all refer to the contents between the shell boundaries and are given half-integral subscripts. In other words, the subscript $j+\frac{1}{2}$ refers to the region between boundary j and boundary $j+1$. The other variables above refer to the time-step (Δt), the ratio of specific heats ($\gamma = C_p / C_V$), and pseudo-viscosity constant (α). In all the models γ was taken to be 5/3 while α was set to 3/2.

Note that the pseudo-viscosity term vanishes unless the cell is under going compression. Therefore, it is non-zero at the shock front where it models the conversion of the kinetic energy of the gas to internal energy at shock fronts, but plays no role in the post-shock region where the gas is expanding. In terms of entropy, the pseudo-viscosity models the irreversible heating of the gas at a shock, while behind the shock where the pseudo-viscosity vanishes the equations return to describing an adiabatic flow. One of the effects of the pseudo-viscosity parameter is to spread the shock front over a number of cells - a number roughly equal to the value of the viscosity parameter. The choice for this parameter has some effect on the emergent spectrum since the density distribution near shock front is altered. Itoh (1977) has studied this effect by changing the viscosity parameter from 1.5 to 2.0 and finds the strengths of lines with energies greater than 0.65 keV change by less than 10%.

The conversion between the Eulerian co-ordinates and the Lagrangian co-ordinates in finite element form are given by

$$r_j = \left[\frac{3}{\rho_0} \int_0^{R_j} \rho_I(r') r'^2 dr' \right]^{\frac{1}{3}}$$

where ρ_I is the initial density distribution.

The specific volume in terms of the electron density, n_e, and the ion density, n_i, is given by

$$V = \frac{1}{(n_e + n_i)\mu m_p}$$

where m_p is the mass of the proton and μ is the average atomic weight per particle. Using solar abundances (Allen, 1976), the value μ is 0.60 and n_e / n_i is 1.087. This gives a conversion of specific volume to electron density which is given by

$$n_e = 5.228 \times 10^{23} \left(\frac{V}{1\ cm^3 gr^{-1}} \right)^{-1} \ \mathrm{cm}^{-3}$$

Combining the equation of state for an ideal gas ($p = (n_e + n_i) k T_m$) and the equation for energy per unit mass ($\varepsilon = pV(\gamma - 1)^{-1}$), the mean temperature can be expressed in terms of the specific energy as

$$T_m = 4.218 \times 10^9 \left(\frac{\varepsilon}{\mathrm{erg\ g}^{-1}} \right) \ \mathrm{K} \ .$$

As was described above, both ejecta region and the shocked circumstellar medium (CSM) were considered. The numerical integrations were begun at a time when the leading edge of the ejecta reached an arbitrarily chosen radius, R_I. This time was typically $\lesssim$ 1 - 2 years. The conditions of the ejecta at that time were parametrized. Let λ be the ratio of the radius, R, to the arbitrarily chosen starting radius, R_I. The starting pressure, density, and velocity distributions for $0 < \lambda \leq 1$ were taken as

$$p_I(\lambda) = p_{EJ} \lambda^{\alpha_p}$$

$$\rho_I(\lambda) = \rho_{EJ} \lambda^{\alpha_\rho}$$

$$u_I(\lambda) = u_{EJ} \lambda^{\alpha_u}$$

and for $\lambda > 1$

$$p_I(\lambda) = p_{CSM}$$

$$\rho_I(\lambda) = \rho_{CSM}$$

$$u_I(\lambda) = 0 \quad .$$

The constants p_{CSM} and ρ_{CSM} are the preshocked ISM pressure and density and are both input parameters to the model. The input parameters for determining the condition of the ejecta are the pressure index (α_p), the density index (α_ρ), the velocity index (α_u), the mass of the material ejected (M_e), the energy in the blast (E_0), and the fraction, f of the blast energy contained as kinetic energy in the bulk motion of the ejected material. The fraction of the blast energy contained in thermal motions in the ejecta is $1-f$. The constants p_{EJ}, ρ_{EJ}, and u_{EJ} are determined by the constraints

$$M_e = \int_{Ejecta} \rho_I \, dV = 4\pi\rho_{EJ} R_I^3 \int_0^1 \lambda^{2+\alpha_\rho} \, d\lambda$$

$$fE_0 = \int_{Ejecta} \tfrac{1}{2}\rho_I \, u_I \, dV = 2\pi\rho_{EJ} R_I^3 u_{EJ}^2 \int_0^1 \lambda^{2+2\alpha_u+\alpha_\rho} \, d\lambda$$

$$(1-f)E_0 = \int_{Ejecta} \frac{p_I}{\gamma-1} dV = \frac{4\pi R_I^3 p_{EJ}}{\gamma-1} \int_0^1 \lambda^{2+\alpha_p} \, d\lambda \quad .$$

These equations imply that

$$\rho_{EJ} = \frac{M_e(3+\alpha_\rho)}{4\pi R_I^3}$$

$$u_{EJ} = \left[\frac{fE_0(3+2\alpha_u+\alpha_\rho)}{2\pi R_I^3 \rho_{EJ}}\right]^{1/2} = \left[\frac{2fE_0(3+2\alpha_u+\alpha_\rho)}{M_e(3+\alpha_\rho)}\right]^{1/2}$$

$$p_{EJ} = \frac{(1-f)E_0(3+\alpha_p)(\gamma-1)}{4\pi R_I^3} \quad .$$

Of all the input discussed above, the only pertinent ones are E_0, M_e, and ρ_{CSM}. ρ_{CSM} will usually be expressed in terms of, n_0, the particle density of the unionized gas of the ISM. The rest of the parameters can be ignored. Itoh (1977) has shown that for times $\gtrsim t_s$ the x-ray spectrum is insensitive to a range of choices of the α's despite the fact that the ejecta remains a significant contributor to the x-ray spectrum. The quantity f might have some effect on the output spectrum except that we have assumed that it is near unity. The only reason for introducing f was to avoid numerical problems caused by having no internal energy initially in the ejecta shells. p_{CSM} was introduced for the same reason. Because the shock waves are of such high Mach number the post shock temperature is very large compared to the pre-shock temperatures that are determined by $(1-f)E_0$ and p_{CSM}. The post-shock temperature in that case is insensitive to the preshock temperature (eg Spitzer, 1978).

For the models used in this thesis the following set of initial conditions were always used:

$$R_I = 0.14\text{pc}$$

$$\alpha_u = 1 \quad \alpha_\rho = 0 \quad \alpha_p = -1$$

$$T_{CSM} = 9 \times 10^4\text{K} \quad f = .999$$

$$\gamma = \frac{5}{3} \ .$$

The numerical integrations were done with 13 shells for the ejecta and the ISM was kept in 24 shells. Typically, 75% of them were contained in the shock region. Rezoning was done when the leading shock reach near the last ISM shell. Neighboring ISM shells were averaged together so that the ISM part of the net was collapsed by a factor of 2 and new unshocked ISM was put in the outer shells. The

ejecta was never rezoned. Stability of the numerical integrations was maintained by never letting the specific volume of any shell change by more than 20%. To keep the integration moving along, another requirement on the hydrodynamic time step was that the specific volume of at least one shell had to change by 10%. About 800 time steps were required to integrate a model to 8000 years.

Figures 1 and 2 show the results of running a typical model. Model parameters are shown on the figures. Figure 2 shows the different hydrodynamic quantities plotted as a function of time. The shock radius grows linearly with time during the early free expansion phase, but at the sweep-up time, the growth approaches a Sedov solution. As expected, the shock temperature remains constant, and begins to fall after the sweep-up time as $t^{-6/5}$. Figure 1 shows quantities plotted as a function of radius at a given time. This figure demonstrates some of the general features predicted by these models. First there is the unshocked CSM which is taken to be of uniform density and some ignorably low temperature. Further in, where the shock is encountered, the CSM is compressed and heated. The next distinct feature is the reverse-shocked ejecta region. A contact discontinuity separates ejecta region from the shocked CSM. As can be seen, the ejecta compresses up into a thin shell with high density and lower temperature. As the densities drop toward the center of the remnant, the shock velocity and temperatures increase.

The density and temperature profiles predicted from a Sedov solution is shown. Also note that the density jump behind the shock which in theory should be 4 is slightly smaller in the numerical model. This is due to the artificial viscosity term spreading the shock out over a few shells.

Ignoring the dynamical instabilities at the contact discontinuity may be one of the failings of the model. Pressure equilibrium does exist at the interface

(nT_m is constant), but the deceleration of the ejecta makes the interface vulnerable to Rayleigh-Taylor instabilities. This would have two effects on how the model compares to reality. First, because the density gradients at the interface would be relaxed, the model would overestimate the density in the ejecta shell and hence would overestimate the emission volume ($\int n_e^2 dV$) of the ejecta. Second, the model would not take account of the mixing of the heavy element enriched, ejecta material into the higher temperature, shocked CSM.

Electron Temperature

The electron temperature is a key parameter in determining the emergent x-ray spectrum from a hot plasma. The ion temperature is ignorable as long as it is much less than $(m_e / m_i)T_i$. Despite the fact that the electron temperature at a given place in the remnant is always changing it is assumed that the electron gas can be described by a Maxwellian distribution. The energy exchange time for electrons from Spitzer (1962) is

$$t_{ee} = \frac{0.27 T_e^{\frac{3}{2}}}{n_e \ln\Lambda} \text{ s}$$

$$= 7.3 \left[\frac{T_e}{10^7 \text{ K}}\right]^{3/2} \left[\frac{n_e}{1 \text{ cm}^{-3}}\right]^{-1} \text{ years} \quad .$$

This is sufficiently short to be ignorable.

One potential non-equilibrium effect concerns the lack of equipartition of energy between the electrons and the ions behind the shock front. The reason this may occur is that in the frame of the shock the velocities of both the electrons and the ions in the frame moving with the shock front are the same. If these ballistic motions were converted behind the shock to thermal motions in the limit of no energy exchange between ions and electrons, then the $T_e / T_i \sim$

m_e/m_i. It has been suggested that collective plasma instabilities at the shock front can provide a mechanism for energy exchange (McKee, 1974). Whether these instabilities are capable of eradicating the energy difference during the time it takes the material to cross the shock front is not clear. In the case of the low Mach number collisionless shock caused by the solar wind impinging on the magnetosphere of the earth, it has been observed that the electron temperature behind the shock is lower than the ion temperature. If that is indeed the case for the high Mach number shocks caused by the interaction of supernova ejecta with the CSM, then Coulomb collisions will be necessary to equilibrate the two temperatures.

The time scale for equipartition of energy between electrons and the i^{th} ionic species, $t_{eq,i}$, as given by Spitzer (1962) is

$$t_{eq,i} = \frac{3m_e m_i k^{\frac{3}{2}}}{8(2\pi)^{\frac{1}{2}} n_i Z_i^2 \ln\Lambda} \left(\frac{T_e}{m_e} + \frac{T_i}{m_i} \right)^{\frac{3}{2}}$$

$$\cong 8000 \left(\frac{T_e}{10^7 \text{K}} \right)^{\frac{3}{2}} \left(\frac{n_i}{1 \text{cm}^{-3}} \right)^{-1} \text{ years} \qquad \left(\frac{T_e}{m_e} \gg \frac{T_i}{m_i} \right).$$

If Coulomb collisions are the principal electron-ion energy equilibration mechanism in young supernova remnants, then the electron temperature would be somewhat lower than would be implied by the shock velocity.

In the model, this uncertainty in what happens to the electrons at the shock front is handled by considering the two extreme cases. The first case is simply that the electrons are brought into thermal equilibrium with the ions at the shock front so that $T_e = T_i = T_m$. In terms of the variables discussed in the hydrodynamics section above, T_e is given by

$$T_e = T_m = 4.218 \times 9^{10} \left(\frac{\varepsilon}{\text{erg g}^{-1}} \right) \text{ K} .$$

In the opposite case, the electrons are assumed to cross the shock front cold and subsequently be heated by Coulomb collisions with ions. Details concerning the initial conditions are discussed below. In this approximation the electrons can be analyzed as a distinct fluid undergoing non-adiabatic expansion. The equations governing this expansion are the rate of change of the electron specific energy (ε_e) and the equation of state. These are

$$\frac{d\varepsilon_e}{dt} = \frac{d}{dt}[(\gamma-1)p_e V] = -p_e \frac{dV}{dt} + Q$$

$$p_e = n_e k T_e$$

where d/dt is the Lagrangian time derivative, p_e is the electron pressure, V is still the specific volume, and Q is electron heating rate. The electron heating rate is given by Spitzer (1962) as

$$Q = \frac{3}{2} V n_e k (T_i - T_e) \sum_k t_{eq,k}^{-1} \quad .$$

From above, assuming $T_e / m_e \gg T_i / m_i$,

$$\sum_k t_{eq,k}^{-1} = \frac{\ln\Lambda n_e A_e^{1/2}}{5.87 T_e^{\frac{3}{2}}} \left(\frac{n^{\mathrm{H}}}{n_e}\right) \sum_j \left(\frac{n_k}{n_{\mathrm{H}}}\right) \frac{Z_k^2}{A_k}$$

where the sum k goes over all the different elements, A_e is mass of the electron in amu, and A_k is the mass of element k^{th} in amu. For solar abundances this gives

$$\sum_k t_{eq,k}^{-1} = 2.263\times10^{21} \frac{\ln\Lambda}{V T_e^{3/2}} \ s^{-1}$$

It useful to next transform $T_i - T_e$ factor to $T_m - T_e$. T_m is defined as

$$T_m = \frac{n_e T_e + n_i T_i}{n_e + n_i}.$$

By subtracting T_e from both sides the desired conversion is derived,

$$(T_i - T_e) = \left[\frac{n_e}{n_i} + 1\right](T_m - T_e) = 2.087(T_m - T_i),$$

is obtained. Substituting into the Q equation the expression for $T_i - T_e$ and the expression for $\sum_j t_{eq,j}^{-1}$ results in

$$Q = 3.93\times10^{29}\frac{\ln\Lambda(T_m - T_e)}{VT_e^{\frac{3}{2}}} \text{ erg s}^{-1}\text{ g}^{-1}.$$

Much manipulation can be performed on the energy equation. Substituting the final expression for Q, substituting the equation of state and adding the adiabatic expansion term to both sides results in

$$\frac{d}{dt}\left[\frac{3}{2}n_e k T_e V\right] + n_e k T_e \frac{dV}{dt} = C_Q \frac{\ln\Lambda(T_m - T_e)}{VT_e^{\frac{3}{2}}} .$$

The expression $n_e V$ is a constant which derivative does not act on. After multiplying through by $T_e^{\frac{1}{2}}/n_e V k$ and making a substitution of $x = T_e / T_m$ the equation becomes

$$\frac{d}{dt}\left[VT_m^{\frac{3}{2}}x\right] = \frac{C_Q \ln\Lambda}{k(n_e V)}\left[\frac{1}{x} - 1\right]$$

For a gas with a ratio of specific heats of 5/2 undergoing adiabatic expansion the expression $VT_m^{\frac{3}{2}}$ is a constant. This results in the final equation to be integrated:

$$\frac{dx}{dt} = \frac{C\ln\Lambda}{VT_m^{\frac{3}{2}}}\left[\frac{1}{x} - 1\right] x^{-\frac{1}{2}} .$$

The variable C is a constant with a value of 5.50×10^{21} $cm^3\, K^{\frac{3}{2}}\, s^{-1}\, g^{-1}$ The Coulomb logarithm, $\ln\Lambda$, which is a weak function of density and temperature, was evaluated by logarithmically interpolating a table presented in Spitzer (1962).

The finite difference equation used to numerically calculate the electron temperature is

$$T_e{}^{n+1} = T_m{}^n \left[x^n + 7.104\times10^{-3} \frac{n_e \Delta t \ln\Lambda(n_e{}^n, T_m{}^n)}{(T_m{}^n)^{3/2}} \left(\frac{1}{x^n} - 1 \right) \right]^{x^-}_{x\ 1/2}$$

Implicitly, all the subscripts of the temperature and density variables are $j+\frac{1}{2}$.

As Itoh (1978) pointed out, in the approximation that $\ln\Lambda$ is constant, equation for dx/dt above can be integrated by separation of variables as follows :

$$\int_{x_0}^{x} \frac{x^{\frac{3}{2}}}{1-x} dx = \frac{C\ln\Lambda}{VT_m{}^{\frac{3}{2}}} \int_{t_0}^{t} dt$$

$$X(x) - X(x_0) = \frac{C\ln\Lambda}{VT_m{}^{\frac{3}{2}}} (t - t_0).$$

The integrand $X(x)$ is given by

$$X(x) = \frac{3}{2} \ln\left[\frac{1+x^{\frac{1}{2}}}{1-x^{\frac{1}{2}}} \right] - x^{\frac{1}{2}}(x+3).$$

At first glance this transcendental equation might seem preferable to the finite difference method to perform a time step. Given an x^n at t^n in a particular cell, the value of x can be computed for an arbitrarily large time step, Δt, by varying x^{n+1} to find the root of the following expression:

$$X(x^{n+1}) - X(x^n) - \frac{C\ln\Lambda}{VT_m{}^{\frac{3}{2}}} \Delta t \ .$$

However, because of the numerous system function calls (LOG and SQRT) required to find a root, many "finite difference" interactions can be made in the time to perform one "transcendental" iteration. Therefore, the "transcendental" was used only when fractional change of the electron temperature in a spatial cell was large. details are discussed in the section concerning numerical details.

As was discussed above, the initial electron temperature behind the shock front is somewhat controversial. It being the intent of this Coulomb heating model to address the possibility of "cold" electrons, the pertinent question is: Below what limit do the exact initial conditions for the electron temperature become ignorable in terms of the predicted x-ray spectrum? One way to estimate this limit is to examine the behavior of equation for dx/dt above in the limit of small x. The equation under those circumstances is

$$\frac{dx}{dt} = \frac{C\ln\Lambda}{VT_m^{\frac{3}{2}}} x^{-\frac{3}{2}} .$$

After separating by parts, integrating both sides and solving for x the early behavior of $x(t)$ is shown to be

$$x(t) = \left[\frac{C\ln\Lambda}{VT_m^{\frac{3}{2}}} (t - t_0) + x_0^{\frac{5}{2}} \right]^{\frac{2}{5}} .$$

Once the value of t gets large enough so that the magnitude of the first term in the brackets is large compared to the second term, the question of the value of x_0 becomes moot. Substituting in for V in terms of n_e and using a nominal value of 32 for $\ln\Lambda$ in the above equation, the upper limit for x_0 can be expressed as

$$x_0 \ll 4.9\times10^{-2} \left[\frac{n_e}{1\ \mathrm{cm}^{-3}} \right]^{\frac{2}{5}} \left[\frac{t}{50\ \mathrm{years}} \right]^{\frac{2}{5}} \left[\frac{T_m}{10^6\ \mathrm{K}} \right]^{\frac{3}{5}} .$$

In practice an initial temperature of 20000 K was used which usually gave an $x_0 \lesssim 0.001$.

Figure 3 shows the evolution of the electron temperature. Time axis is in units of t_{heat} (= $VT_m^{3/2}/C\ln\Lambda$). For times less than t_{heat} the function does follow a $t^{2/5}$ power law.

Ionization Structure of the Heavy Elements

It is assumed that hydrogen and helium nuclei are completely stripped of their electrons by the time they have spent any significant amount of time behind the shock front. They could have been photoionized by ionizing radiation from the initial supernova blast or from the shocked CSM region while still upstream of the shock. If there is any significant heat conduction across the shock front, some amount of electron collisional ionization could occur in the pre-shocked material. If all else fails, given the temperatures and densities that occur in and behind the shock, electron collisions should be able to do the job in short order ($\lesssim$10 years).

In addition to the light elements, the same scenario pertains to the outer few electrons of the high Z elements (3 - 10 , depending on the Z). However, given electron collisions as the only significant mechanism, the remnant will be quite old ($\gtrsim$ 20000 years) before the x-ray spectrum will no longer be affected by the fact that the ionization temperature of much of the shocked gas is not equal to the electron temperature.

A typical equation that needs to be integrated for given ionic species of a given element is

$$\frac{1}{n_e}\frac{dX_{Z,z}}{dt} = i_{Z,z-1}X_{Z,z-1} - (i_{Z,z}+r_{Z,z})X_{Z,z} + r_{Z,z+1}X_{Z,z+1}$$

where $X_{Z,z}$ is the fractional abundance of ionic species with charge $z-1$ of an

element with nuclear charge Z, $n_e i_{Z,z}$ is the rate for an atom with nuclear charge Z in ionic state z to ionize to state $z+1$ via electron collisions, and $n_e r_{Z,z}$ is the rate in which an atom with nuclear charge Z and ionic state z recombines with an electron to form ionic state $z-1$. The fractional abundance is defined such that

$$\sum_{z=1}^{Z+1} X_{Z,z} = 1 \ .$$

The set of values $\{X_{Z,1}, X_{Z,2}, \ldots, X_{Z,Z+1}\}$ shall hereafter be referred to as the ionization structure of the element with nuclear charge Z. Ionization and recombination rates were calculated from the Raymond and Smith plasma code. They are, in the limit of low densities found in supernova remnants, only functions of electron temperature.

For a given element, the problem of the time development of the ionization structure entails the solution of a set of Z+1 coupled differential equations. If the ionization structure is represented as a column vector,

$$\vec{X}_Z = \begin{bmatrix} X_{Z,1} \\ X_{Z,2} \\ \cdot \\ \cdot \\ X_{Z,Z+1} \end{bmatrix} ,$$

then the whole system can be represented as

$$\frac{1}{n_e} \frac{d\vec{X}_Z}{dt} = \mathbf{A}_Z \, \vec{X}_Z$$

where $\mathbf{A}_Z$ is the following matrix:

$$\mathbf{A}_Z = \begin{bmatrix} -i_{Z,1} & r_{Z,2} & 0 & . & & & \\ i_{Z,1} & -(i_{Z,2}+r_{Z,2}) & r_{Z,3} & 0 & . & & \\ 0 & i_{Z,2} & . & . & . & . & \\ . & 0 & . & . & . & 0 & . \\ & . & . & . & . & r_{Z,Z} & 0 \\ & & . & 0 & i_{Z,Z-1} & -(i_{Z,Z}+r_{Z,Z}) & r_{Z,Z+1} \\ & & & . & 0 & i_{Z,Z} & -r_{Z,Z+1} \end{bmatrix}$$

As was discussed above, the coefficients of the matrix $\mathbf{A}_Z$ are only functions of electron temperature. In the context of the SNR problem, because of time dependence of the electron temperature at a given Lagrangian radius in the remnant, the coefficients are also implicitly functions of time. Despite that, insight as well as a verification for a numerical code can be gained by examining the evolution of the ionization structure in a constant temperature plasma. In that case, an analytical solution can be found, in principle, since the problem reduces to a system of linear differential equations with constant coefficients. The solution can be expressed as

$$\vec{X}_Z(t) = \mathbf{E}\, e^{\Lambda n_e (t-t_0)}\, \mathbf{E}^{-1}\, \vec{X}_{Z,0}$$

where $\vec{X}_{Z,0}$ is the ionization structure at t = t_0 and $\mathbf{E}$ and Λ are matrices containing the eigenvectors, $\vec{e}_j$, and the eigenvalues, λ_j, of matrix $\mathbf{A}_Z$. They are arranged in the respective matrices as follows:

$$\mathbf{E} = \begin{bmatrix} & & \\ \vec{e}_1 \vec{e}_2 .. \vec{e}_{Z+1} & & \\ & & \end{bmatrix} \qquad \Lambda = \begin{bmatrix} \lambda_1 & & & \\ & \lambda_2 & & \\ & & . & \\ & & & \lambda_{Z+1} \end{bmatrix} .$$

This solution assumes no accidental degeneracy in the eigenvalues.

Because $\mathbf{A}_Z$ is singular, one of the eigenvalues is identically zero. All the rest of the eigenvalues, λ_j, are of the order of $-(i_j + r_{j+1})$. The negative reciprocal of

the non-zero eigenvalues are the time constants of the evolution of the ionization structure. At times long compared with the largest time constant all the terms begin to vanish except for the eigenvector corresponding to the zero eigenvalue. This eigenvector, therefore, is the equilibrium state of the ionization structure.

The largest time constant (the negative reciprocal of the eigenvalue with the smallest non-zero absolute value) characterizes the time scale, in terms of $n_e t$, required for an element to reach ionization equilibrium at a given temperature. Figure 4 displays that time scale as a function of temperature for a number of different elements. The large jumps in the time scale occur when the electrons just start to "eat" into a filled shell.

The evaluation of the evolution of the ionization structure for each element within each spatial zone behind the shock front was done with a second-order Runge-Kutta method. The method expressed in finite element form was

$$\vec{X}_Z{}^{n+1} = \vec{X}_Z{}^n + \frac{\Delta t}{2}(n_e{}^n \vec{k}_Z^{(1)} + n_e{}^{n+1} \vec{k}_Z^{(2)})$$

$$\vec{k}_Z^{(1)} = \mathbf{A}_Z{}^n \vec{X}_Z{}^n \qquad \vec{k}_Z^{(2)} = \mathbf{A}_Z{}^{n+1}(\vec{X}_Z{}^n + \vec{k}_Z^{(1)})$$

where $\mathbf{A}_Z{}^n$ and $\mathbf{A}_Z{}^{n+1}$ are the coefficient matrices evaluated with $T_e{}^n$ and $T_e{}^{n+1}$, respectively.

Figure 5a shows a test run of Runge-Kutta method on a system where a group of carbons are put into a plasma of log T_e = 6.4. They initially are all in C^{+3} state. The ionization time scale is marked on the plot. Figure 5b shows the same situation solved by the analytic method. Both methods show agreement.

Maintaining numerical accuracy during the rapid early evolution of the ionization structure in the zones immediately behind the shock constrained Δt severely. Since the electron temperature changes less rapidly, it might seem possible to decrease the computation time by assuming that the electron

temperature can be set equal to some mean constant value for some longer Δt and use the analytic solution to evolve the ionization structure from t to $t+\Delta t$. Analogous to the problem with electron temperature discussed above, each time step would require more calculations than the Runge-Kutta method, so this pseudo-analytic method only be used in time-space zones where bottlenecks have developed. Unfortunately, calculating Λ, $\mathbf{E}$, and $\mathbf{E}^{-1}$ was not as straightforward as it would appear. The coefficients of matrix $\mathbf{A}_Z$ vary by many orders of magnitude. In practice, this caused severe enough propagation of round-off error, even with the use of double precision. By the time $\mathbf{E}^{-1}$ was calculated the answer was rendered meaningless. We are convinced the problem is soluble by spending more time to find a different way, other than using canned routines, to calculate the needed quantities or by using more extended precision available with some compilers. We unfortunately had neither. We reverted back to using the finite element approach.

As was discussed above, a number of the outer electrons of the high Z elements will be stripped off in short order after crossing the shock front. To facilitate the numerical integrations, all the atoms of a given element were assumed to be initially in an advanced ionic state. The elements considered and their initial state are: C^{+4}, N^{+5}, O^{+5}, Ne^{+5}, Mg^{+5}, Si^{+5}, S^{+6}, Ar^{+6}, Ca^{+6}, Fe^{+6}, and Ni^{+6}. Because of the relatively large ionization rates that still occur at these stages of ionization, the transient effects caused by this *ad hoc* choice of initial conditions should be eliminated in ~ 10 - 20 years.

X-ray Spectrum Calculation

At a given time the x-ray photon spectrum can be calculated for a given element with nuclear charge Z_k as follows

$$\frac{dN}{dE}(E,t,Z_k) = \frac{1}{E}\frac{4\pi}{3}\sum_j \Lambda(E,T_{e,j+\frac{1}{2}}(t),\vec{X}_{Z_k,j+\frac{1}{2}}(t))\, n^2_{e,j+\frac{1}{2}}(t)\,[R^3_{j+1}(t)-R^3_j(t)]$$

where Λ is the x-ray emissivity based on a restructured version of the Raymond and Smith plasma code. Two spectra are calculated. One where the sum is over the ejecta shells; the other is over the shocked CSM shells. The spectra were calculated using solar abundances given by Allen (1976).

A final spectrum can be evaluated by

$$\frac{dN}{dE}(E,t) = \sum_k (A_{Z_k,ej}\ \frac{dN}{dE}(E,t,Z_k)\,|_{ej} + A_{Z_k,CSM}\,\frac{dN}{dE}(E,t,Z_k)\,|_{CSM})$$

where AZ_k,ej and $A_{Z_k,CSM}$ are abundances relative to solar of element k in the ejecta and the CSM, respectively.

Miscellaneous Computing Details

All computing was performed on a VAX 11/780 computer that is part of the High Energy Physics Computing Facility at Caltech (a.k.a HEP VAX). The VAX ran under the *UNIX*+ operating system (Seventh Version). The bulk of the code was written in Fortran 77, with some low level subroutines written in C.

The first part of the modeling just included calculation of the hydrodynamics, electron heating (if applicable), and ionization structure. During the integration the state of the remnant at various ages was output to disk storage. The interval between the output ages was increased logarithmically as the age

+ *UNIX* is a Trademark of Bell Labs.

increased - ~200 years at the beginning, ~2000 years at the end. The amount of CPU time required to integrate a supernova remnant to 8000 years was ~35 minutes. It varied by ± 15 minutes depending on the choice of β and η.

The electron heating calculation was nested inside the hydrodynamic calculation. Typically, the electron heating needed a smaller time-step than the hydrodynamics to maintain numeric stability, especially near the shock fronts. Time steps were chosen so that T_e changed by 3-5% per iteration. Separately, each shell was integrated until it "caught-up" with the hydrodynamics. If the number of time steps was estimated to be four or more and $T_e / T_i < 0.5$, then the "analytic method", described above, was used to increase efficiency. All of this was, of course, moot if electron-ion thermal equilibrium was assumed in the model. In that case T_e was set to T_m and the program moved on.

Further nested within the electron temperature calculation was the integration of the ionization structure. In a similar fashion to the electron heating, each element in each shell is integrated out at its own pace within a hydrodynamic time-step. The ionization heating mini-time step was chosen so that the fraction of atoms that transferred states during an iteration was between 0.5-1%. With an ionic state that was decreasing in population, the fractional change was never allowed to be greater than 20%. In order to improve stability and speed an ionic state was ignored if the population dropped below 0.001% and was still dropping. Care was taken to ensure that conservation of atoms was maintained during this freeze-out process.

The spectrum calculation was performed after the combined hydrodynamic/electron heating/ionic heating had been calculated. Some of the remnant states that had been output to disk were read in and the calculation proceeded as outlined above. This was a relatively sluggish calculation taking about 10-15 CPU minutes to process each spectrum. For this reason the

spectrum for only about 5 or 6 different epochs were calculated. Each spectrum was normalized to 10^{-12} photons s^{-1} cm^3 keV^{-1}.

Each run of the model corresponded to an η and a β and each epoch corresponded to a τ. Each spectrum was put into its appropriate slot on the grid. Because of disk space considerations, it was not possible to keep every element separate. The only elements that were kept separate were ones where abundances were likley to be varied during spectral fitting.

Finally, models were derived from logarithmic interpolation from the $\eta - \beta - \tau$ grid. The non-linear least square fitting was adopted from well-known and loved CURFIT routine in Bevington (1969).

Figure Captions

Figure 1

Different hydrodynamic quantities as a function of radius at a given time. Values for the blast energy, density, ejected mass, and age are given in the figure. Solid lines in the density and mean temperature graphs are a representation of an analytic approximation of a Sedov solution.

Figure 2

Different properties of a SNR as a function of time. Sedov solution shown in the shock radius graph.

Figure 3

The ratio of T_e to T_m as a function of time for constant T_m.

Figure 4

The ionization time scale for a dozen elements as a function of temperature.

Figure 5a

The fractional populations of the four most ionized states of carbon as a function of time. The electron temperature is assumed to log T=6.4 and all the carbons were initially in the C^{+4} state. Calculation was done with 2^{nd}-order Runge-Kutta method.

Figure 5b

Same as 5a except the calculation was done analytically.

Figure 6

An illustrative example of a model spectra from a 10^{6-8} K plasma. Characteristic lines from various elements are indicated.

$E_0 = 1.0$ $n_0 = 1.0$ $M_e = 0.5$ age $= 2.4 \times 10^3$

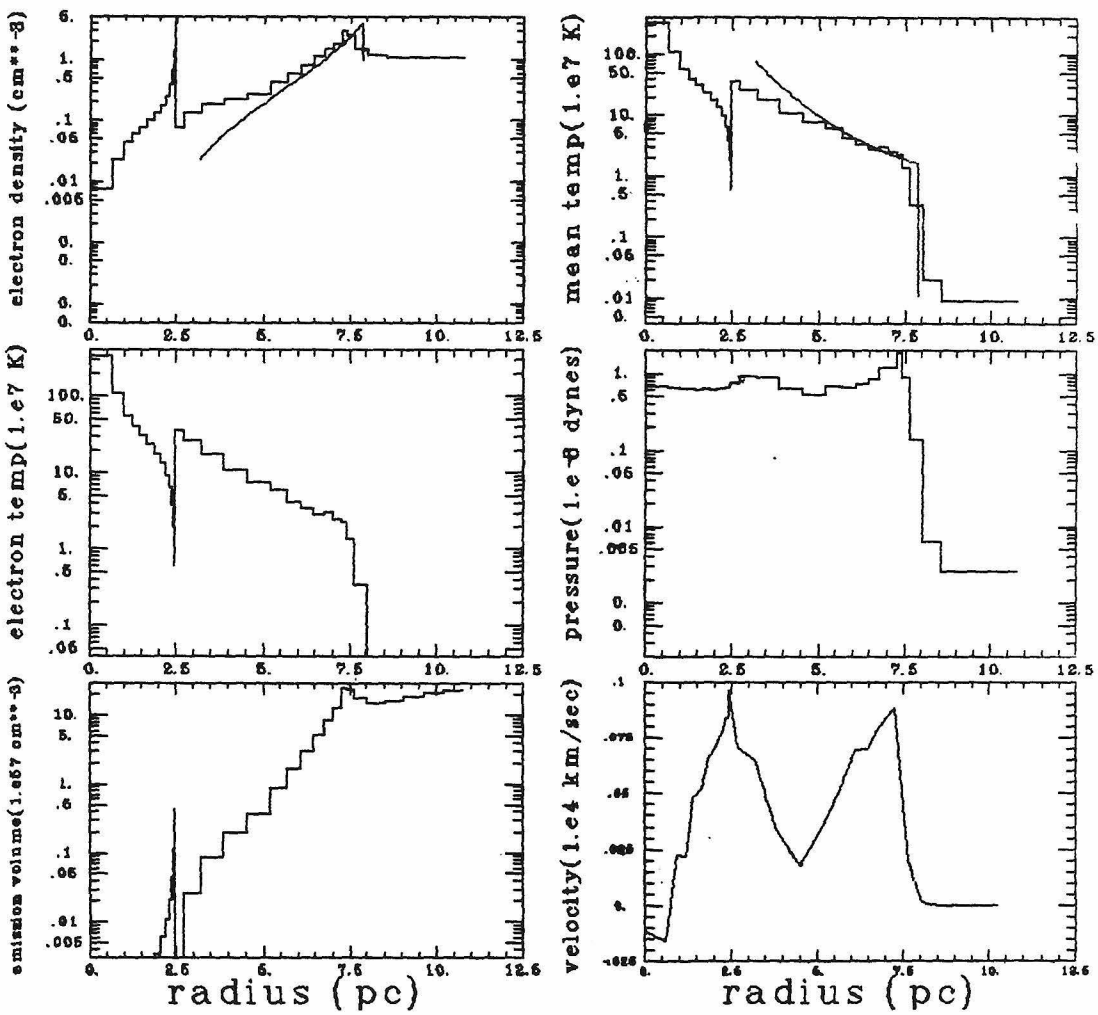

Figure 1

$E_0 = 1.0$ $n_0 = 1.0$ $M_e = 0.5$

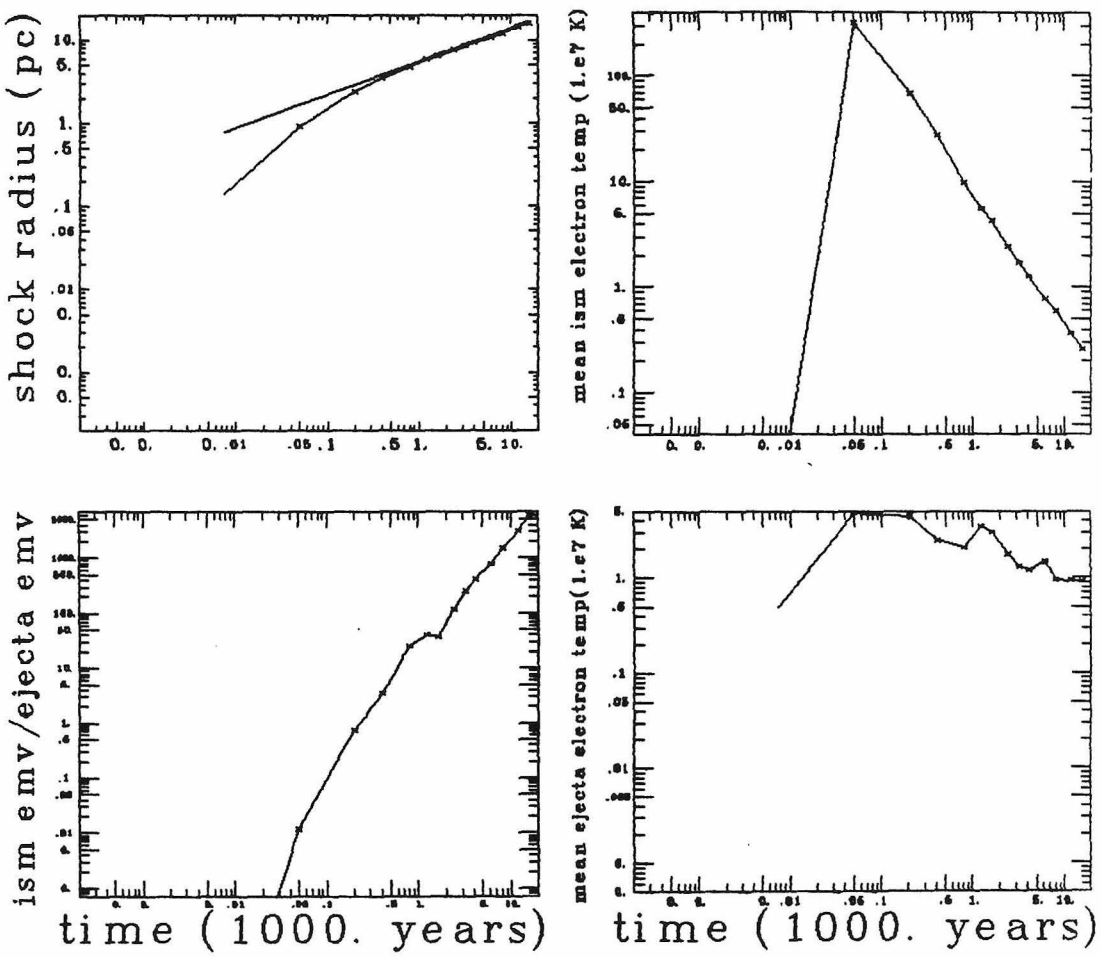

Figure 2

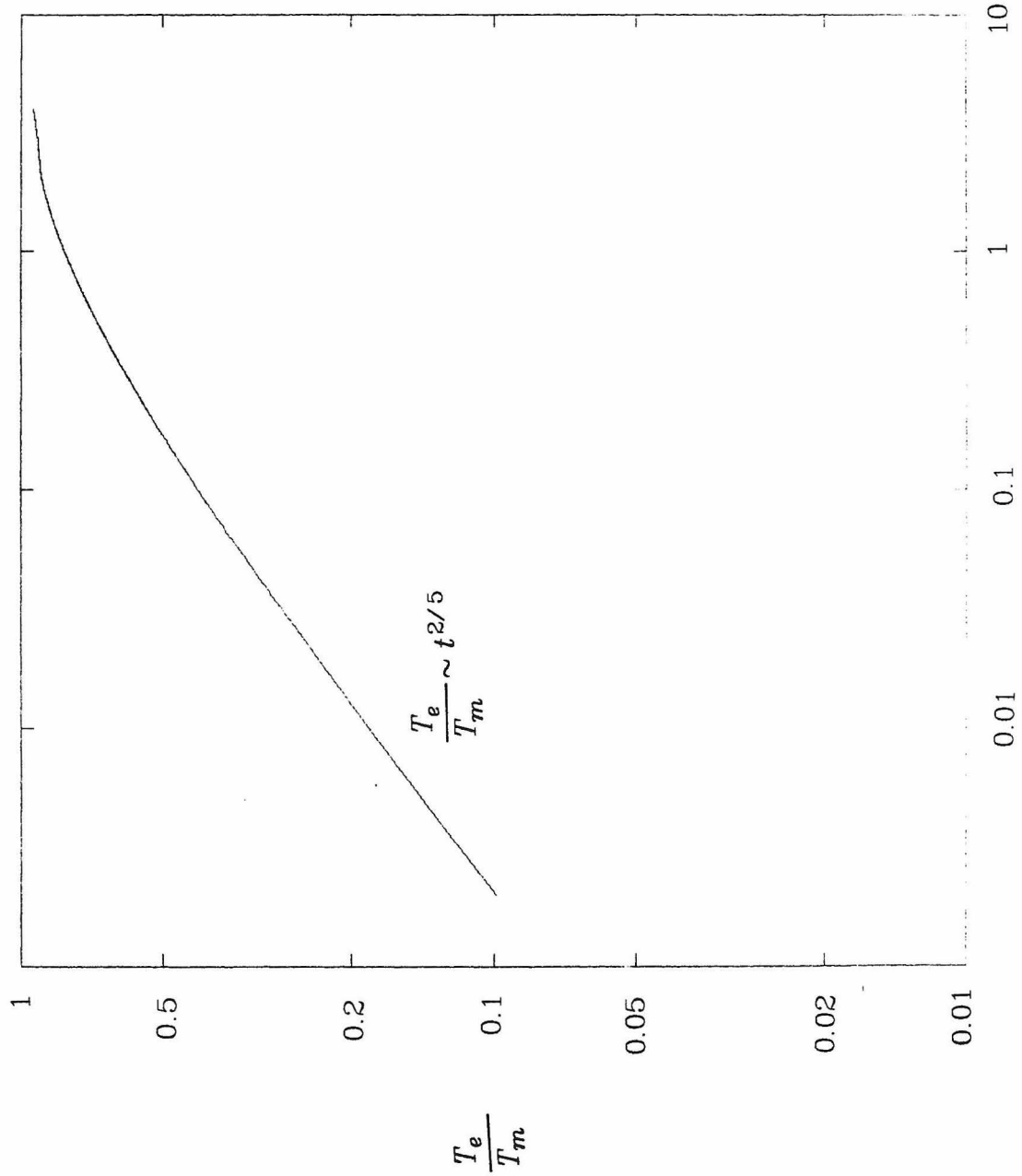
1
0.5
0.2
0.1
0.05
0.02
0.01
$\frac{T_e}{T_m}$
$\frac{T_e}{T_m} \sim t^{2/5}$
0.01
0.1
1
10
$(t / t_{h(0)})$

Figure 3

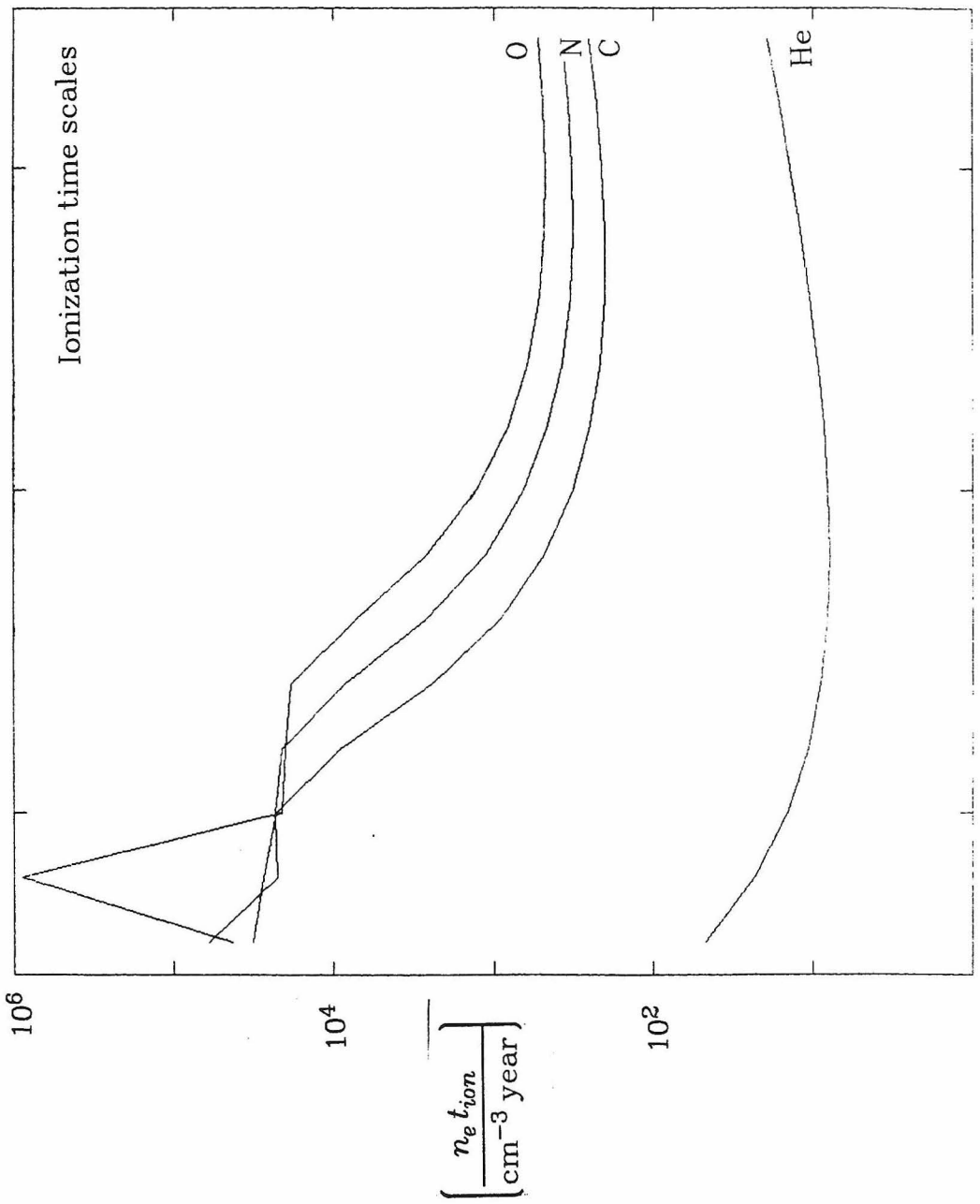
Ionization time scales
O
N
C
He
10^6
10^4
10^2
$\left(\frac{n_e t_{ion}}{\text{cm}^{-3}\text{ year}}\right)$
6
7
8
log T

Figure 4a

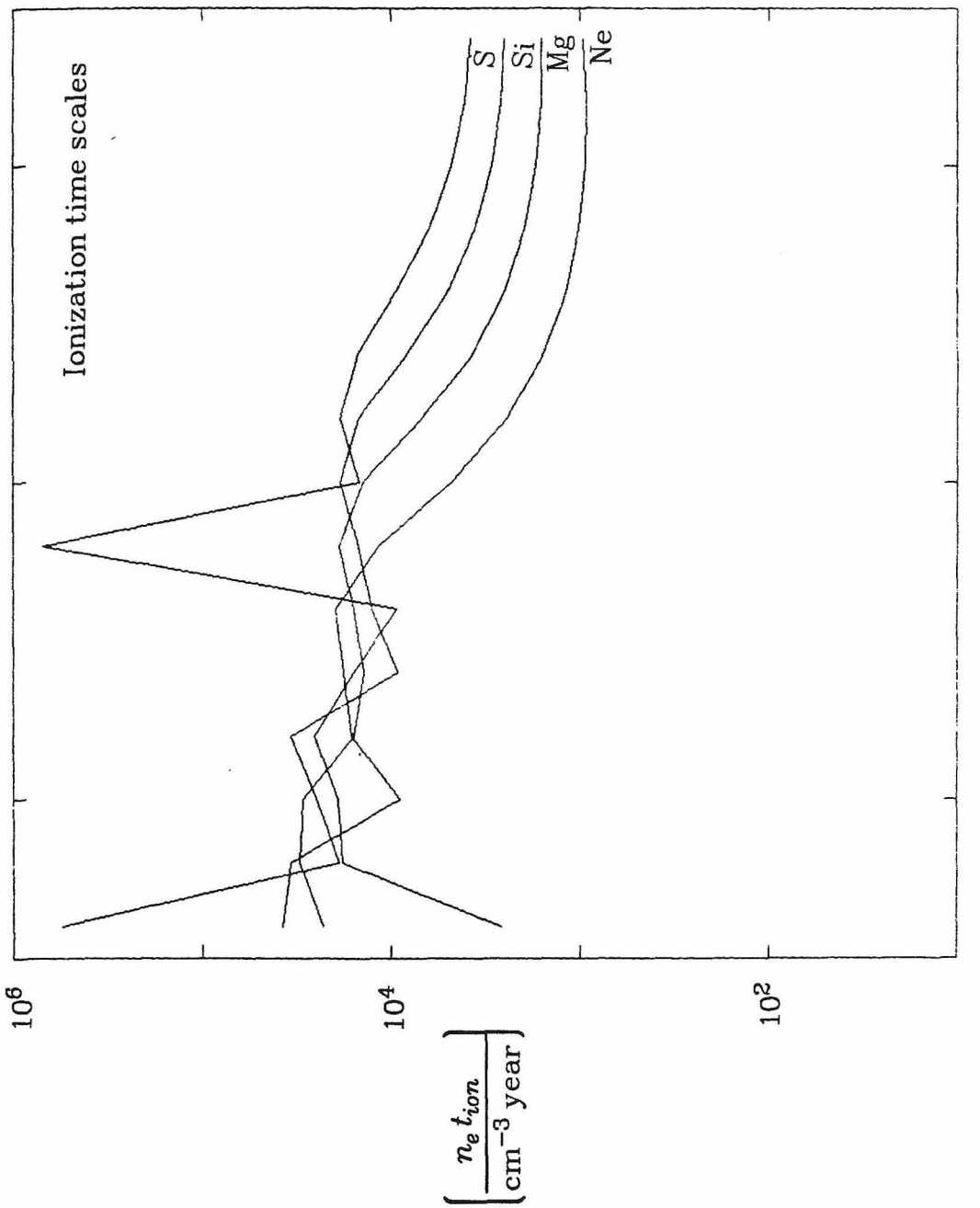
Ionization time scales
S
Si
Mg
Ne
10^6
10^4
10^2
$\left\{\frac{n_e\, t_{ion}}{\mathrm{cm}^{-3}\ \mathrm{year}}\right\}$
6
7
8
$\log T$

Figure 4b

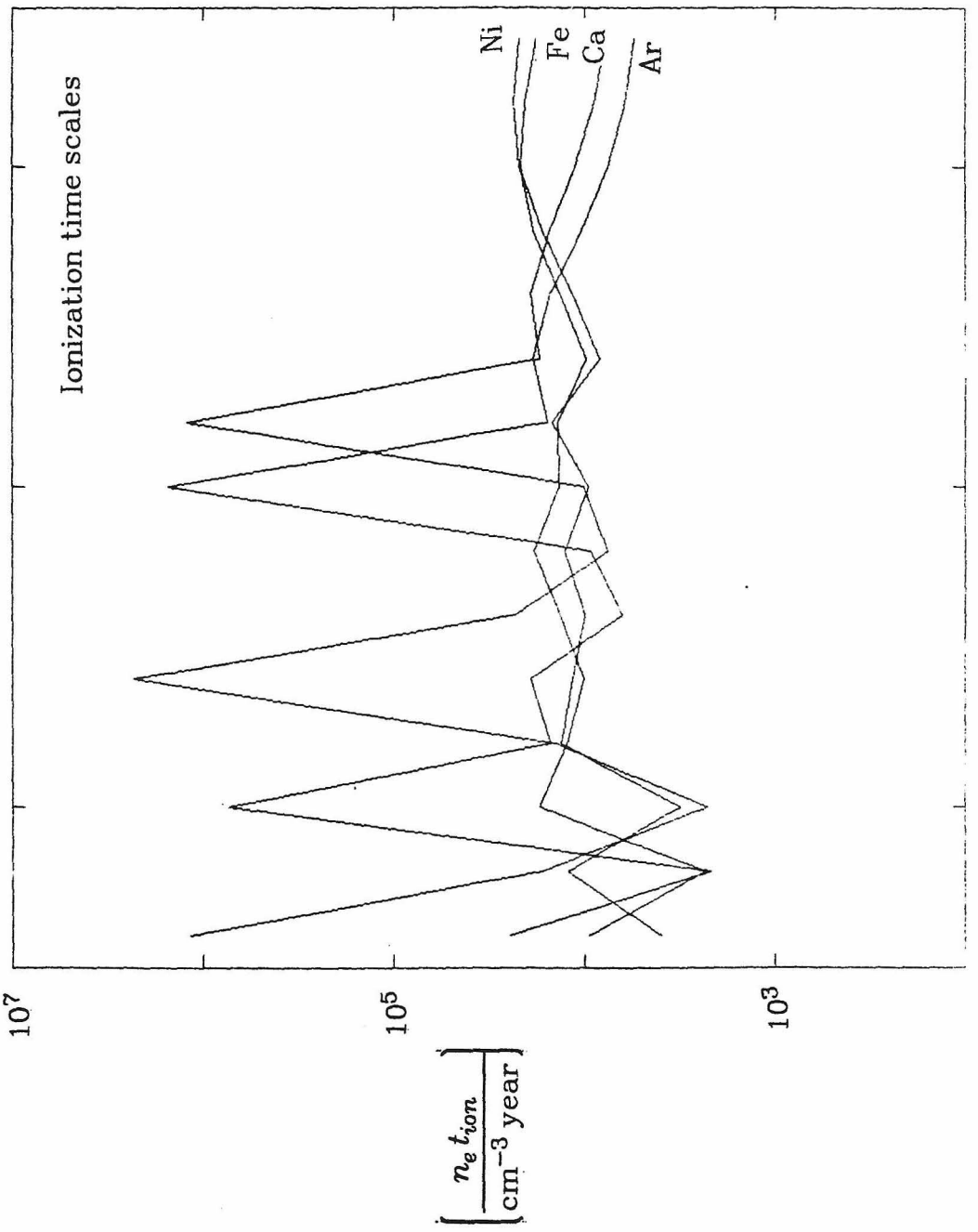
Ionization time scales
Ni
Fe
Ca
Ar
10^7
10^5
10^3
$\left\{\frac{n_e t_{ion}}{\text{cm}^{-3}\text{ year}}\right\}$
6
7
8
log T

Figure 4c

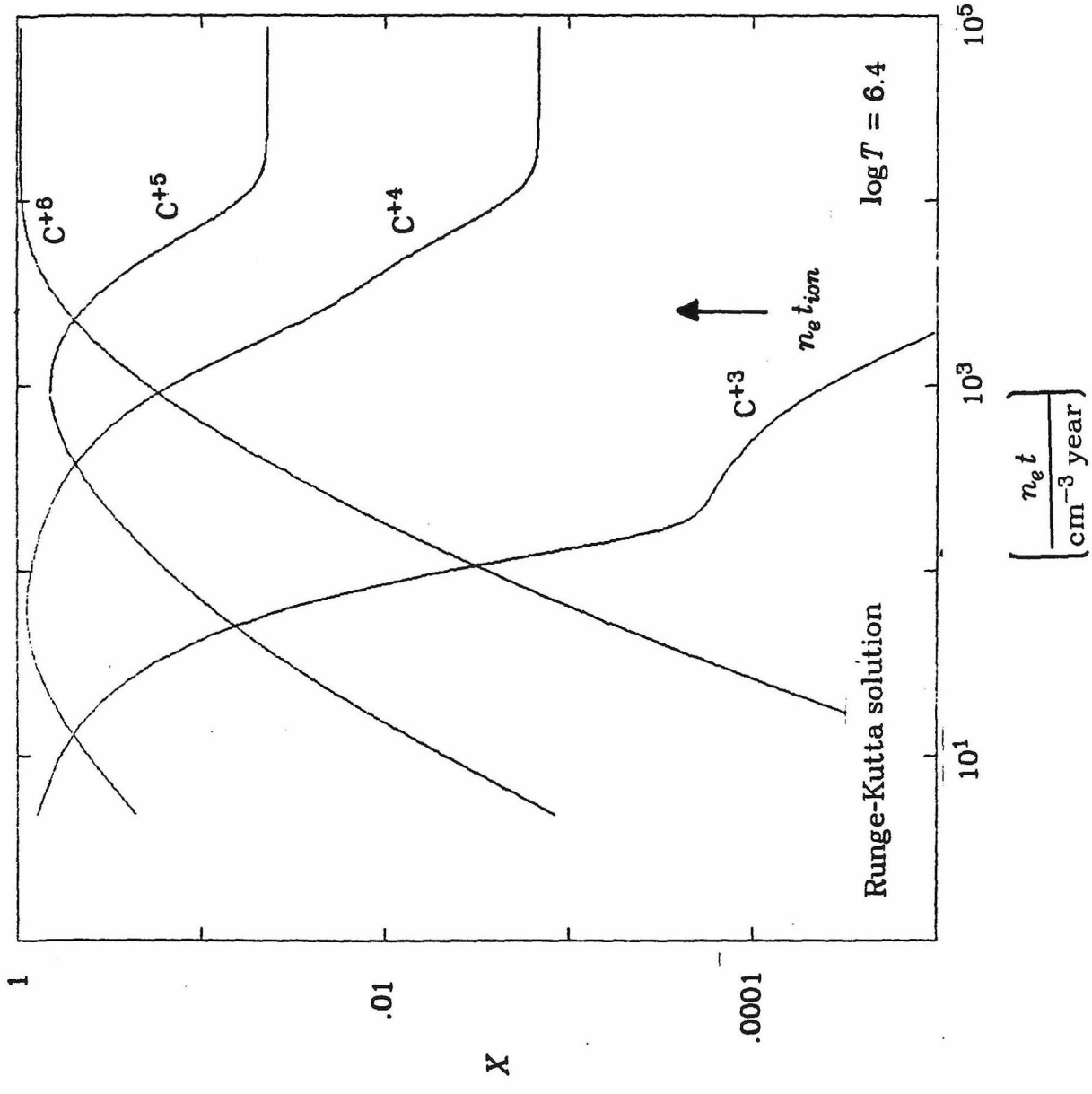
1
.01
.0001
X
10^1
10^3
10^5
$\left[\frac{n_e\,t}{\mathrm{cm}^{-3}\ \mathrm{year}}\right]$
C+6
C+5
C+4
C+3
$n_e\,t_{ion}$
log T = 6.4
Runge-Kutta solution

Figure 5a

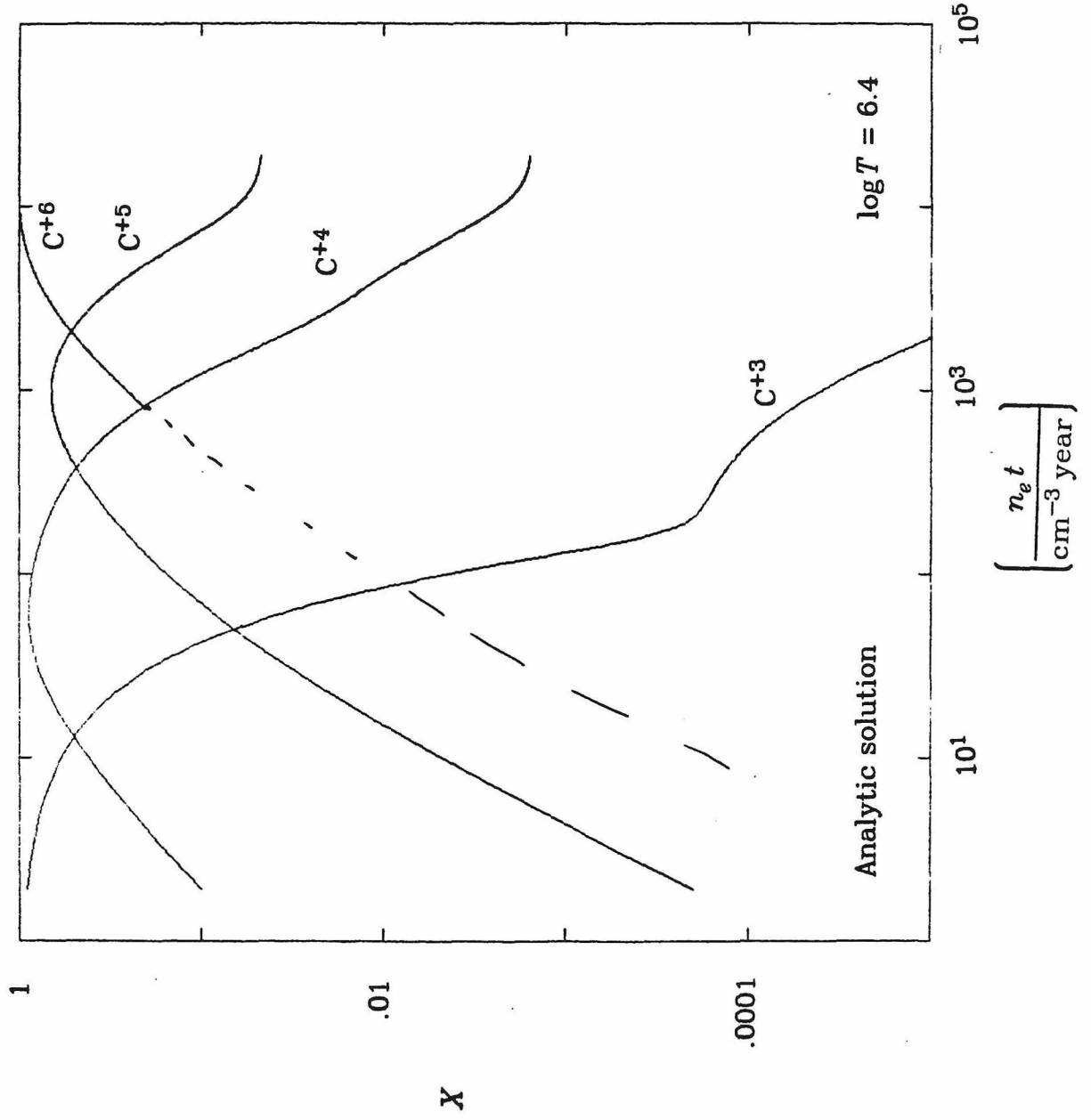
C+6
C+5
C+4
C+3
log T = 6.4
Analytic solution
X
1
.01
.0001
10^1
10^3
10^5
n_e t / cm^-3 year

Figure 5b

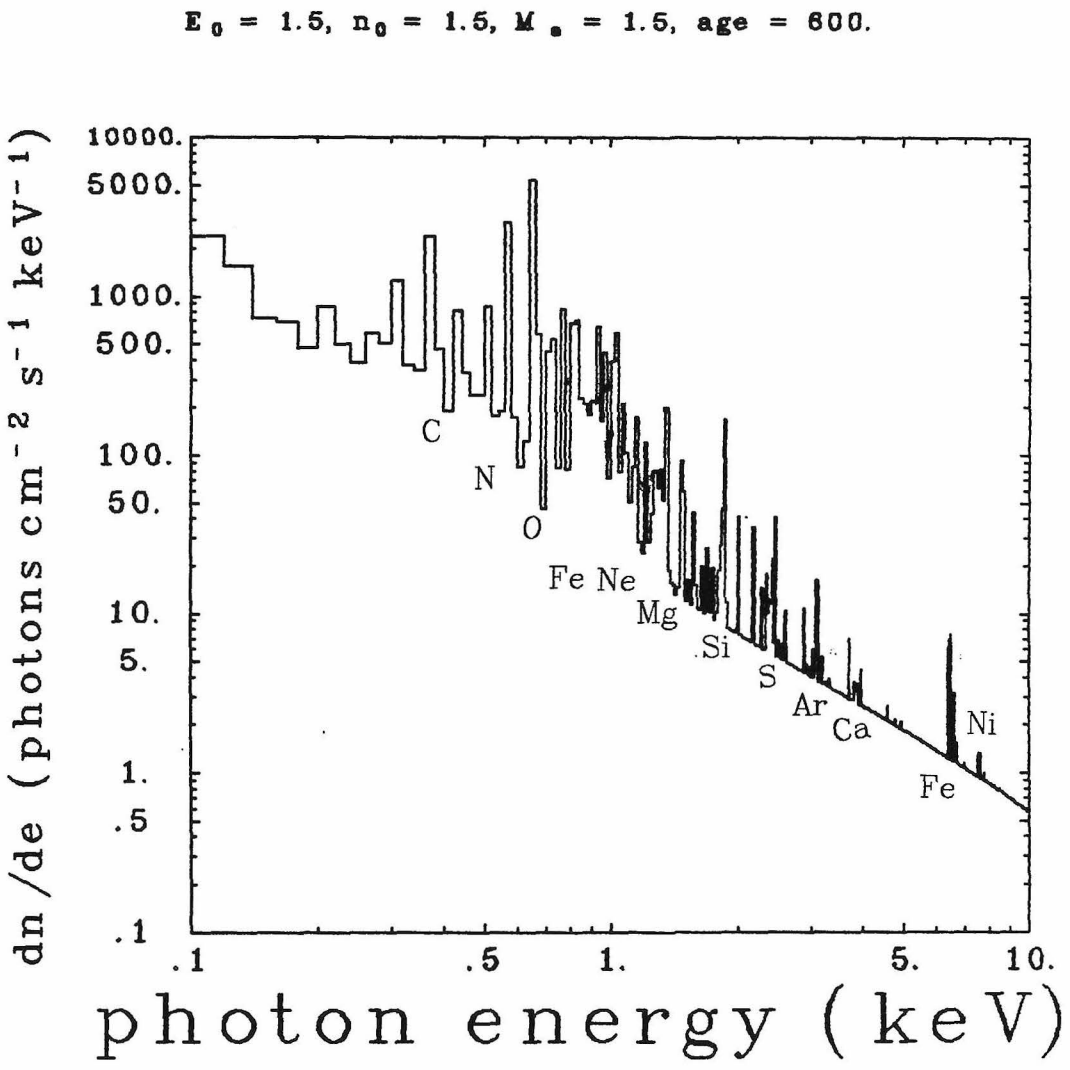
E_0 = 1.5, n_0 = 1.5, M_s = 1.5, age = 600.
dn/de (photons cm^{-2} s^{-1} keV^{-1})
10000.
5000.
1000.
500.
100.
50.
10.
5.
1.
.5
.1
.1
.5
1.
5.
10.
photon energy (keV)
C
N
O
Fe Ne
Mg
Si
S
Ar
Ca
Fe
Ni

Figure 6

Allen, C. W., 1976, *Astrophysical Quantities*, 4th ed. (London; The Athlone Press)

Bachall, J. N., and Wolf, R. A. 1965, *Ap. J.*, **142**, 1254.

Becker, R. H., Holt, S. S., Smith, B. W., White, N. E., Boldt, E. A., Mushotzky, R. F. and Serlemitos, P. J. 1980, *Ap. J. (Letters)*, **235**, L5.

Bevington, P. R. 1969, *Data Reduction and Error Analysis for the Physical Sciences* (New York; McGraw-Hill)

Caswell, J. L., Clark, D. H., and Crawford, D. F. 1975, *Australian J. Phys. Suppl.*, **37**, 39

Caswell, J. L. *et al.* 1976, *Astron. Astrophys.*,

Chevalier, R. A., 1977, *Ann. Rev. Astr. Ap.*, **15**, 175

Chevalier, R. A. 1975, *Ap. J.*, **200**, 698.

Clark, D. H. and Caswell, J. L. 1976, *M. N. R. A. S.*, **174**, 267.

Clark, D. H. and Stephenson, F. R., 1977, *Historical Supernovae* (Oxford; Pergamon Press)

Cox, D. P. and Anderson, P. R. 1982, *Ap. J.*, **253**, 268.

Fireman, E. L. 1974, *Ap. J.*, **187**, 57.

Glen, G. and Sutherland, P. G. 1980, *Ap. J.*, **239**, 671.

Groenschild, E. H. B. M., 1979 Utrecht University PhD thesis

Goss, W. M., and Shaver, P. A. 1970, *Aust. J. Phys., Astro. Suppl.*, **14**, 1

Gull, S. F. 1973, *M. N. R. A. S.*, **161**, 47.

Gull, S. F. 1975, *M. N. R. A. S.*, **171**, 263.

Hamilton, A. J. S., Sarazin, C. L., and Chevalier R. A. 1982 (preprint)

Hill, E. R. 1967,*Australian J. Phys.*, **20**, 297

Itoh, H., 1977, *Publ. Astr. Soc. Japan*, **29**, 813

Itoh, H., 1978, *Publ. Astr. Soc. Japan*, **30**, 489

Itoh, H., 1979, *Publ. Astr. Soc. Japan*, **31**, 541

Joyce, R. M., Becker, R. H., Birsa, F. B., Holt, S. S., and Noordzy, M. P. 1978, *IEEE Trans. Nucl. Sci.*, **25**, 453

Kato, T. 1976, *Ap. J. Suppl.*, **30**, 397.

Lampton, M. *et al.* 1976, *Ap. J.*, **208**, 177.

Lucke, R. L., *et al.* 1979, *Ap. J.*, **228**, 763.

Mansfield, V. N., and Salpeter, E. E. 1974, *Ap. J.*, **190**, 305.

McKee, C. F. 1974, *Ap. J.*, **188**, 335.

Mewe, R., Schrijver, J., and Sylwester, J., 1980, *Astr. Ap. Suppl.*, **40**, 323

Meyer, J., 1979, *Les Elememts et leurs Isotope dans l'Univers*, Comm. 22nd Colloq. Int. d'Astrophys. Liese, p.153

Naranan, S. *et al.* 1977, *Ap. J. (Letters)*, **213**, L53.

Normoto, K. and Tsurta, S. 1981, *Ap. J. (Letters)*, **250**, L19.

Nugent, J. J. and Garmire, G. P. 1978, *Ap. J. (Letters)*, **226**, L83.

Nugent, J. J. *et al.* 1982, *Ap. J. Suppl.*, (accepted).

Nussbaumer, H. and Osterbrook, D. E. 1970, *Ap. J.*, **161**, 811.

Pradhan, A. K., Norcross, D. W., and Hummer, D. G. 1981, *Ap. J.*, **246**, 1031.

Pravdo, S. H. and Smith, B. W. 1979, *Ap. J. (Letters)*, **234**, L195.

Raymond, J. C. and Smith, B. W. 1977, *Ap. J. Suppl.*, **35**, 419.

Richardson, M. B., *et al.* 1982, *Ap. J.*, **255**, 624.

Richtmyer, R. D., and Morton, K. W., 1967, *Difference Methods for Initial-Value Problems*, 2nd ed. (New York; InterScience)

Rothschild, R. *et al.*, 1979,*Space Sci. Inst.*, **4**, 169

Sedov, L., 1959, *Similarity and Dimensional Methods in Mechanics*, (New York; Academic)

Shlovsky, I. S., 1962, *Soviet Asto.*, **6**, 162

Shull, J. M. 1981, *Ap. J. Suppl.*, **46**, 27.

Shull, J. M., 1982, (preprint)

Solinger, A., Rappaport, S., and Buff, J. 1975, *Ap. J.*, **201**, 381.

Spitzer, L. 1962, *Physics of Fully Ionized Gases*, 2nd ed., (New York; InterScience)

Spitzer, L. 1978, *Physical Process in the Interstellar Medium*, (New York; InterScience)

Tuohy, I. R. *et al.* 1979, *Ap. J. (Letters)*, **230**, L27.

Tuohy, I. R. and Garmire, G. P. 1980, *Ap. J. (Letters)*,

Tuohy, I. R. *et al.*, 1983 (in preparation)

Tucker, W. H., and Koren, M. 1971, *Ap. J.*, **168**, 283.

Westerlund, B. E. 1969a, *Astron. J.*, **74**, 879.

Westerlund, B. E. 1969b, *Astron. J.*, **74**, 882.

Winkler, P. F. 1978, *Ap. J.*, **221**, 220.